

EFFECT OF COLD ROLLING AND ANNEALING PARAMETERS ON THE
MICROSTRUCTURE AND MECHANICAL PROPERTIES OF DUAL PHASE
STEELS

A THESIS SUBMITTED TO
THE GRADUATE SCHOOL OF NATURAL AND APPLIED SCIENCES
OF
MIDDLE EAST TECHNICAL UNIVERSITY

BY

OKAN POYRAZ

IN PARTIAL FULFILLMENT OF THE REQUIREMENTS
FOR
THE DEGREE OF MASTER OF SCIENCE
IN
METALLURGICAL AND MATERIALS ENGINEERING

JANUARY 2020

Approval of the thesis:

**EFFECT OF COLD ROLLING AND ANNEALING PARAMETERS ON THE
MICROSTRUCTURE AND MECHANICAL PROPERTIES OF DUAL
PHASE STEELS**

submitted by **OKAN POYRAZ** in partial fulfillment of the requirements for the degree of **Master of Science in Metallurgical and Materials Engineering Department, Middle East Technical University** by,

Prof. Dr. Halil Kalıpçılar
Dean, Graduate School of **Natural and Applied Sciences**

Prof. Dr. Cemil Hakan Gür
Head of Department, **Met. and Mat. Eng.**

Prof. Dr. Bilgehan Ögel
Supervisor, **Met. and Mat. Eng., METU**

Examining Committee Members:

Prof. Dr. Tayfur Öztürk
Met. And Mat. Eng., METU

Prof. Dr. Bilgehan Ögel
Met. and Mat. Eng., METU

Prof. Dr. Arcan Fehmi Dericioğlu
Met. And Mat. Eng./METU

Prof. Dr. Rıza Gürbüz
Met. And Mat. Eng./METU

Assoc. Prof. Dr. Ender Keskinılıç
Met. And Mat. Eng./Atılım University

Date: 21.01.2020

I hereby declare that all information in this document has been obtained and presented in accordance with academic rules and ethical conduct. I also declare that, as required by these rules and conduct, I have fully cited and referenced all material and results that are not original to this work.

Name, Surname: Okan Poyraz

Signature:

ABSTRACT

EFFECT OF COLD ROLLING AND ANNEALING PARAMETERS ON THE MICROSTRUCTURE AND MECHANICAL PROPERTIES OF DUAL PHASE STEELS

Poyraz, Okan
Master of Science, Metallurgical and Materials Engineering
Supervisor: Prof. Dr. Bilgehan Ögel

January 2020, 103 pages

This study consists of change in the microstructure and mechanical properties of the 0.14C-1.98Mn steel with different cold rolling ratios, annealing temperature and annealing time.

The starting sheet metal is 2.8mm thick and have a microstructure of ferrite-pearlite in as-received condition. Samples are cold rolled such that either 30%, 45% or 60% cold rolling is achieved. In order to see the change in microstructure below and in the intercritical temperatures, samples are annealed for 5 minutes or 10 minutes in the range 680°C - 800°C, then quenched in water. Finally, the as-received samples are annealed at the same temperatures range for 5 minutes in order to be able to compare the microstructural and mechanical property differences between cold rolled and ferritic-pearlitic samples.

Between 730-760°C, ferrite fraction and grain sizes of 45% samples is found to be highest at intermediate intercritical annealing temperatures, and as a result the lowest tensile strength is obtained. At higher temperatures, the effect of cold rolling ratio become negligible. The positive effect of increasing the annealing temperature and the annealing time on the amount of austenite formation is observed. Also, the main

nucleation sites for austenite is determined as grain boundaries that are close to carbon sources.

Keywords: Dual phase steels, DP steels, intercritical annealing, nucleation of austenite, recrystallization, cold rolling.

ÖZ

SOĞUK HADDELEME VE TAVLAMA PARAMETRELERİNİN ÇİFT FAZLI ÇELİKLERİN MİKROYAPI VE MEKANİK ÖZELLİKLERİNE ETKİSİ

Poyraz, Okan
Yüksek Lisans, Metalurji ve Malzeme Mühendisliği
Tez Danışmanı: Prof. Dr. Bilgehan Ögel

Ocak 2020, 103 sayfa

Bu çalışmada, 0.14C-1.98Mn içeren bir çeliğe uygulanan farklı soğuk hadde miktarları, interkritik tavlama sıcaklıkları ve interkritik tavlama sürelerinin çeliğin mikroyapı ve mekanik özellikleri üzerindeki etkisi incelenmiştir.

Başlangıçtaki çelik sacın kalınlığı 2.8mm olup, ferritik-perlitik bir iç yapıya sahiptir. Numuneler %30-%45 ve %60 redüksiyonlarda haddelenmiştir. İnterkritik sıcaklıklar ve altındaki sıcaklıklarda iç yapı değişimini görmek için numuneler, 680°C-800°C arasında 5 ve 10 dakika tavlانیp su verilmiştir. Son olarak, başlangıçtaki numuneler, soğuk haddelenmiş ve haddelenmemiş numuneler arasındaki farkı görebilmek amacı ile aynı sıcaklıklarda 5 dakika tavlانmıştır.

730°C-760°C arasında, %45 haddelenen numunelerdeki ferrit oranının en düşük olduğu, buna bağlı olarak en düşük çekme mukavemetine sahip olduğu görülmüştür. Yüksek sıcaklıklarda, redüksiyonun etkisi azalmıştır. İnterkritik tavlama sıcaklığı ve süresinin östenit oluşumuna pozitif etkisi görülmüştür. Ayrıca, östenit tanelerinin başlıca oluşma noktası olarak karbon kaynağına yakın tane sınırları belirlenmiştir.

Anahtar Kelimeler: ift fazlı elikler, DP elikleri, interkritik tavlama, stenit tanelenmesi, rekristalizasyon, soėuk haddeleme

To Poyraz family and all animals, especially Huginn and Muninn.

ACKNOWLEDGEMENTS

Firstly, I would like to state my genuine gratitude to my supervisor, Prof. Dr. Bilgehan Ögel. His door and phone was always open to not only my study related questions, but also guiding me through the life. His support and comments helped me overcome many problems, therefore I am indebted to him whole-heartedly.

I would also like to express my thanks to my prior manager, Celal Seyahiođlu. His trust, support and encouragement kept me going on this long and hard path.

I also owe my thanks to Serkan Yılmaz and Yusuf Yıldırım, together with Borçelik Laboratory teams for helping me with their hard working and helpful mindset.

I wish to acknowledge the understanding, love, guidance and wisdom of my parents, Mehmet Poyraz, Hürü Poyraz and brothers Dođan Poyraz, Arda Poyraz. This work would have been very hard for me without their endless support.

Lastly, my love, Aşkın Deniz Kaya, is the owner of my deepest gratitude. Her unexampled support, encouragement and existence was so precious that without her, this work could not have been possible.

TABLE OF CONTENTS

ABSTRACT	v
ÖZ	vii
ACKNOWLEDGEMENTS	x
TABLE OF CONTENTS	xi
LIST OF TABLES	xiii
LIST OF FIGURES	xiv
1. INTRODUCTION	1
2. LITERATURE REVIEW	3
2.1. Dual Phase Steels	3
2.2. Cold Rolling	6
2.3. Annealing in the Intercritical Region	10
2.3.1. Recovery and Recrystallization of Ferrite	10
2.3.2. Nucleation and Growth of Austenite	13
2.4. Effect of Important Alloying Elements on Dual Phase Steels	16
2.4.1. Carbon.....	18
2.4.2. Manganese	21
2.4.3. Silicon	26
2.4.4. Aluminum	27
2.4.5. Molybdenum.....	28
2.4.6. Chromium	29
3. EXPERIMENTAL PROCEDURE	31
3.1. Steel Used for the Experiments	31

3.2. Sample Taking	31
3.3. Heat Treatment.....	35
3.4. Microstructural Analysis.....	37
3.5. Quantitative Analysis.....	37
3.6. Tensile Tests	38
4. RESULTS.....	39
4.1. Microstructures and Mechanical Properties of As-Pickled Samples	39
4.2. Microstructures and Mechanical Properties of Cold Rolled Samples	43
4.3. The Microstructure and Mechanical Properties of Heat Treated Samples	47
4.3.1. Microstructures of Heat Treated Samples	48
4.3.2. Mechanical Properties	56
4.3.2.1. 5 Minute Annealed Samples	56
4.3.2.2. 10 Minute Heat Treatments	61
5. DISCUSSION	65
5.1. Recrystallization of Ferrite.....	65
5.2. Nucleation of Austenite	69
5.3. Mn Partitioning at 740°C, 760°C and 780°C.....	76
5.4. Comparison of Grain Sizes	79
5.5. Comparison of Ferrite Fractions	82
5.6. Comparison of Tensile Properties	88
6. CONCLUSIONS	91
7. REFERENCES	93

LIST OF TABLES

TABLES

Table 3.3.1. Chemical analysis of the steel used in this study.	31
<i>Table 3.2. Reduction ratios of each baby coils (Parts).</i>	33
Table 4.1. Summary of the heat treatments.	47
Table 4.2. Mechanical properties of the 5 minute annealed 30% CR samples.....	57
Table 4.3. Mechanical properties of the 5 minute annealed 45% CR samples.....	57
Table 4.4. Mechanical properties of the 5 minute annealed 60% CR samples.....	57
Table 4.5. Mechanical properties of the 10 minute annealed samples.....	62
Table 5.1. JMAK values of samples.	74

LIST OF FIGURES

FIGURES

Figure 2.1. Typical image and schematic of dual phase steels [18].	5
Figure 2.2. Tandem cold rolling mill [26]	7
Figure 2.3. Reversible cold rolling mill [27].	7
Figure 2.4. Typical grain structure after cold rolling of steel [30].	8
Figure 2.5. Elongation of ferrite and pearlite grains after A) 58% cold rolling, B) 70% cold rolling [31].	9
Figure 2.6. Recrystallization of steel with 0.22C with different martensite tempering temperatures and pearlitic microstructure [29].	9
Figure 2.7. Schematic representation of cold worked grains during recovery recrystallization and grain growth [17].	11
Figure 2.8. Microstructural changes during recovery [38].	11
Figure 2.9. Effect of Mo addition on the ferrite grain interface front speed. Horizontal axis indicates the interface front speed, left axis indicates the temperature [41].	12
Figure 2.10. Undissolved Carbide precipitates in martensite grains [13].	14
Figure 2.11. Austenite growth in 0,11C-1,68Mn steel, annealed at 740°C for 5 min [5].	15
Figure 2.12. Austenite growth in 0,11C-1,68Mn steel, annealed at 740°C for 24 hour [5].	15
Figure 2.13. Schematic view of austenite formation and growth during intercritical annealing. a) being the start of the annealing, d) being the end of the annealing [5].	16
Figure 2.14. <i>Fe binary phase diagrams according to Wever categorization. a) open austenite field, b) closed austenite field, c) expanded austenite field, d) contracted austenite field</i> [50].	17
Figure 2.15. Microhardness of martensite depending on the C content [55].	19
Figure 2.16. Yield strength of DP steels depending on C content [55].	20

Figure 2.17. C content vs austenite fraction formed in 1.50Mn steel with two different starting microstructures [46].	20
Figure 2.18. Change of the intercritical temperatures with Mn content in 0.16C steel [56].	21
Figure 2.19. Mn profile in ferrite in a 0.1C-6Mn steel at 650°C [57].	22
Figure 2.20. Mn profile in austenite in a 0.1C-6Mn steel at 650°C [57].	23
Figure 2.21. Mn concentration of ferrite and austenite phases in 0.06C-1.5Mn steel after 1h annealing at 740°C [60].	24
Figure 2.22. Mn partitioning by diffusion during annealing [60].	25
Figure 2.23. Microstructure of 0.06C-1.5Mn steel after annealing at 740°C followed with slow cooling [60].	25
Figure 2.24. Austenite formation diagram for 0.12C-1.5Mn steel [60].	26
Figure 2.25. Effect of Si content on the tensile strength and elongation in dual phase steels [64].	27
Figure 2.26. Tensile strength-elongation relationship with different amount of Al content in a dual phase steel [66].	28
Figure 3.1. Steel strip coil in hot rolled state.	32
Figure 3.2. Temperature heterogeneity in hot rolled steel during cooling, and places where PO samples are taken [70].	32
Figure 3.3. Borçelik cold rolling mill line.	34
Figure 3.4. Flat samples taken after cold rolling.	34
Figure 3.5. Mechanical tensile test specimen press machine.	35
Figure 3.6. Atmospheric heat treatment furnace.	36
Figure 3.7. DATAPAQ data logger.	36
Figure 3.8. Ferrite fraction detection using MIPAR.	38
Figure 3.9. INSTRON tensile test machine.	38
Figure 4.1. Microstructure of Part3. Etched with %2 Nital. Dark regions are pearlite, white regions are ferrite.	40
Figure 4.2. Microstructure of Part2. Etched with %2 Nital. Dark regions are pearlite, white regions are ferrite.	40

Figure 4.3. Microstructure of Part1. Etched with %2 Nital. Dark regions are pearlite, white regions are ferrite.	41
Figure 4.4. SEM image of Part2. F represents ferrite, P represents pearlite.	41
Figure 4.5. Ferrite fraction and grain size of each part prior to cold rolling.	42
Figure 4.6. Mechanical properties of each part of the PO.	43
Figure 4.7. 30% CR specimen before heat treatment.	44
Figure 4.8. 45% CR specimen before heat treatment.	44
Figure 4.9. 60% CR specimen before heat treatment.	45
Figure 4.10. Yield strength, tensile strength and elongation of samples after cold rolling.	46
Figure 4.11. Hardness Vickers versus cold reduction ratio.	46
Figure 4.12. Microstructure of 700-30-5. F represents ferrite, PP represents prior pearlite.	49
Figure 4.13. High magnification image of 700-30-5. M represents martensite, PP represents prior pearlite, GC represents globular cementite.	49
Figure 4.14. SEM micrograph of 700-45-5. M represents martensite, FC represents fragmented cementite.	50
Figure 4.15. SEM micrograph of 700-60-5. M represents martensite, FC represents fragmented cementite.	50
Figure 4.16. SEM image of 710-45-5. GC represents globular cementite, PP represents prior pearlite.	51
Figure 4.17. SEM image of 730-30-5.	52
Figure 4.18. SEM image of 730-45-5.	53
Figure 4.19. SEM image of 730-60-5.	53
Figure 4.20. SEM micrograph of 740-45-5.	54
Figure 4.21. SEM micrograph of 740-45-10.	54
Figure 4.22. SEM image of 800-30-5.	55
Figure 4.23. SEM image of 800-45-5.	55
Figure 4.24. SEM image of 800-60-5.	56

Figure 4.25. Yield Strength and Tensile Strength of 5 minute annealed samples below 740°C.....	58
Figure 4.26. Yield strength and tensile strength of 5 minute annealed samples above 740°C.....	58
Figure 4.27. Ferrite fraction of 5 minute annealed samples.....	59
Figure 4.28. Ferrite grain sizes of 5 minute soaked samples.	60
Figure 4.29. Temperature versus elongation for 5 minute annealed samples.....	61
Figure 4.30. 5 minute and 10 minute soaking time effect on the tensile strength.	62
Figure 4.31. Temperature-Elongation plot of 10 minute annealed samples.	63
Figure 4.32. Ferrite fractions of 10 minute annealed samples.	64
Figure 4.33. Ferrite grain sizes of 10 minute annealed samples	64
Figure 5.1. Light Microscope image of 680-30-5. Dark regions are pearlite, white regions are ferrite.	65
Figure 5.2. Light Microscope image of 680-45-5. Dark regions are pearlite, white regions are ferrite.	66
Figure 5.3. Ferrite aspect ratios of 5 minute annealed samples up to 720°C.	66
Figure 5.4. Light Microscope image of 680-60-5. Dark regions are pearlite, white regions are ferrite.	67
Figure 5.5. SEM image of 700-60-5 at 4000x. No deformed ferrite is observed.	68
Figure 5.6. Tensile strength of samples at 680°C and 700°C.....	69
Figure 5.7. SEM image of 720-30-5. White circles represent austenite formation from agglomeration of fragmented cementite particles, white rectangles represent prior pearlite bands, P represents Pearlite.....	71
Figure 5.8. SEM image of 720-45-5. White circles represent austenite formation from agglomeration of fragmented cementite particles, white rectangles represent prior pearlite bands, P represents Pearlite.....	71
Figure 5.9. SEM image of 720-60-5. White circles represent austenite formation from agglomeration of fragmented cementite particles. Note that these particles are considerably lower in amount than 30% and 45% CR samples.	72

Figure 5.10. Plotted graphs for calculation of Q values. a) 30% CR, b) 45% CR, c) 60% CR, d) NR HT. Vertical lines correspond the \ln function in Eq.10, horizontal lines correspond the $-1/T$ values.	74
Figure 5.11. Carbide fraction determination with MIPAR in 720-NR-5.	76
Figure 5.12. Mn partitioning during annealing at 740°C.	77
Figure 5.13. Mn partitioning during annealing at 760°C.	78
Figure 5.14. Mn partitioning during annealing at 780°C.	78
Figure 5.15. Grain sizes of annealed samples.	80
Figure 5.16. Ferrite grain size versus intercritical annealing temperature, from the study of Mazaheri et al [75].	81
Figure 5.17. Activation energy for heterogeneous nucleation of austenite [78].	81
Figure 5.18. SEM image of 730-60-5. Almost all grain boundaries are covered with martensite (M).	82
Figure 5.19. Ferrite fraction of annealed samples.	83
Figure 5.20. The degree of elongation of grains and cementite fragmentation in a) 30%, b) 45%, c) 60% as rolled samples. FC represents fragmented cementite.	85
Figure 5.21. SEM image of 730-30-5. White arrows represent martensite inside the grains.	86
Figure 5.22. SEM image of 730-45-5. White arrows represent martensite inside the grains.	86
Figure 5.23. SEM image of 730-60-5. White arrows represent martensite inside the grains.	87
Figure 5.24. Volume fraction of austenite in 0.14C-1.98Mn steel.	88
Figure 5.25. Tensile strengths of 5 minute and 10 minute annealed samples	90
Figure 5.26. Strain distribution between ferrite and martensite in networked and isolated martensite structures [89].	90

CHAPTER 1

INTRODUCTION

Change in strict regulations in automotive industry towards reduction of fuel usage and passenger safety forced steelmakers to search for alternative solutions. One of the biggest improvements in this industry is the introduction of Advanced High Strength Steels (AHSS). It is reported that, Hyundai i40 contains 35.6% traditional low-strength steel, 28.5% high strength steel and 28.5% AHSS [1].

From the AHSS family, dual phase steels contain ferrite and martensite in the microstructure. Their production consists of management of the alloying elements and process parameters so that the resulting microstructure mainly consists of hard martensite and soft ferrite phase. The mechanical properties of the steel is determined by the fraction of phases, and this fraction can be altered in order to have more strength, for passenger protection, and to have more ductility, better flangeability and formability.

So far, numerous studies had been done regarding the effect of chemical composition on the microstructure and mechanical properties of dual phase steels [2] [3] [4]. Moreover, the effect of intercritical annealing parameters have also been studied by some researchers [5] [6]

The effect of cold working on the microstructure and mechanical properties of dual phase steels, however, is not yet fully understood. Nikkhah et al has reported that, increasing the cold reduction ratio, increase in tensile strength seen for 3 different cold rolled samples, after quenching [7]. On the other hand, Zhang et al used 4 different cold rolled samples to investigate the intercritical annealing parameters, and they found that increasing the reduction ratio reduces the tensile strength of the samples slightly [8].

The focus on this study is to investigate the effect of cold reduction ratio, intercritical annealing temperature and annealing time on the microstructure and tensile properties of the chosen dual phase steel composition.

CHAPTER 2

LITERATURE REVIEW

2.1. Dual Phase Steels

The term Dual Phase steels first entered metallurgy dictionary in a conference in Berlin, 1978 [2]. Hayami and Furukawa's "unknown phase" works made a great impression on metallurgists [9] [10]. However, the motivation of carmakers did not last long in that era. One of the most passionate DP steel researcher, R. Davis (Ford Automotive), lost his interest on DP steels and the interest is eventually diminished [11]

Not every researcher had given up on this process. Inland Steel, USA, continued their work on DP steels and achieved TS up to 975 MPa [12]. This steel is used in fields such as car bumpers, beams in door structure and a few more places. This research and active usage of DP steels in cars made other carmakers desire for stronger and lighter steels for safety and fuel usage.

Another very big desire for DP steels came from the move of Honda. Honda factory in USA did many trials on DP steel usage on cars, which were mostly positive. As a result, their demand for uncoated and coated DP steels, especially DP590 grades increased. As successful usage of DP steels in some car parts and Honda's decision to move towards DP steels increased the attention, to DP steels, of carmakers and steelmakers [13].

Light-weight vehicle material competition was not only amongst steelmakers. In 1994, Audi launched their new aluminum-body car (A8), which was quite lighter than the steel-body cars and this move of Audi rallied steel producers [14].

After Audi's move, leading steel producers launched an international consortium that comprised 35 companies from 18 countries, which is called Ultra-Light-Steel Auto Body (ULSAB). ULSAB's work were successful in making car body with lighter steel alloys. Car bodies contained %90 High Strength Steels (HSS) and this made the car almost %25 lighter in mass and granted %14 fuel efficiency compared to cars produced with mild steel and Interstitial Free (IF) [13].

Currently, ULSAB proposed a new concept, Advanced Vehicle Concept (AVC), which aims to have %100 HSS, of which at least %80 of this is Advanced High Strength Steel (AHSS) [15]

Dual phase steels are defined in European Norms standard as steels that consist mainly martensite and ferrite, and possibly bainite as a third phase [16]. Minimum tensile strengths of industrial dual phase steels range from 450MPa to 1180MPa. Strength of dual phase steels can be improved by strengthening mechanisms such as increasing martensite fraction, reducing grain size or solid solution strengthening [17].

Matrix of dual phase steels are usually ferrite and martensite and other second phase islands are present within the matrix. Dual phase steels have relatively high toughness and isotropy at high stress levels. A typical dual phase microstructure is given in Figure 2.1 [18]. At very high stress levels (tensile strength above 800 MPa), high elongation is obtainable with dual phase microstructure due to the combination of soft ferrite phase and hard martensite phase [19].

Ferrite-Martensite DP

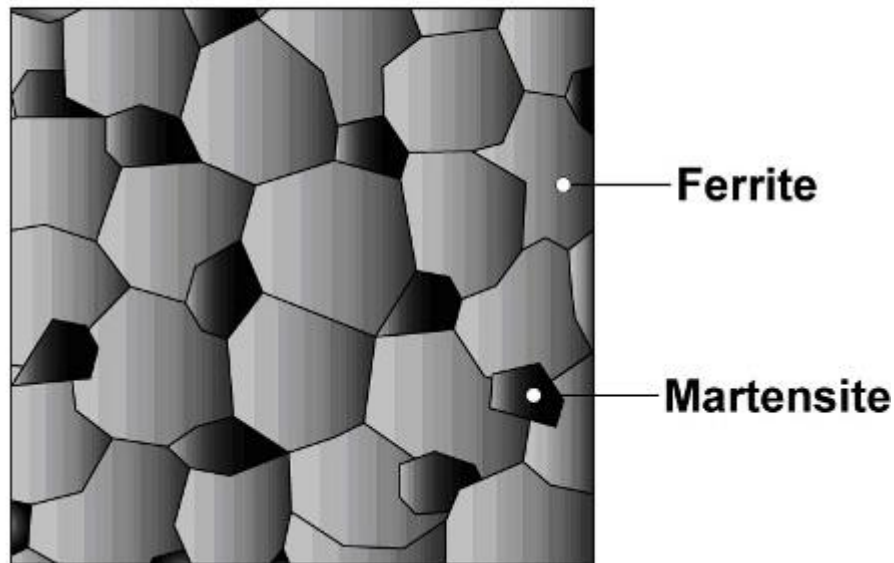


Figure 2.1. Typical image and schematic of dual phase steels [18].

Production of dual phase steels can basically be done by three different approaches. The first one is, adjusting the chemical composition and cooling rate so that, at the end of the hot rolling and coiling processes, mainly ferrite and martensite phases are present in the microstructure [20] [21] [22]. Due to high cost requirements and difficulty in thickness control, this method is undesired among the steelmakers. Also, use of CCT diagrams are not as accurate during hot rolling as another parameter, strain, comes into play. Prediction of phase transformation in the vicinity of strain is not quite an easy method. Another approach is the batch annealing method [23] [24] [25]. This process involves heating and cooling of the steel in massive batches. Due to the nature of heat transfer, time required for homogenous annealing and cooling is very long, which could take days, compared to continuous approach. Additionally, as the cooling rate is very low in batch annealing, higher amount of alloying elements are required for this process, which could increase the raw material price. For some steelmakers, low processing costs make batch annealing a suitable method for production of dual phase steels. The last approach is the production in continuous

annealing lines. Desired thickness could be easily obtained during cold rolling, precise process control and different cooling rates and possibility of integration of tempering furnaces enables production of dual phase steels in continuous annealing lines relatively easy and practical.

2.2. Cold Rolling

Cold rolling is the process performed after hot rolling and pickling of the steel coil. Steel coil with a high thickness is crushed between 2 work rolls to reduce the thickness to the desired level.

Cold rolling mills can be divided into 2 categories, tandem cold rolling mills (Figure 2.2) and reversible cold rolling mills (Figure 2.3). In reversible mills, head and the tail of the strip is connected between uncoiler and recoiler and the strip is passed between one set of work rolls back and forth. Tandem mills do not have uncoiler, as the hot rolled sheet is immediately rolled by sets of work rolls, which are placed back to back and at the end of the last work roll set, the strip is coiled.

Length of the reversible mills is shorter than tandem mills, the former's line total length is around 30 meters, while the latter's total line length could be up to 200 meters. While reversible mills has a length advantage, the biggest problem with these type of cold rolling mills are that, thickness is not controllable at the first and last loop of the coil. As the strip is connected to uncoiler and recoiler, the connected parts are not rolled, resulting in 30 to 50 meters of scrap for each coil. As tandem mills operate continuously and are not connected to any mandrel during the process, the whole strip could be reduced to the desired thickness.

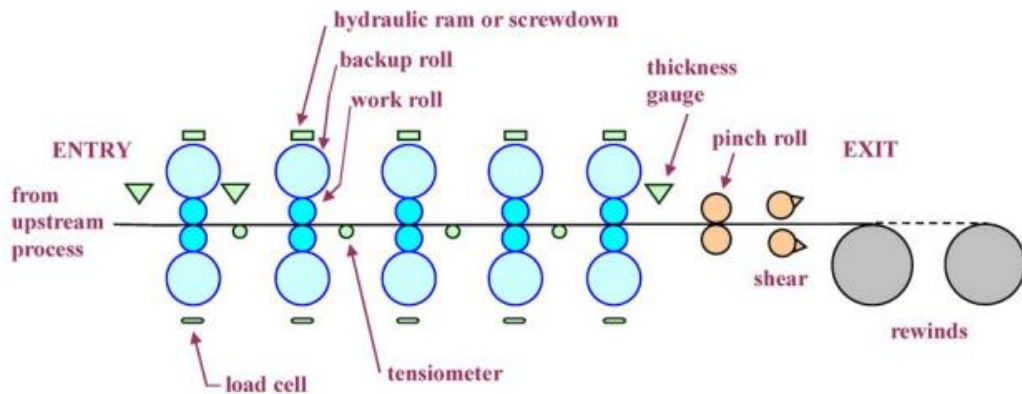


Figure 2.2. Tandem cold rolling mill [26]

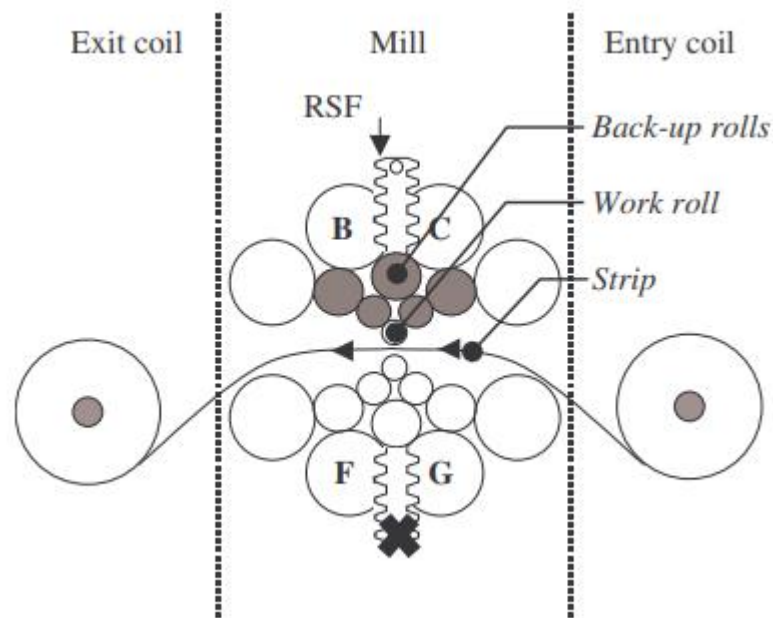


Figure 2.3. Reversible cold rolling mill [27].

Independent of the type of cold rolling mill, the steel undergoes to the same process. In each pass, thickness of the material is reduced, ferrite grains are elongated in the direction of rolling and the amount of grain boundary area increases (Figure 2.4). According to Humphreys, 50% cold rolling increases the surface area of a cubic grain

by 16%, 90% rolling increases the area by 270%, while further reduction to 99% increases the surface area by 3267% [28] (Figure 2.5).

During cold rolling, the driving force for recovery and recrystallization increases as the reduction ratio increases. In ferritic-pearlitic steels, ferrite grains are elongated and the dislocation density increases considerably. Cementite particles from pearlite grains are fragmented, resulting in smaller pearlite grains and fine cementite particles scattered across the microstructure. Scattering of cementite particles could increase the nucleation sites for austenite, which could positively affect the final microstructure and mechanical properties of the steel. Therefore, the amount of cold reduction is an important parameter in the production of steel.

Figure 2.6 shows recrystallization start temperature for martensitic and pearlitic starting microstructures. It can be seen that independent of the starting microstructure, cold work ratio increases the driving force for recrystallization and reduces recrystallization start temperature [29].

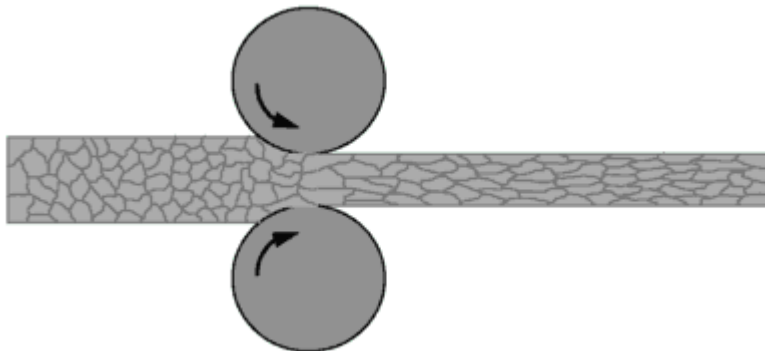


Figure 2.4. Typical grain structure after cold rolling of steel [30].

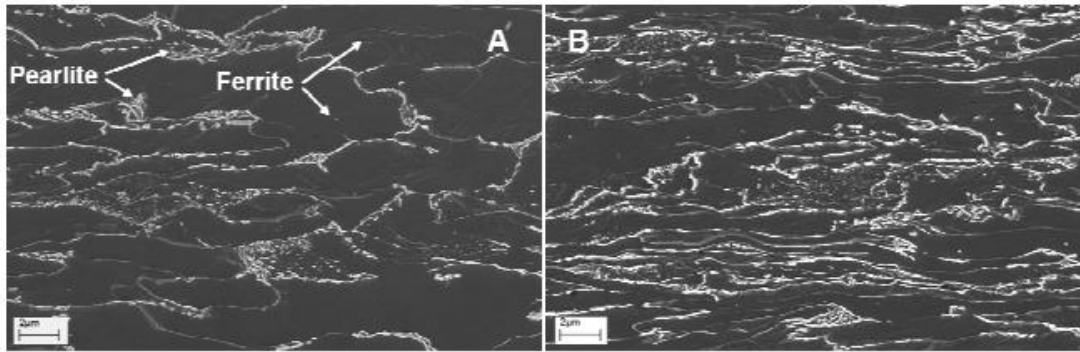


Figure 2.5. Elongation of ferrite and pearlite grains after A) 58% cold rolling, B) 70% cold rolling [31].

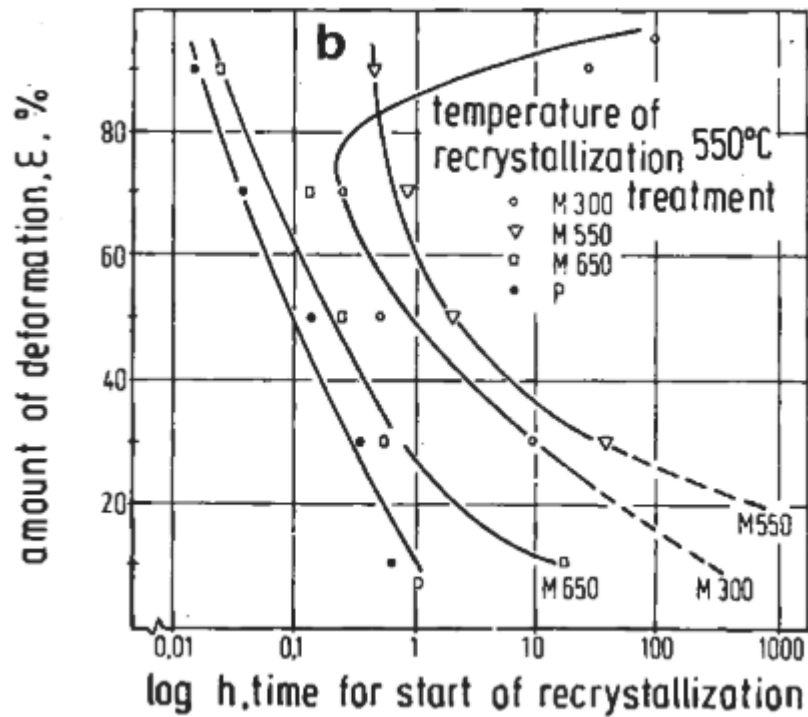


Figure 2.6. Recrystallization of steel with 0.22C with different martensite tempering temperatures and pearlitic microstructure [29].

Cold deformation of steel has been receiving more and more attention recently, due to its effect on grain refinement [32] [33] [34]. Increasing nucleation sites for ferrite transformation during the cooling from austenite region, Hodgson et al has achieved

ferritic microstructure of 1 μ m ferrite grain size and introduced transformational grain refinement term to the metallurgy [35] [36].

2.3. Annealing in the Intercritical Region

2.3.1. Recovery and Recrystallization of Ferrite

During annealing of a cold rolled steel, the first stage is the recovery stage. Recovery is a homogeneous process, means that all regions of the annealed material are changing in a similar manner, towards reducing internal stored energy to a small degree. This stage is basically rearrangement of dislocation cells to a energetically more favored states. The second stage is the recrystallization stage, where new, stress free ferrite grains start to form along nucleation sites [28]. Both stages are thermally activated processes and driven by the internal stored energy, which means the higher the internal stored energy, the more driving force for recovery and recrystallization stages, which reduces temperature requirement for both stages.

The microstructure of the deformed steel should be able to provide new nucleus formation and provide enough energy to continue recrystallized grain growth. This concludes that there is a minimum amount of cold working required for recrystallization to occur. If the cold work amount is minimal, temperature of recrystallization would be high and recovery could be finished until recrystallization starts. If the cold work amount is high, the desire to reduce strain energy reduced recrystallization temperature, therefore recovery and recrystallization may co-exist.

In Figure 2.7, evolution of microstructure during annealing below A1 temperature is given. During recovery period, minimal increase in ductility is seen as cold worked

grains have not yet been eliminated. Microstructural changes during recovery is schematically shown in Figure 2.7 and Figure 2.8. Increasing the annealing temperature, recrystallization stage begins, so does nucleation of stress-free grains. At this point, a noticeable increase in ductility, also reduction in tensile strength of the steel is seen.

Recrystallization could begin with high angle grain boundary migration, sub-boundary migration and sub-grain coalescence [37]. First movements of the grains during recrystallization occur at high energy regions such as inclusion edges or grain boundaries.

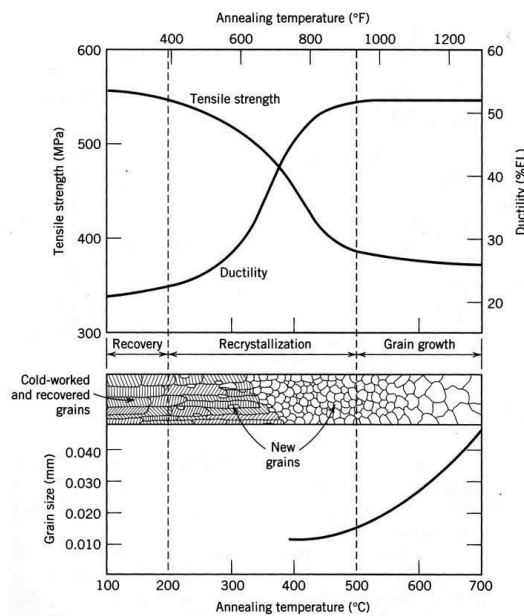


Figure 2.7. Schematic representation of cold worked grains during recovery recrystallization and grain growth [17].

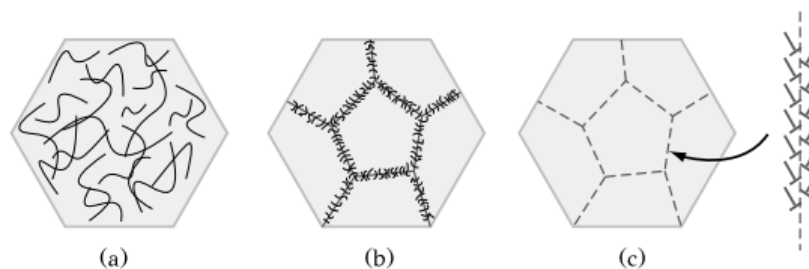


Figure 2.8. Microstructural changes during recovery [38].

Rate of formation and growth of recrystallized ferrite grains can be changed quite easily by addition of alloying elements and forming precipitates [39]. Using fine precipitates such as AlN, VC, VN, TiC, TiN could pin the ferrite grain interface front and limit the grain size. Figure 2.9 shows the effect small amount of Mo addition on the interface front speed of the ferrite.

However, addition of second phase particles could have a nucleation promoting effect on the microstructure. Cahn et al stated that, second phase particles with a size greater than $1\mu\text{m}$ could provide nucleation sites for recrystallization, while smaller and closely packed particles act as recrystallization and nucleation inhibiting agents [40].

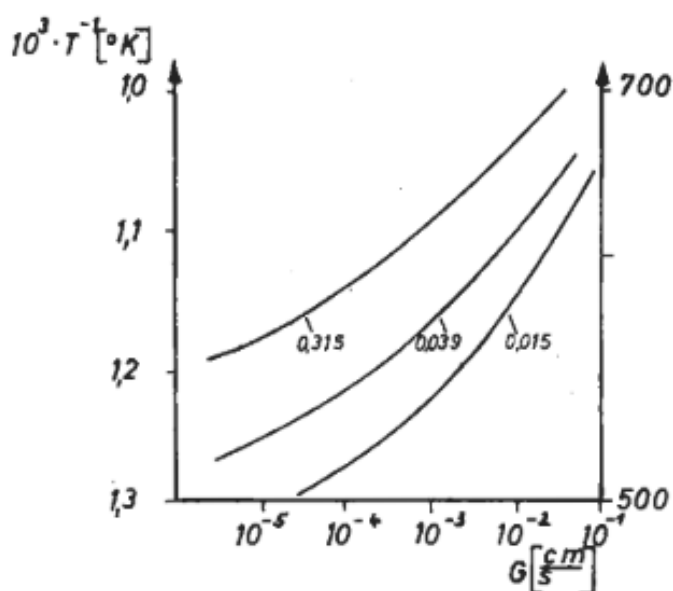


Figure 2.9. Effect of Mo addition on the ferrite grain interface front speed. Horizontal axis indicates the interface front speed, left axis indicates the temperature [41].

2.3.2. Nucleation and Growth of Austenite

Final microstructure of dual phase steel contains ferrite and martensite. Combination of soft ferrite and hard martensite results in superior stress-elongation properties. As the strength and hardness of the steel is directly related to martensite content, mechanical properties of the steel could easily be modified by altering the microstructure.

Upon heating the steel above A1 temperature, austenite starts to form at carbon rich grain boundaries and cementite islands [42]. Increasing annealing temperature reduces carbon content of the austenite, thus reduces hardenability of the austenite. However, applying lever rule, as temperature increases, amount of martensite formed also increases.

In the below equation (Eq.1), derived by Wycliffe et al [43], v is the velocity of austenite phase boundary, D is the diffusivity of carbon in the austenite, $\frac{dC}{dx}$ is the gradient of the carbon concentration within the austenite grain, $\Delta C^{\gamma \rightarrow \alpha}$ is the carbon concentration difference between austenite and ferrite and $\Delta C^{C \rightarrow \gamma}$ is the carbon concentration difference between carbide and austenite. As the temperature increases, all of the above parameters contribute to the increase of v .

$$v = D \frac{dC}{dx} \left(\frac{1}{\Delta C^{\gamma \rightarrow \alpha}} + \frac{1}{\Delta C^{C \rightarrow \gamma}} \right) \quad \text{Eq.1}$$

The reason for amount of martensite to increase and amount of ferrite to decrease as increasing the temperature can be explained by the effect of difference between $\Delta C^{C \rightarrow \gamma}$ and $\Delta C^{\gamma \rightarrow \alpha}$. Increasing annealing temperature, decrease in $\Delta C^{\gamma \rightarrow \alpha}$ is bigger than in $\Delta C^{C \rightarrow \gamma}$, so at elevated temperatures, austenite growth into ferrite is more pronounced [13]. This may cause undissolved carbide precipitates in austenite grains (martensite after quenching), shown in Figure 2.10. Therefore, even though diffusion rate of

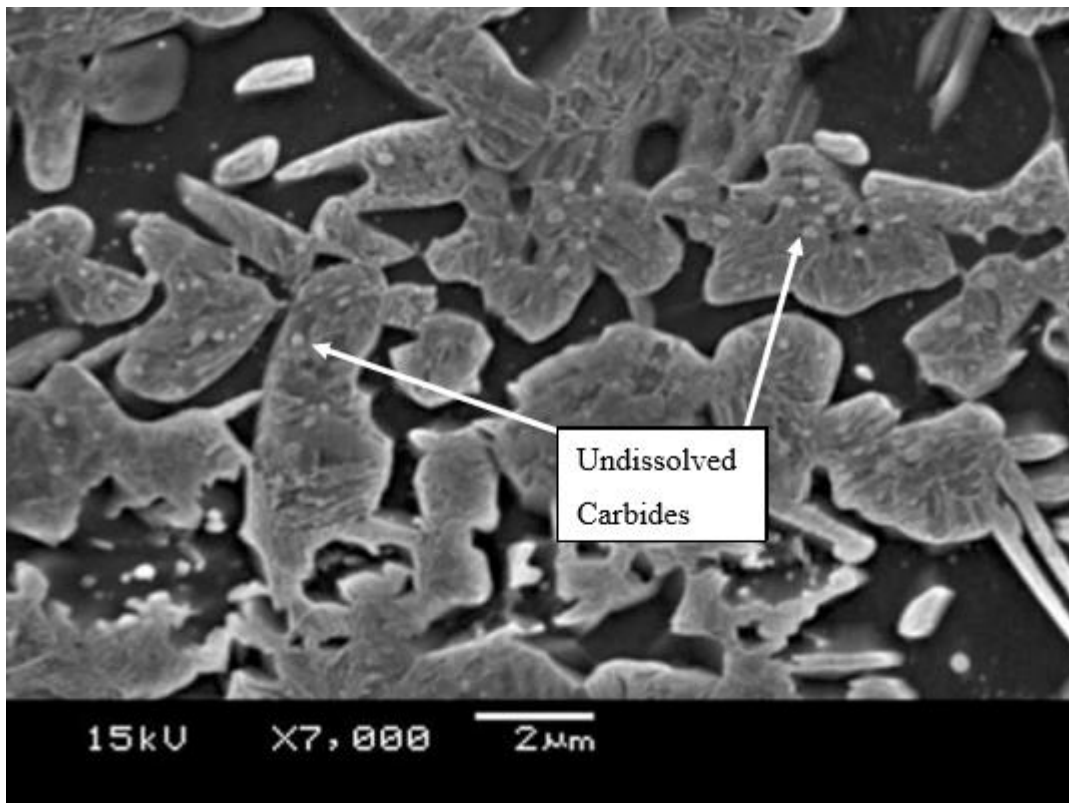


Figure 2.10. Undissolved Carbide precipitates in martensite grains [13].

carbon increases with increasing temperature, undissolved carbides may be present in the case of high carbon and high annealing temperatures.

Nucleation of austenite starts primarily at ferrite/ Fe_3C and carbon rich ferrite/ferrite interfaces [44] [45]. Upon reaching A_1 temperature during heating, austenite starts to form at carbon rich zones and as time passes, growth is in the direction of both away from the grain boundaries, and mostly, along the grain boundaries [46]. It can be said that austenite growth into the ferrite grain is slowest because of the depleted carbon content as formation of austenite requires C diffusion into the austenite grain. Estay et.al. has performed intercritical annealing at 740°C and water quenching tests on their work and found that, nucleating of austenite is seen that at 5 min at the grain boundaries and carbon rich regions. For 24 hour annealing at 740°C , almost all grain boundaries are covered with austenite with a great increase in austenite fraction

(Figure 2.11, Figure 2.12, Figure 2.13) [5]. Other researchers also reported that increasing annealing time, increases volume fraction of austenite [47] [48].

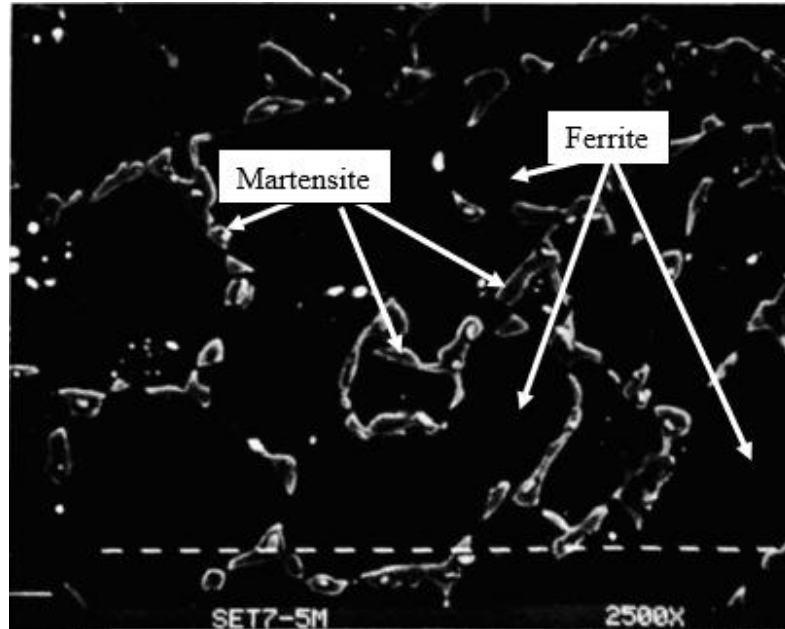


Figure 2.11. Austenite growth in 0,11C-1,68Mn steel, annealed at 740°C for 5 min [5].

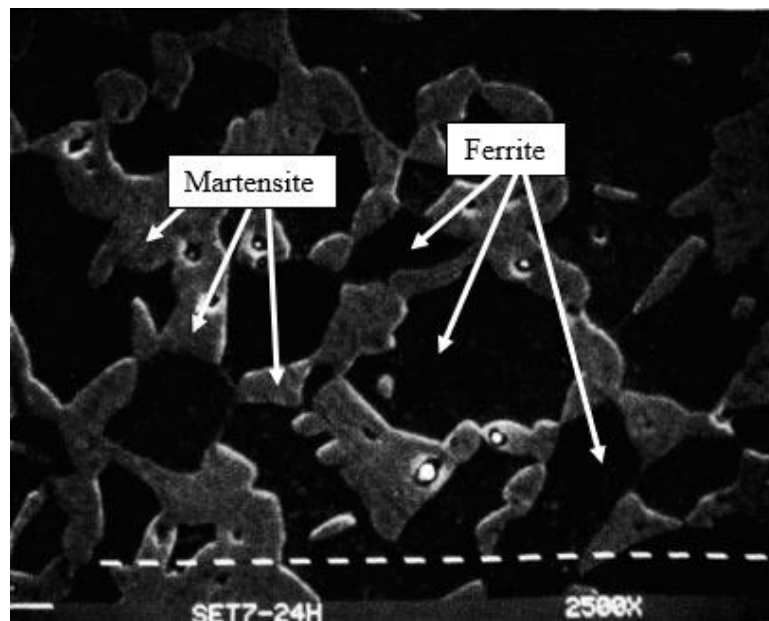


Figure 2.12. Austenite growth in 0,11C-1,68Mn steel, annealed at 740°C for 24 hour [5].

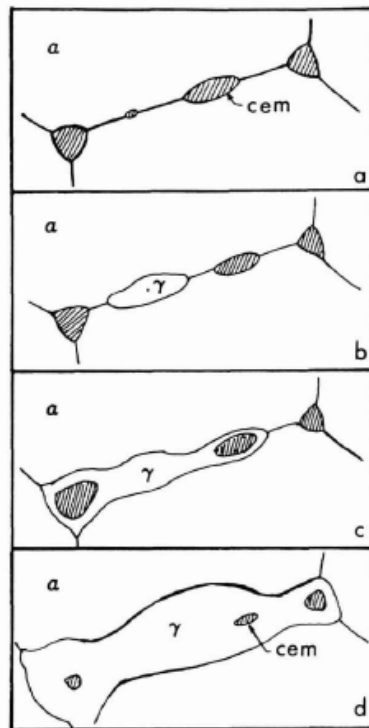


Figure 2.13. Schematic view of austenite formation and growth during intercritical annealing. a) being the start of the annealing, d) being the end of the annealing [5].

Effect of cold rolling on nucleation of austenite is an important subject. As mentioned previously, austenite starts to nucleate on ferrite-ferrite or ferrite-cementite grain boundaries. Cold rolling the steel prior to intercritical annealing increases number of dislocations and carbide fragments, therefore increasing the number of sites that austenite can form and reduce the path that carbon has to diffuse [49].

2.4. Effect of Important Alloying Elements on Dual Phase Steels

Almost all alloying elements have an effect on phase diagrams. In 1928, Wever has introduced 4 main categories that Fe binary diagrams fall into (Figure 2.14). These diagrams are based on some important element amounts in the steel. For example,

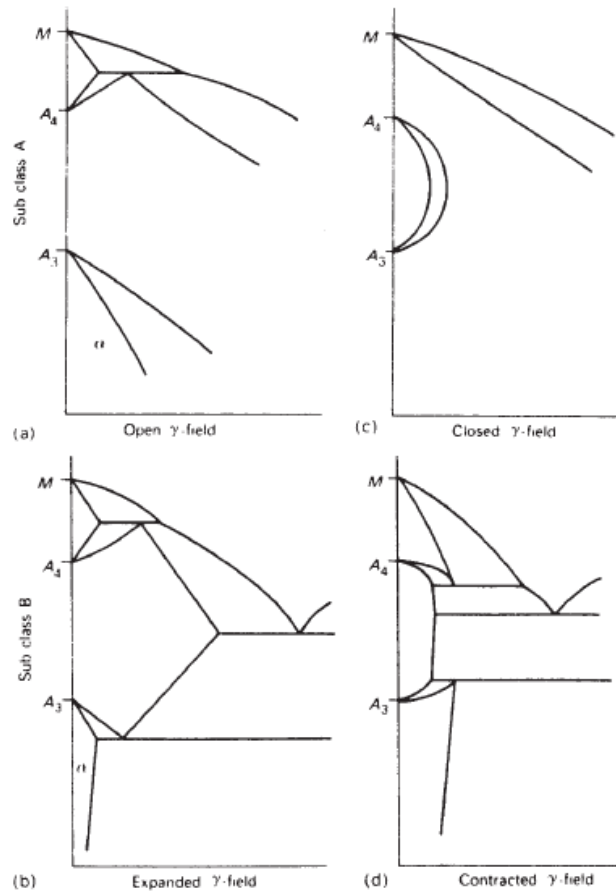


Figure 2.14. Fe binary phase diagrams according to Wever categorization. a) open austenite field, b) closed austenite field, c) expanded austenite field, d) contracted austenite field [50].

nickel and manganese are strong Mn stabilizers and if added high enough, may cause ferrite phase to completely be removed. Elements such as Si and Al shrink austenite phase while promoting formation of ferrite, causing “shrinkage” in the austenite area in the binary phase diagrams [51].

Shrinking and expanding of the austenite phase directly affects the Ae1 and Ae3 temperatures (intercritical lower and upper temperatures). Andrews has suggested below formulas for determination of Ae1 and Ae3 temperatures in steels [52]:

$$Ae1 = 723 - 10.7Mn - 16.9Ni + 29.1Si + 16.9Cr + 290As + 6.32W \quad \text{Eq.2}$$

$$Ae3 = 910 - 203\sqrt{C} - 15.2Ni + 44.7Si + 104V + 31.5Mo + 13.1W - 30Mn + 11Cr + 20Cu - 700P - 120As - 400Ti \quad \text{Eq.3}$$

Another important equation is the critical cooling rate calculation. In order to obtain ferrite-martensite microstructure after cooling, Speich has suggested below empirical equation to determine the required critical cooling rate for dual-phase microstructure [53]:

$$\log \text{Cooling Rate} \left(\frac{C}{sec} \right) = -1,7 * Mn_{eq} + 3,95 \quad \text{Eq.4}$$

Where CR is the critical cooling rate and Mn_{eq} is the equilibrium manganese ratio. Chromium and molybdenum also has an effect on equilibrium manganese ratio, given by below empirical formula, found by Rigsbee et al [54]:

$$Mn_{eq} (\%) = (\%Mn) + 1,3 * (\%Cr) + 2,67 * (\%Mo) \quad \text{Eq.5}$$

2.4.1. Carbon

In order to control the amount of carbon in ferrite and martensite, it is usually wanted for carbon content to be not higher than 0,30% weight percent. Carbon is the main alloying element that determines martensite hardness. In order to avoid high contrast of hardness between ferrite and martensite phases, low carbon content is desired.

Increasing annealing temperature, carbon content in austenite (martensite, after quenching) reduces and the amount of martensite increases while carbon content in

ferrite remains relatively the same. Main effect of carbon in austenite is the control of hardenability [13], and at high temperatures, transformation of austenite to martensite would require higher cooling rates.

Effect of C content on the mechanical properties of dual phase steels arises from the amount of martensite. In many studies, it is shown that increasing C content increases yield and tensile strength of the steel.

Effect of C content of martensite to martensite hardness and yield strength in 1.45Mn containing steels that are annealed at 760°C for 30 min then water quenched are shown in Figure 2.15 and Figure 2.16. Increasing the carbon content, hardness of the martensite and yield strength of the samples increase almost linearly. In Figure 2.17, C content of the steel versus fraction of austenite formed for two different starting microstructures is given [46]. It can be concluded that, C content both increases the martensite amount and hardness of the martensite phase.

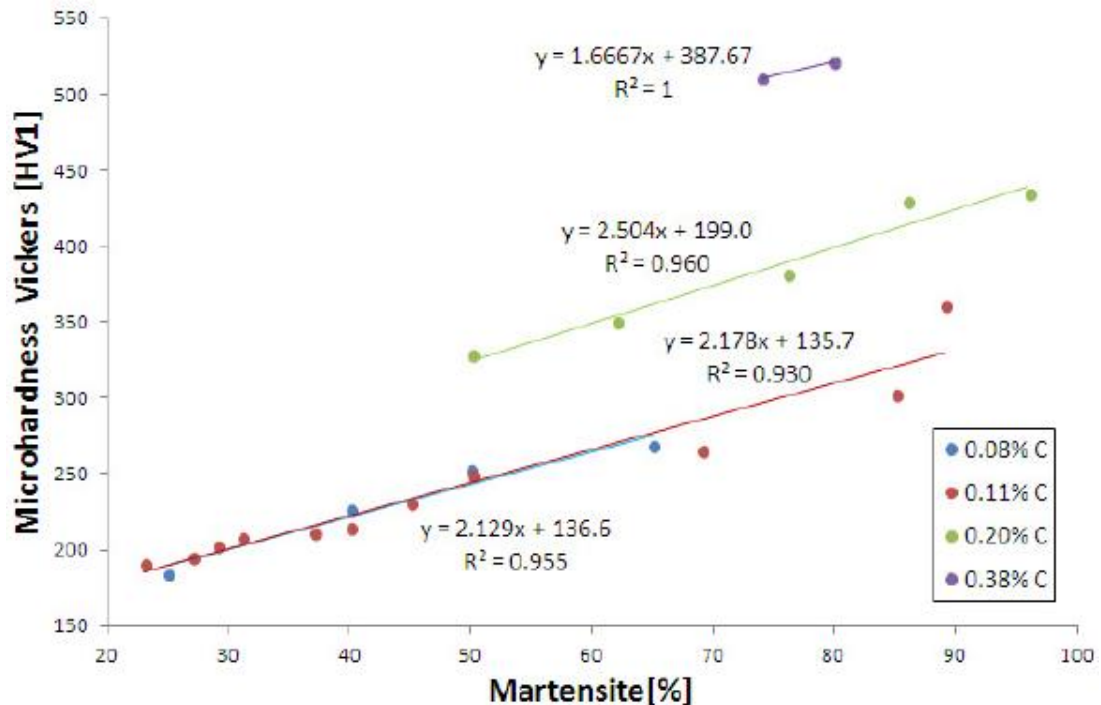


Figure 2.15. Microhardness of martensite depending on the C content [55].

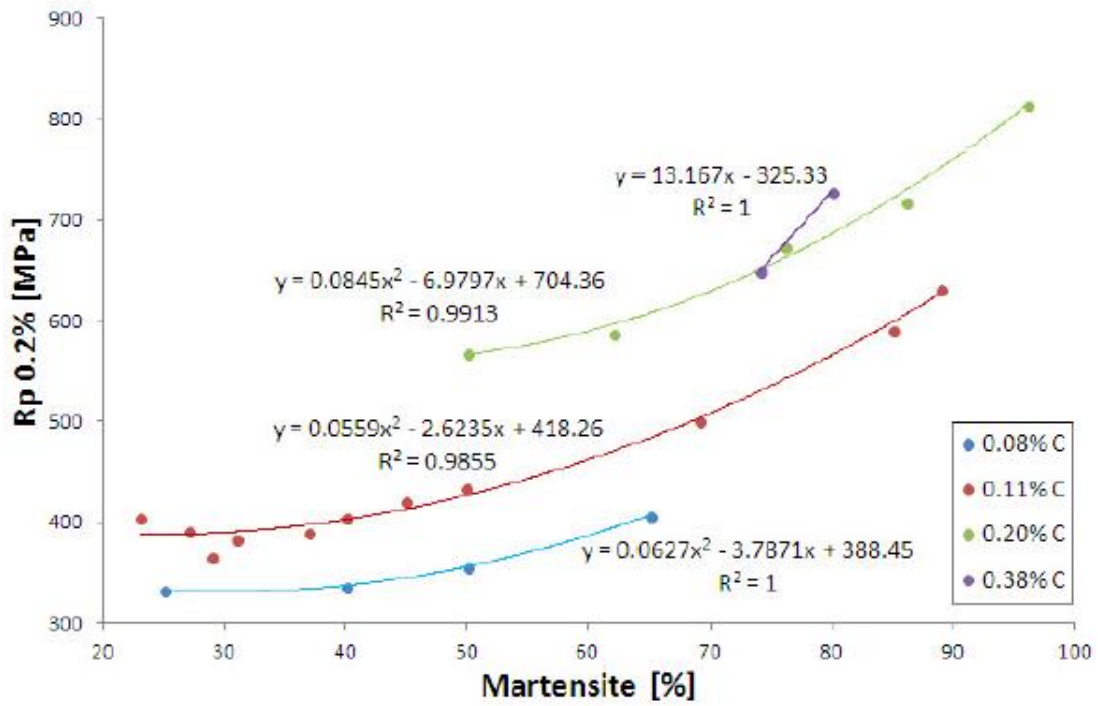


Figure 2.16. Yield strength of DP steels depending on C content [55]

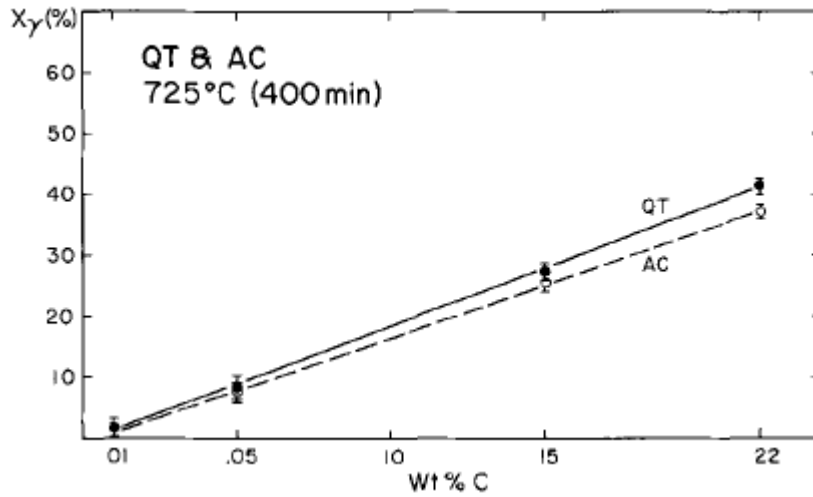


Figure 2.17. C content vs austenite fraction formed in 1.50Mn steel with two different starting microstructures [46].

2.4.2. Manganese

The effect of manganese content is mainly to the grain refinement of austenite [13]. Calcagnotto et al has reported that addition of manganese has 4 main effects on the austenite. These are, decrease of A1 temperature and so required annealing temperatures, expanding ferrite + cementite + austenite phase region, in where austenite growth is very limited, refinement of cementite, which in turn causes a great pinning effect on the grain boundaries, and reduction of grain boundary movement due to solute drag effect [48]. These effects cause an increase in strength while keeping the elongation similar in the steel.

In Figure 2.18, change of the A1 and A3 temperatures with changing Mn content in 0.16C steel is shown. Increasing Mn content reduces both A1 and A3 temperatures.

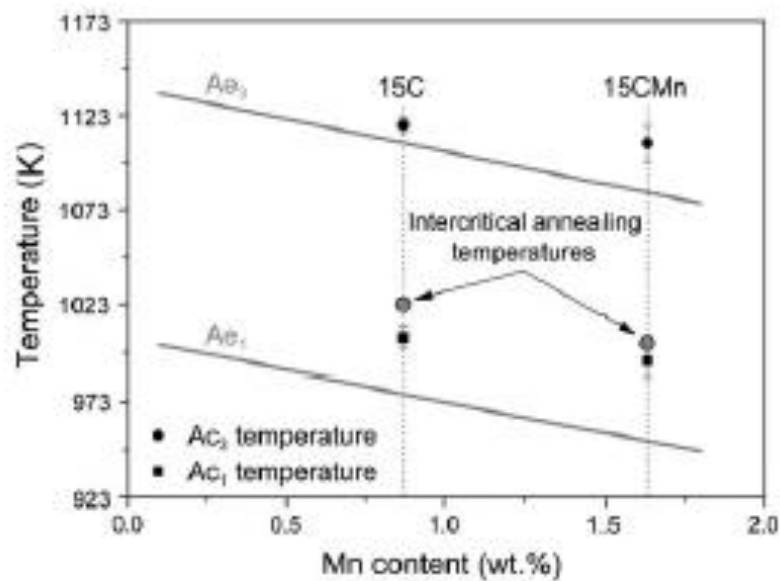


Figure 2.18. Change of the intercritical temperatures with Mn content in 0.16C steel [56].

Mn content in austenite for production of DP steels are of great importance as Mn is an austenite stabilizing element. Due to diffusion of Mn from ferrite to austenite grain being slow, a Mn rich zone at the grain boundary between ferrite and austenite is expected [57] [58]. Their work on a steel with 0.1C-6Mn steel has shown that at the ferrite side of the grain boundary, a Mn depleted zone occurs and with increasing time, homogenization of the Mn in ferrite slowly proceeds (Figure 2.19).

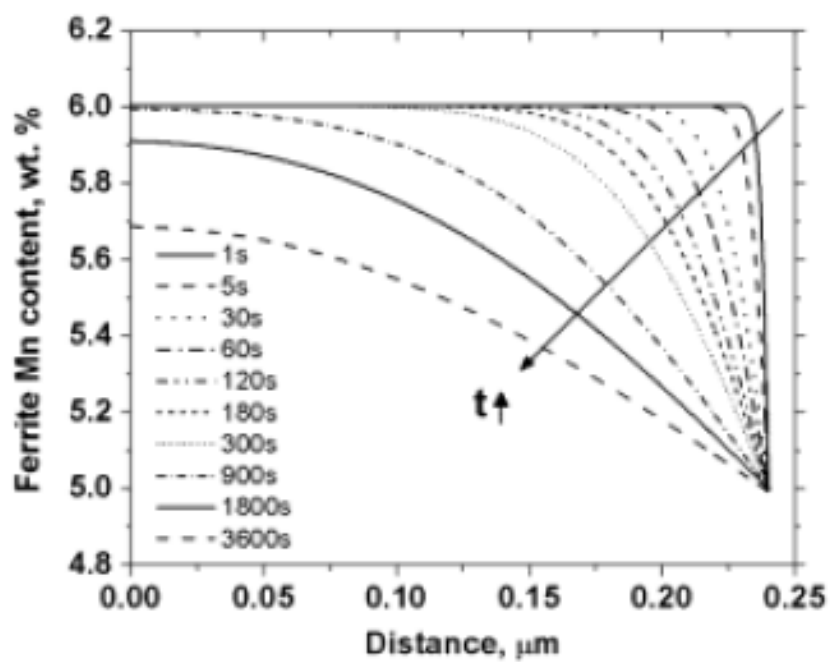


Figure 2.19. Mn profile in ferrite in a 0.1C-6Mn steel at 650°C [57].

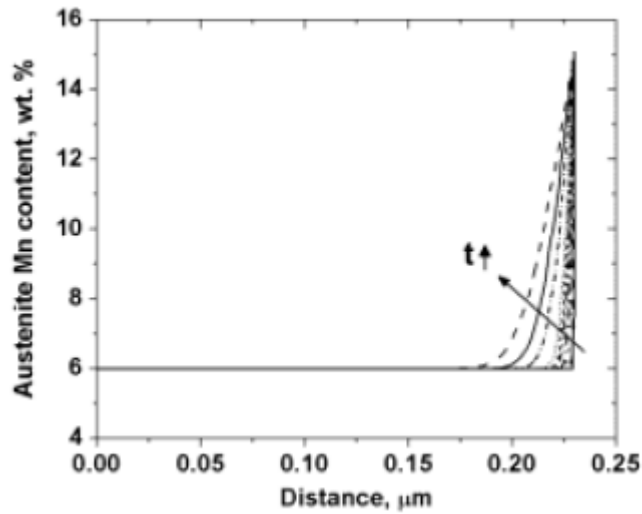


Figure 2.20. Mn profile in austenite in a 0.1C-6Mn steel at 650°C [57].

At the austenite side of the grain boundary however, Mn rich zone is formed and as time passes by, homogenization of Mn in austenite proceeds (Figure 2.20).

As dashed lines from Figure 2.19 and Figure 2.20 correspond to the same annealing times, it is seen that Mn diffusion in ferrite is faster than Mn diffusion in austenite. For 1 minute holding between 750°C and 850°C, diffusion distance of Mn in ferrite is around 0.2μm and in austenite is lower than 0.01μm [59]. In his work with 0.06C-1.5Mn steels, Speich et. al. has found that the Mn diffusion in ferrite is almost third order of the Mn diffusion in austenite [60]. In Figure 2.21, a similar result to Moor's work has been obtained at different temperature by Speich. Note that 1 hour annealing at intercritical temperature (740°C) is not sufficient for complete Mn diffusion and homogenization for 0.1C-1.5Mn steel.

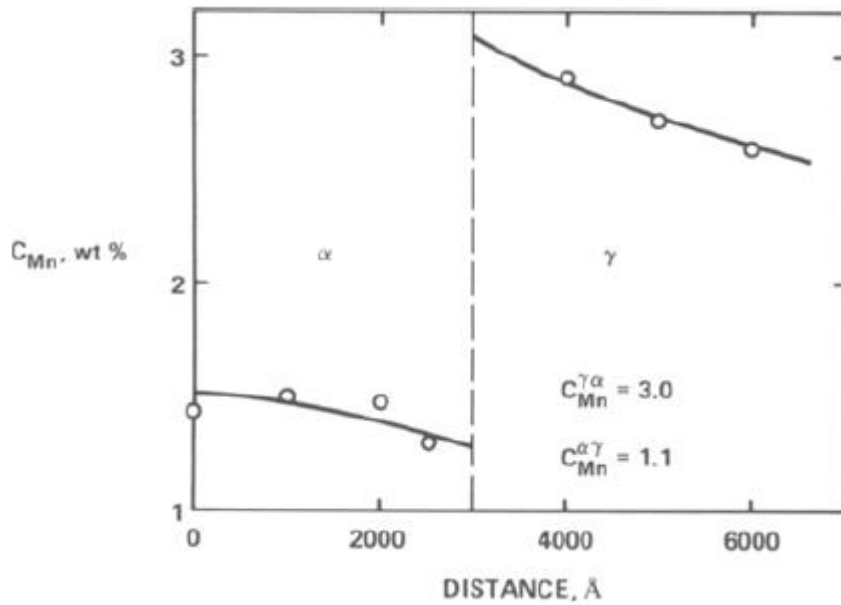


Figure 2.21. Mn concentration of ferrite and austenite phases in 0.06C-1.5Mn steel after 1h annealing at 740°C [60].

As previously mentioned, Mn is an austenite stabilizing element and delays pearlite or ferrite formation to a degree. If the steel is cooled before the Mn homogenization, an Mn-rich zone at the austenite side of the grain boundary will show different transformation kinetics than the middle of the austenite grain (Figure 2.22). If diffusion kinetics are not enough, it is very possible for martensite formation at the edge of the austenite grain, while inner sections of austenite transform to pearlite, bainite or ferrite, schematically shown in Figure 2.23 [60].

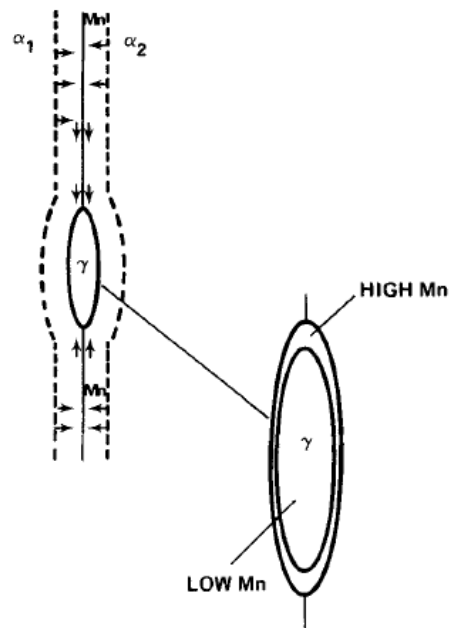


Figure 2.22. Mn partitioning by diffusion during annealing [60].

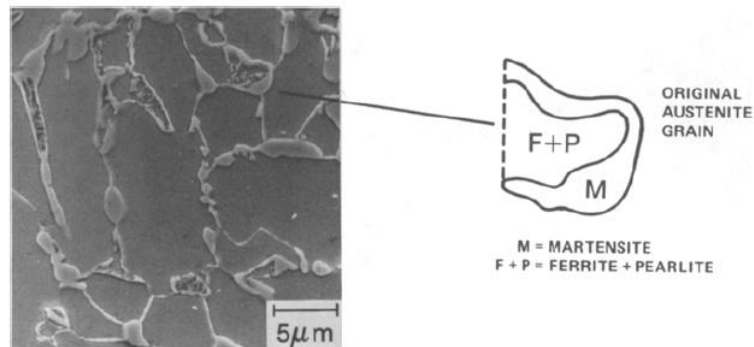


Figure 2.23. Microstructure of 0.06C-1.5Mn steel after annealing at 740°C followed with slow cooling [60].

Speich was able to plot Figure 2.24 using his experimental data, which is very important and useful for production of DP steels containing low carbon and high Mn. It can be seen that at low intercritical temperatures dissolution of pearlite takes long time, which may cause, for short annealing times, presence of pearlite in the final microstructure. After this region ends, diffusion on Mn starts which could take up to 270 hours. His theoretical calculations showed no Mn diffusion zone above 840°C.

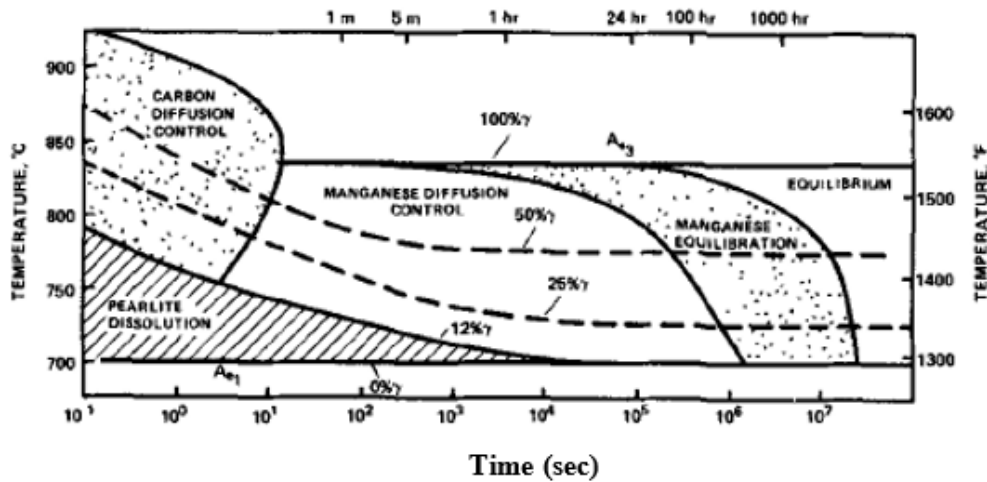


Figure 2.24. Austenite formation diagram for 0.12C-1.5Mn steel [60].

2.4.3. Silicon

Silicon is usually the main alloying element in the dual phase steel alongside with manganese. As Si is a ferrite forming element, it increases A_1 temperature, causing ferrite grains to be larger during heating, reduces the amount of Fe_3C precipitates. Reduction of Si content causes formation of brittle carbides along ferrite / austenite grain boundaries.

Nouri et al has reported that at higher Si contents, Mn partitioning between ferrite and austenite is higher [61]. Presence of Si in ferrite phase, promote higher flux of carbon migration to austenite [62]. It both increases the yield and tensile strength of the steel by solid solution strengthening and enhances mechanical properties by improving the elongation-tensile strength balance [63] [64] (Figure 2.25).

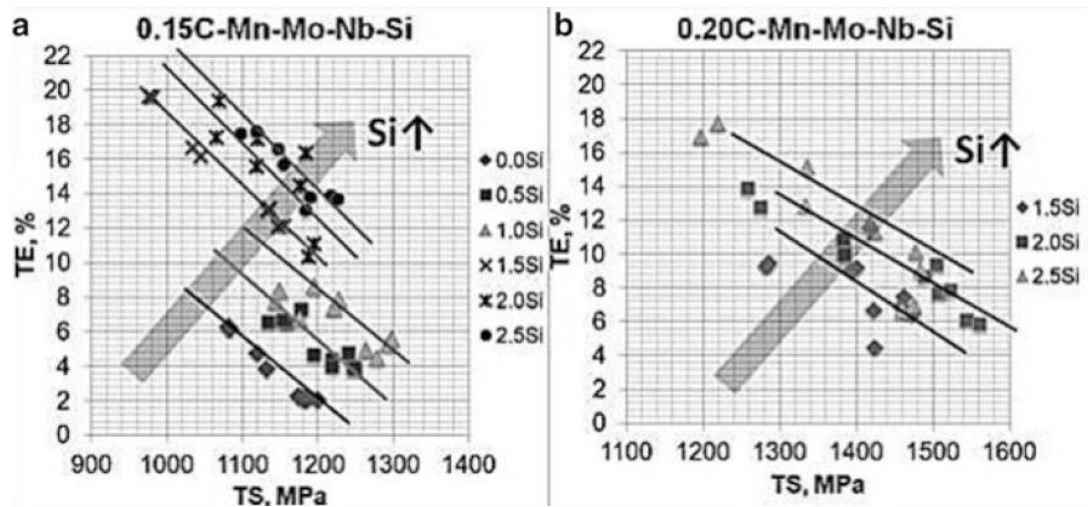


Figure 2.25. Effect of Si content on the tensile strength and elongation in dual phase steels [64].

2.4.4. Aluminum

Aluminum is also a ferrite-forming element similar to Si. Addition of Al, as well as Si, has an indirect effect on formation of new ferrite, which is crucial for controlling carbon content in austenite and stability of austenite [13]. Addition of Si increases A1 and A3 temperatures, making formation of ferrite faster [65]. In their experiments, Girina et al. has found that increasing Al content, formation of new ferrite is accelerated and carbon distribution between ferrite and austenite is improved, which leads to delay of bainitic transformation and increase in martensite amount [66]. Al also has a grain refinement effect on ferrite and may bind with Nitrogen to form AlN, preventing Nitrogen to bind with other precious alloying elements such as Titanium.

Effect of Al content on the tensile properties of dual phase steels are mainly due to increase of A3 temperature, hence reduced amount of austenite formed, and to refinement of grains. Girina and Fonstein reported that increase in Aluminum content could balance tensile strength and elongation relationship in dual phase steel by refinement of ferrite grains [66].

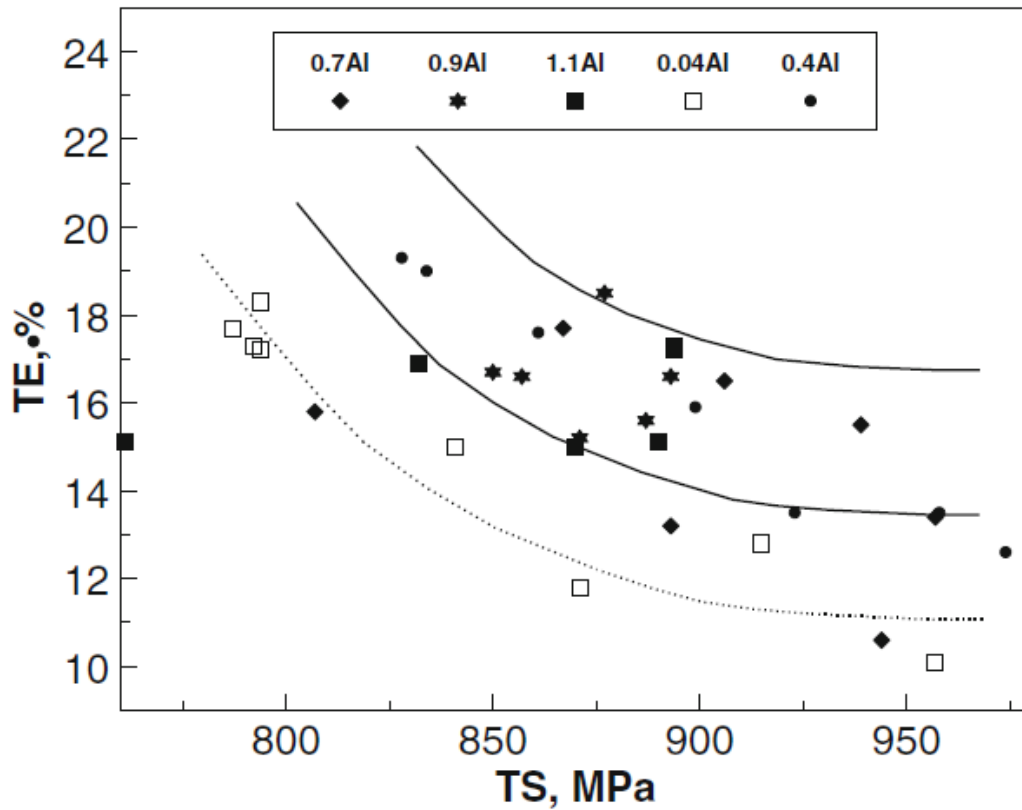


Figure 2.26. Tensile strength-elongation relationship with different amount of Al content in a dual phase steel [66].

2.4.5. Molybdenum

Molybdenum promotes martensitic transformation by improving hardenability of austenite. It delays pearlitic and ferritic transformation reaction, and reduces bainite start temperature. At low cooling rates, Mo is the best austenite stabilizer among other elements such as Mn and Cr, as indicated by Irie et al [67]. For galvanizing process, where galvanizing bath is between 450°C-500°C, addition of Mo extends the required time for bainitic reaction to start and reduces bainitic reaction start temperature, avoiding formation of bainite in the final microstructure for dual phase steels. Hara et

al has reported that, addition of Mo to low carbon steels causes Mo-C precipitate to form, leaving more precious alloying elements such as B or Nb to carbon-free and in the solid solution [68].

2.4.6. Chromium

Chromium increases hardenability of austenite and retards austenitic transformations, enabling, at relatively slow cooling rates, formation of martensite [69]. At intercritical annealing temperatures, due to high carbon content of austenite, effect of Cr is more significant. If added extensively, steel's performance during deep drawing is negatively affected.

CHAPTER 3

EXPERIMENTAL PROCEDURE

3.1. Steel Used for the Experiments

In this study, a 20 ton, 800 meters long, 1142 mm wide and 2,8 mm thick steel strip coil is used. Coil was purchased by Borçelik, a joint venture of ArcelorMittal and Borusan Holding, as hot rolled condition. Chemical analysis of the steel is given in Table 3.3.1. The steel coil in the hot rolled state is shown in Figure 3.1.

Table 3.3.1. Chemical analysis of the steel used in this study.

Element	C	Mn	Si	Cr+V	Ti+Nb	Ni+Al	C _{eq}
(%)	0.14	1.98	0.21	<0.40	<0.05	<0.1	0.56

3.2. Sample Taking

The coil (also called as the mother coil) is first pickled oiled in Borçelik Continuous Pickling Line (CPL) to remove the rust on the coil surface. The first and last 25 meters are cut and discarded in order to avoid inhomogeneities which can occur after hot rolling and coiling due to the differences in chemical composition and cooling rates. After, the steel is cut into 3 equal parts (also called as baby coils) of 250 meters each. At the end of each baby coil, 3 30 cm flat samples are taken for initial microstructural analysis. The places where PO (pickled oiled) samples are taken are shown in Figure 3.2. Some production lines are equipped with high technology monitoring systems to adjust the cooling rate just before the coiling so that no homogeneity occurs

throughout the coil. First cut part is called Part3, second cut part is called Part2, third cut part is called Part1 in this study.



Figure 3.1. Steel strip coil in hot rolled state.

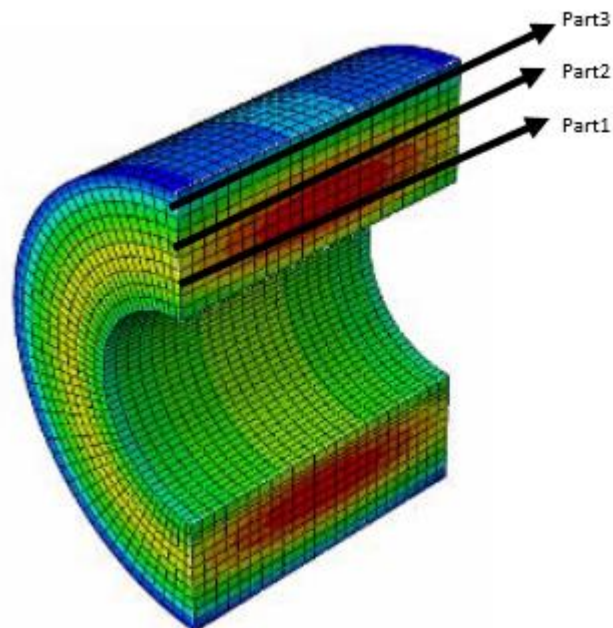


Figure 3.2. Temperature heterogeneity in hot rolled steel during cooling, and places where PO samples are taken [70].

After taking of the samples, each baby coil (parts) is cold rolled into different thicknesses in Reversible Cold Rolling Mill in Borçelik (Figure 3.3). Reduction ratios are chosen so that effect of annealing in the intercritical region can be seen in low, middle and high cold rolling ratios. Part1, Part2 and Part3 coils are cold rolled to their final thicknesses in 3, 5 and 7 passes, respectively (Table 3.2).

After the rolling of each coil in Borçelik Reversible Cold Rolling Mill line, around 20 meters of strip is cut to the scrap from the coil head. Then 10 samples from each baby coil, each with a length of 30 cm, are taken (Figure 3.4).

Table 3.2. Reduction ratios of each baby coils (Parts).

	Part1	Part2	Part3
Starting Thickness (mm)	2,80	2,80	2,80
Reduction Ratio (%CR)	60%	45%	30%
Final Thickness (mm)	1,12	1,54	1,96
Number of Passes	7	5	3



Figure 3.3. Borçelik cold rolling mill line.



Figure 3.4. Flat samples taken after cold rolling.



Figure 3.5. Mechanical tensile test specimen press machine.

The tensile test specimens were prepared parallel in the direction of hot rolling and cold rolling. Specimens were punched from the sheets directly using a die and hydraulic press, as shown in Figure 3.5.

3.3. Heat Treatment

Heat treatments were done in muffle furnace (Figure 3.6). The furnace has a maximum temperature capacity of 1200°C. The samples were heated to the required temperatures at a rate of 1°C/sec. Thermocouple is placed inside the furnace, very close to the samples each time. Thermocouple is connected to DATAPAQ data logger, which has a capability of logging data every second for up to 6 hours (Figure 3.7).

In annealing, the samples were hold in a temperature range of 680C-800C for either 5 min or 10 min. Following each heat treatment, samples were quenched in water.



Figure 3.6. Atmospheric heat treatment furnace.



Figure 3.7. DATAPAQ data logger.

The heat treatments were planned such that the effect of the amount of cold reduction, the soaking time and annealing temperature on the microstructure can be observed. For comparison purposes, a specimen cut from the as-received (NR HT (Not rolled, heat treated)) is also heat treated. Samples were designated as *temperature*-*%CR*-*annealing time*. For example 740-60-10 means that 60% cold rolled sample annealed at 740°C for 10 minutes.

All tests were repeated 3 times in order to increase accuracy and minimize error.

3.4. Microstructural Analysis

After heat treatment, the samples were sectioned parallel to the rolling direction and mounted in Bakalite. After grinding and polishing, they were etched (in 2% Nital etchant) in order to analyze the microstructure.

In this study, optical microscopy (Huvitz) and Field Emission Scanning Electron Microscopy (FESEM) (FEI NOVA NANOSEM 430) was used to analyze the microstructure of the samples. Optical microscopy was used in order to find the volume fractions of ferrite and martensite, and also for general microstructural examination. FESEM is used especially to analyze the carbides, to determine the austenite nucleation regions and to see the effect of cold reduction on the A_{e1} temperature by closely analyzing martensite formation.

3.5. Quantitative Analysis

Volume ratio and grain sizes of the phases were calculated by an image analyzer software, MIPAR. Different recipes for all samples in order to identify ferrite and to emphasize grain boundaries were created for analyses to be accurate (Figure 3.8).

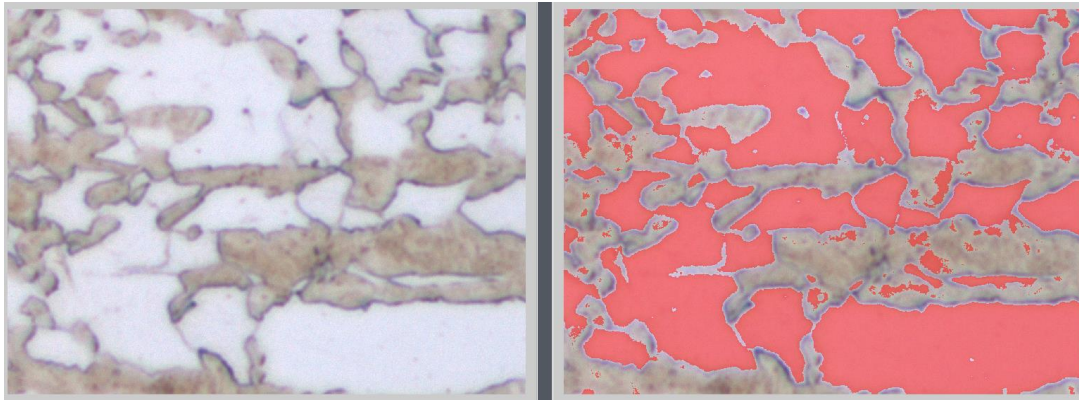


Figure 3.8. Ferrite fraction detection using MIPAR.

3.6. Tensile Tests

Tensile tests of the heat treated specimens were performed in Borçelik. The tensile test machine is INSTRON, has a maximum capacity of 25 tons (Figure 3.9). Tensile tests are done at a speed of 32 mm/minute.



Figure 3.9. INSTRON tensile test machine.

CHAPTER 4

RESULTS

The aim of this work is to see the effect of rolling ratio, annealing temperature and annealing time on the microstructure and tensile properties of dual phase steels. Pickled-oiled (not cold rolled), 30% cold rolled, 45% cold rolled, 60% cold rolled steel specimens were annealed at the pre-determined temperatures for 5 minutes and 10 minutes. After annealing, specimens were quenched in water.

4.1. Microstructures and Mechanical Properties of As-Pickled Samples

The microstructures of each batch are shown in Figure 4.1, Figure 4.2 and Figure 4.3 and SEM image is given in Figure 4.4. Starting microstructure is ferrite-pearlite. In order to measure the amount of the primary ferrite grains, the microstructure is analyzed quantitatively. Quantitative analysis results of PO samples are given in Figure 4.5. A slight reduction of ferrite fraction from Part3 to Part1 can be seen. During coiling of the hot rolled strip, cooling rate is different throughout the length due to overlapping the strip onto the cold recoiler [70]. Also, edges of the strip may cool faster due to being exposed directly to air. Therefore, slight differences in ferrite fraction and grain sizes in the parts are expected.

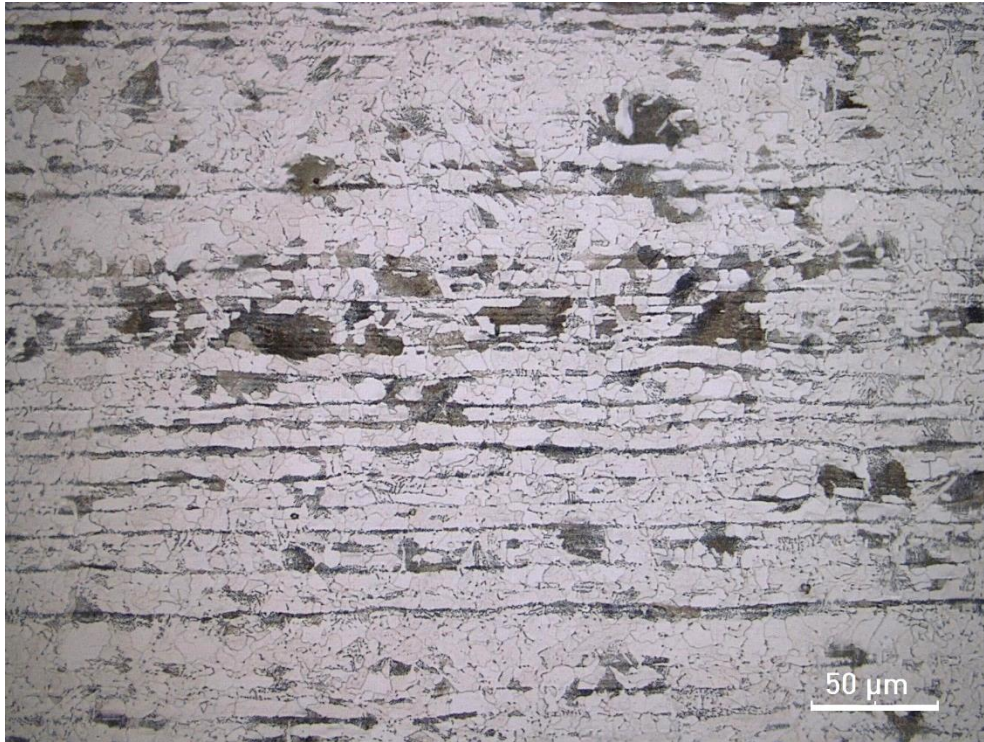


Figure 4.1. Microstructure of Part3. Etched with %2 Nital. Dark regions are pearlite, white regions are ferrite.



Figure 4.2. Microstructure of Part2. Etched with %2 Nital. Dark regions are pearlite, white regions are ferrite.

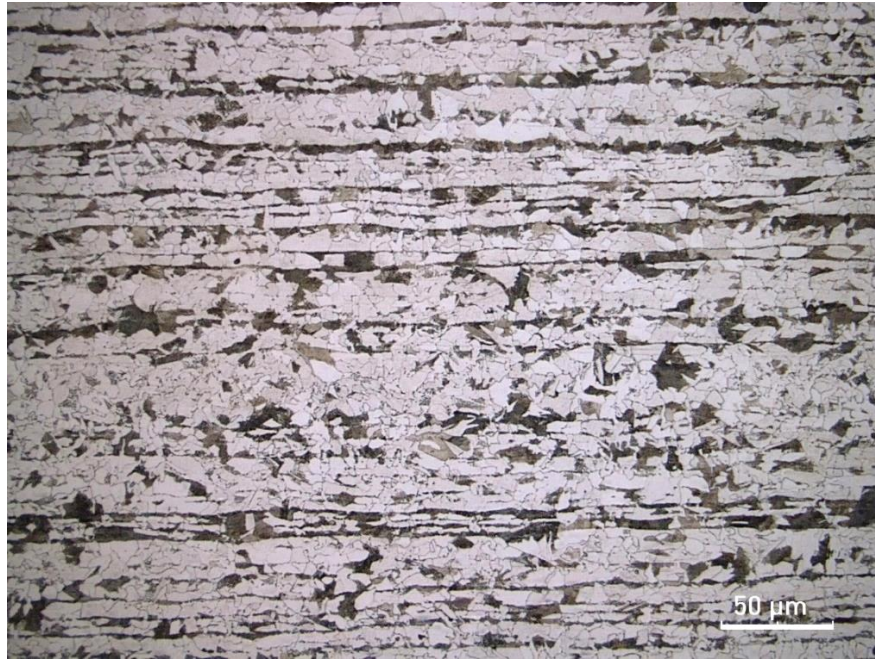


Figure 4.3. Microstructure of Part1. Etched with %2 Nital. Dark regions are pearlite, white regions are ferrite.

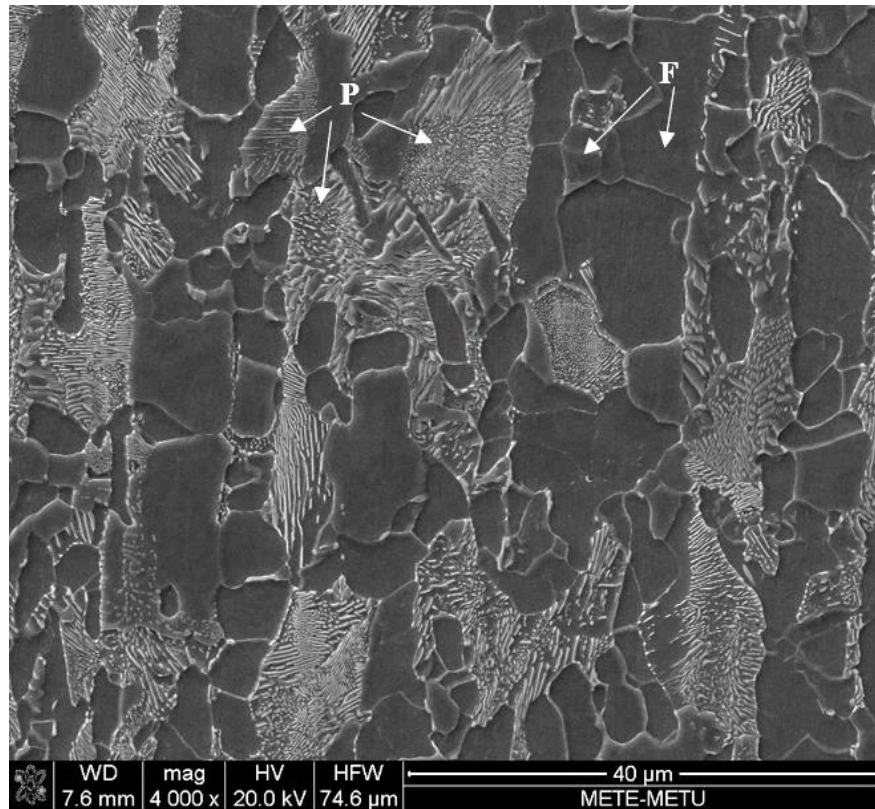


Figure 4.4. SEM image of Part2. F represents ferrite, P represents pearlite.

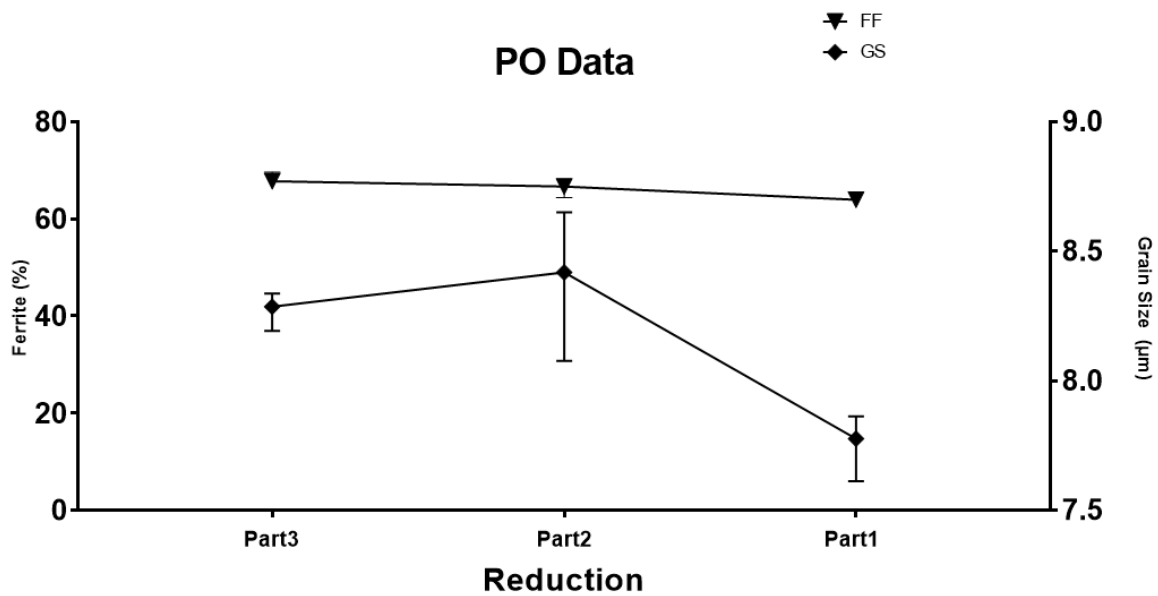


Figure 4.5. Ferrite fraction and grain size of each part prior to cold rolling.

Mechanical properties of PO specimens taken from Part1, Part2 and Part3 regions of the mother coil is given in Figure 4.6. There are slight differences between the mechanical properties, Part1 has the highest tensile strength and Part3 has the lowest. As mentioned above, due to different procedures on cooling rates during coiling, change of ferrite fraction and grain size seems to affect the mechanical properties of the PO samples slightly.

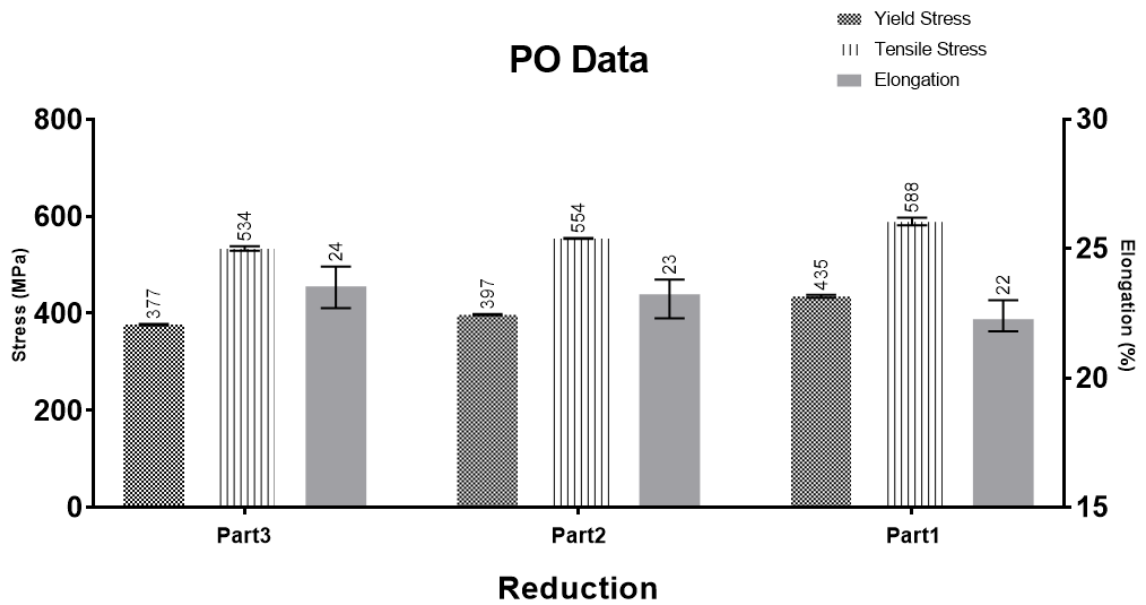


Figure 4.6. Mechanical properties of each part of the PO.

4.2. Microstructures and Mechanical Properties of Cold Rolled Samples

The effect of 30%, 45% and 60% cold rolling on the microstructures can be seen in Figure 4.7, Figure 4.8 and Figure 4.9 respectively. As rolling ratio increases, the aspect ratio of ferrite grains increase. Another effect of cold rolling is fragmentation of pearlite. For 60% CR specimen, broken cementite particles seems to be scattered inside ferrite grains, while this fragmentation is less pronounced in 30% and 60% CR specimens

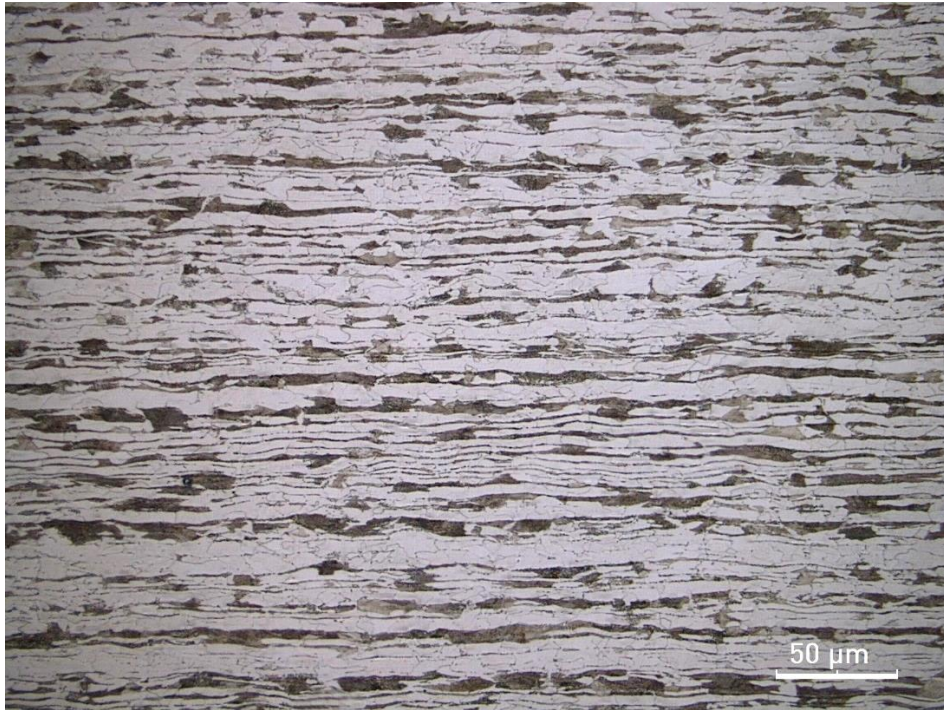


Figure 4.7. 30% CR specimen before heat treatment.

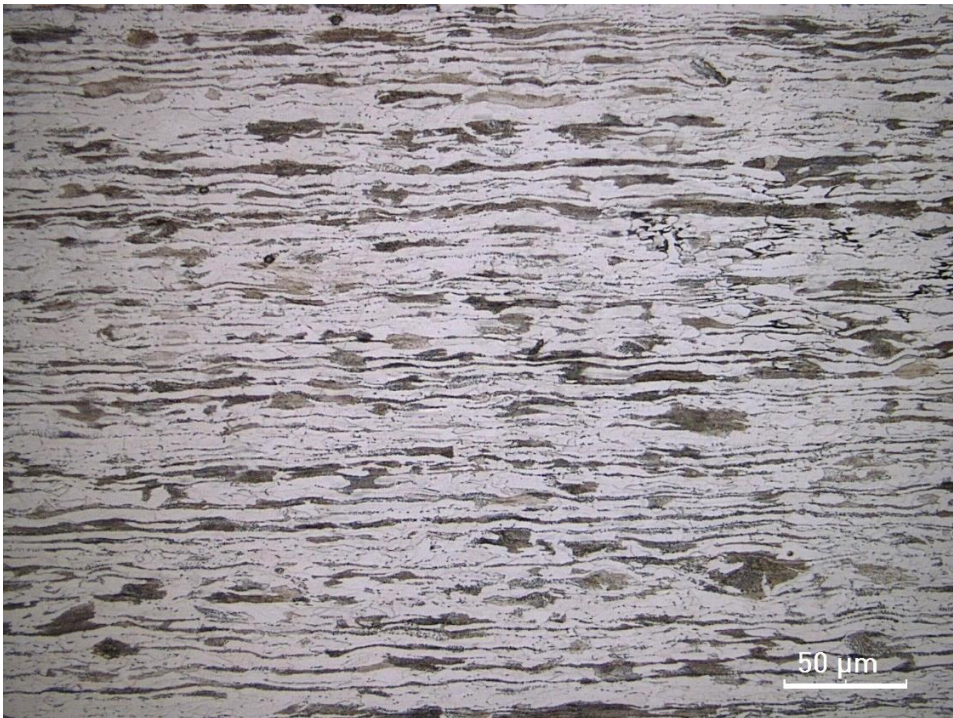


Figure 4.8. 45% CR specimen before heat treatment.



Figure 4.9. 60% CR specimen before heat treatment.

Mechanical properties of cold rolled samples are given in Figure 4.10 and Figure 4.11. As seen, an increase in the amount of cold work causes an increase in yield and tensile strength values but a decrease in % elongation as expected. The 60% cold rolled specimen did not form neck due to excessive amount of cold rolling and failed in a brittle manner. For this reason, yield strength and elongation of 60% cold rolled specimen could not be measured as seen in Figure 4.10. The abrupt increase in hardness of 60% cold rolled sample is seen in Figure 4.11.

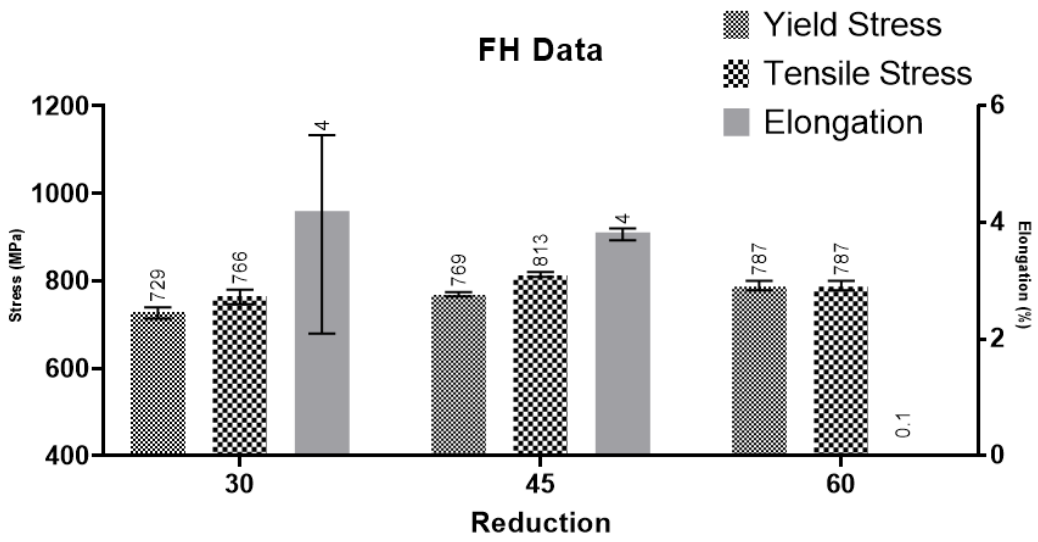


Figure 4.10. Yield strength, tensile strength and elongation of samples after cold rolling.

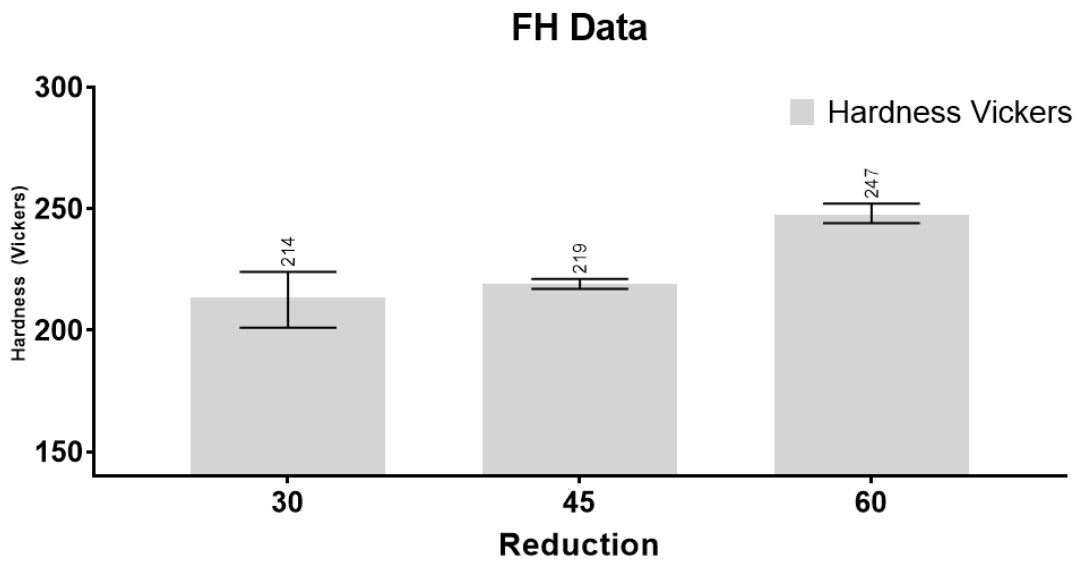


Figure 4.11. Hardness Vickers versus cold reduction ratio.

4.3. The Microstructure and Mechanical Properties of Heat Treated Samples

In order to see the effect of annealing temperature on the mechanical properties and microstructure of the cold rolled specimens, several samples were annealed below and above the intercritical temperature. The heat treatment details are given in Table 4.1.

Table 4.1. Summary of the heat treatments.

	NR HT	30% CR		45% CR		60% CR	
	5 Min	5 Min	10 Min	5 Min	10 Min	5 Min	10 Min
680°C		x	x	x	x	x	x
700°C		x		x		x	
710°C		x		x		x	
720°C	x	x	x	x	x	x	x
730°C		x		x		x	
740°C	x	x	x	x	x	x	x
760°C	x	x	x	x	x	x	x
780°C		x		x		x	
800°C	x	x	x	x	x	x	x

Critical transformation temperatures, A_{c1} and A_{c3} , of the samples are calculated using Eq.2 and Eq.3 are as follows:

A_{c1} : 711,2°C

A_{c3} : 802,2°C

Where A_{c1} is the temperature where austenite is first starts to nucleate upon heating and A_{c3} is the lowest temperature for the composition where the microstructure consists of only austenite. All the specimens are quenched in water after annealing.

4.3.1. Microstructures of Heat Treated Samples

In Figure 4.12 and Figure 4.13, SEM micrographs of 700-30-5 are given. Even at well below A_{e1} temperature, nucleation of austenite phase (which most probably transformed to martensite upon quenching) can be seen at grain boundaries, especially at locations adjacent to prior pearlite or close to carbides.

Thermodynamically, formation of austenite at this temperature is not expected under equilibrium conditions. However, due to composition gradients and short annealing times, austenite formation is favored at carbon rich grain boundaries.

A higher magnification of a prior pearlite region, martensite formation and cementite globularization is given in Figure 4.13. Due to cold deformation, fragmented globular cementite particles are present in the microstructures, which formed as a result of breakdown of several pearlite colonies into smaller, spherical cementite particles. The presence of martensite islands indicate that upon heating at 700°C and waiting for only 5 minutes is enough for formation of austenite islands which transform to martensite upon quenching to room temperature.. With an increase in the amount of cold work the amount of fragmented cementite particles increase such that in 60% CR sample only fragmented cementite particles and martensite is seen besides ferrite grains (Figure 4.14, Figure 4.15). There is no pearlite morphology is observed.

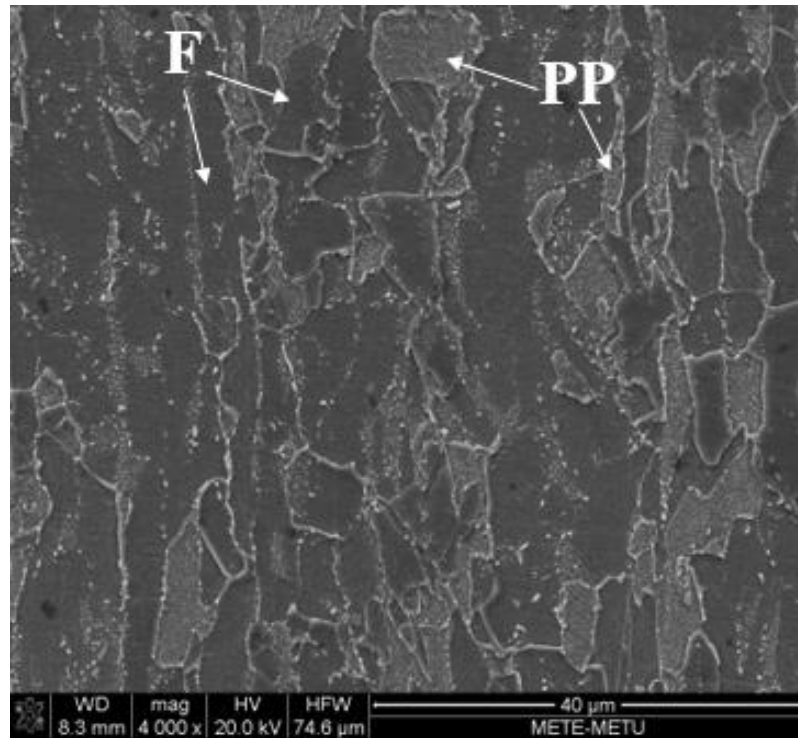


Figure 4.12. Microstructure of 700-30-5. *F* represents ferrite, *PP* represents prior pearlite.

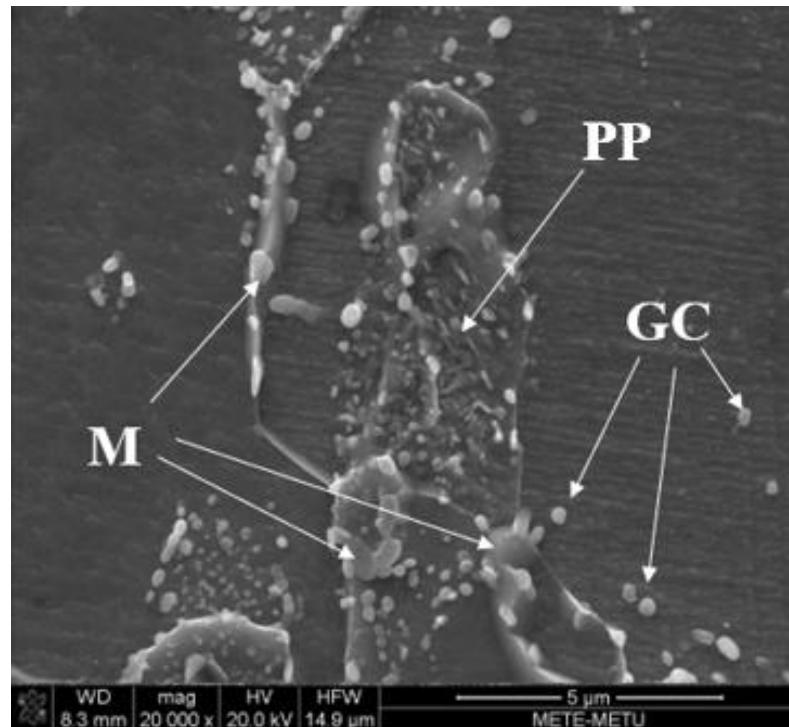


Figure 4.13. High magnification image of 700-30-5. *M* represents martensite, *PP* represents prior pearlite, *GC* represents globular cementite.

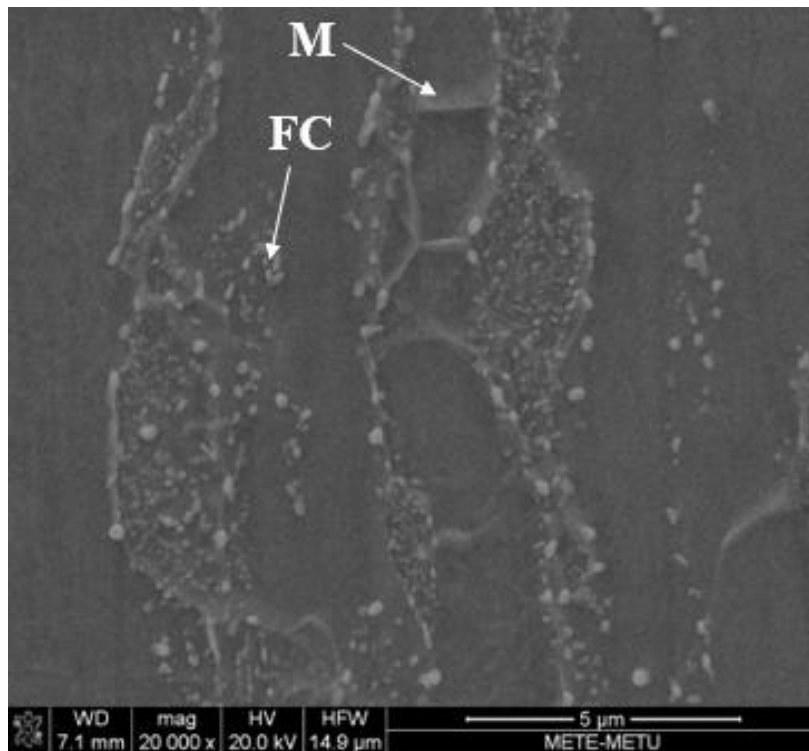


Figure 4.14. SEM micrograph of 700-45-5. M represents martensite, FC represents fragmented cementite.

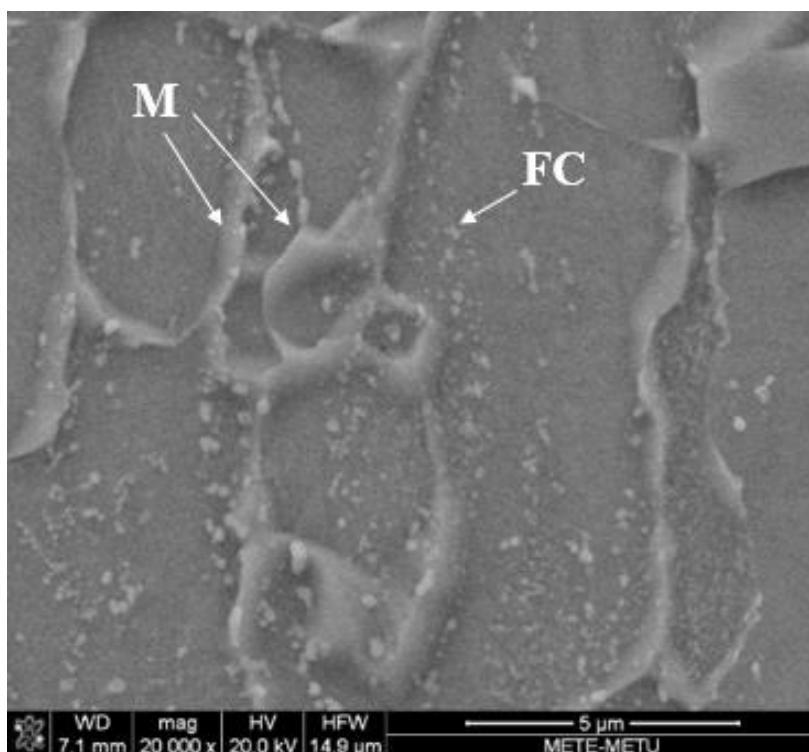


Figure 4.15. SEM micrograph of 700-60-5. M represents martensite, FC represents fragmented cementite.

In Figure 4.16, four different regions where austenite nucleation starts are designated as “1” for ferrite-ferrite grain boundary, “2” for ferrite/pearlite phase boundary, “3” for triple grain boundary and “4” for inside the ferrite grain, in 710-45-5 sample. As discussed before, austenite requires carbon for nucleation, therefore point “2” and “3” are ideal locations for austenite nucleation as diffusion of carbon into austenite is easy from pearlite to austenite, when near a pearlite grain. If given enough time, diffusion of carbon into each other from fragmented cementite and martensite formation is also possible inside a ferrite grain, as seen at point “4”. the transformed fraction of austenite inside the grain is much smaller due to the fact that high energy requirement for homogenous nucleation inside a grain. Finally, due to the low nucleation energy at grain boundaries, austenite nucleation at a ferrite/ferrite grain boundary is also possible and can be seen in point "1".

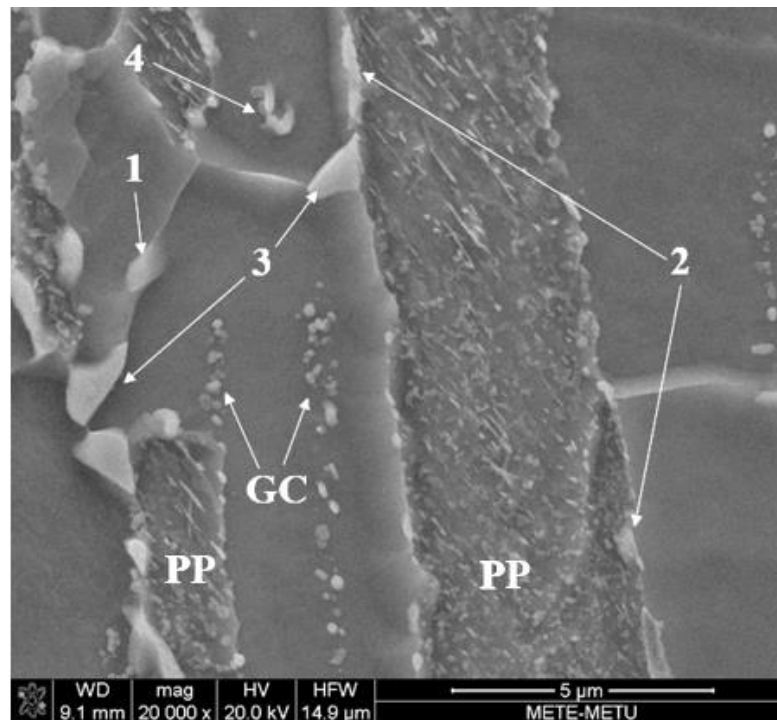


Figure 4.16. SEM image of 710-45-5. GC represents globular cementite, PP represents prior pearlite.

At 730°C, amount of martensite increases mainly by nucleating along grain boundaries, as given in Figure 4.17, Figure 4.18 and Figure 4.19. It can be seen that the sizes of fragmented globular cementite particles in 60% CR sample is finest due to heavy deformation. For 30% sample, due to small amount of deformation, amount of globular cementite particles are lower in amount. The amount of martensite within the ferrite grains is the highest in 45% CR sample when compared to other samples. Shape of ferrite grains are more equiaxed and larger in 45% CR sample than 30% and 60% CR samples. Elongated grains are still pronounced at 30% CR due to higher recrystallization temperature and at 60% CR due to extensive deformation.

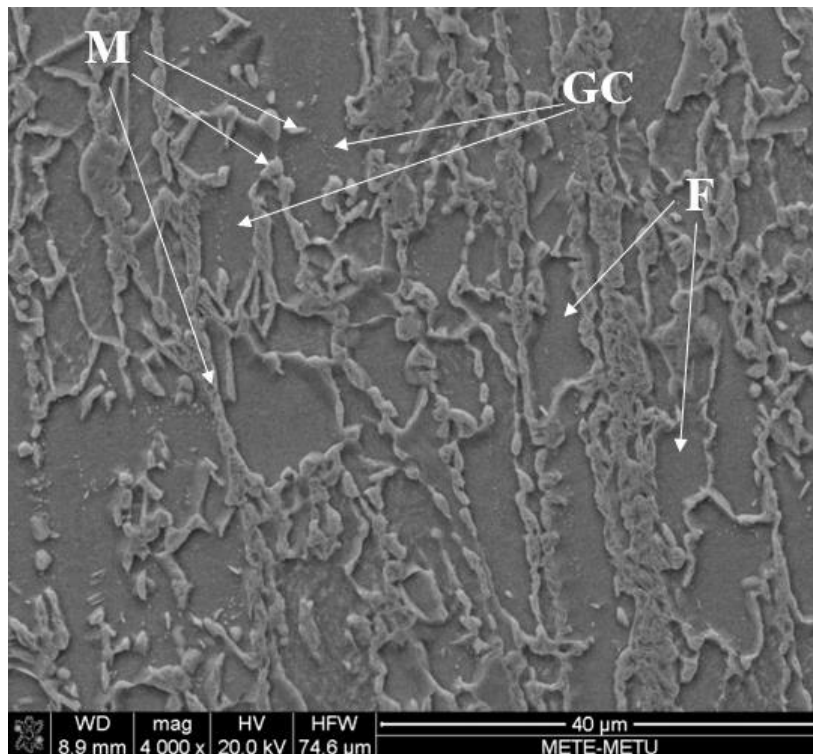


Figure 4.17. SEM image of 730-30-5.

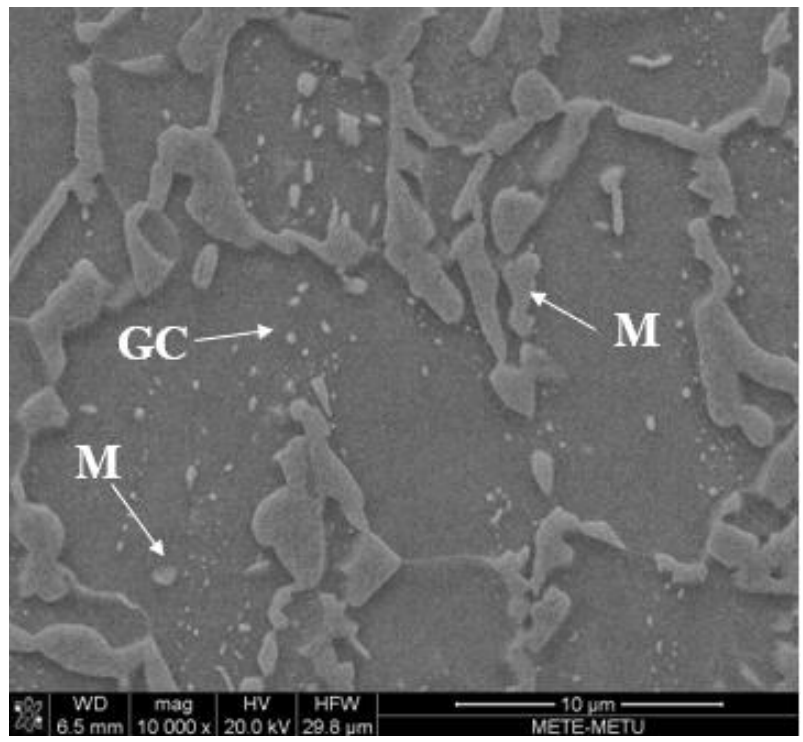


Figure 4.18. SEM image of 730-45-5.

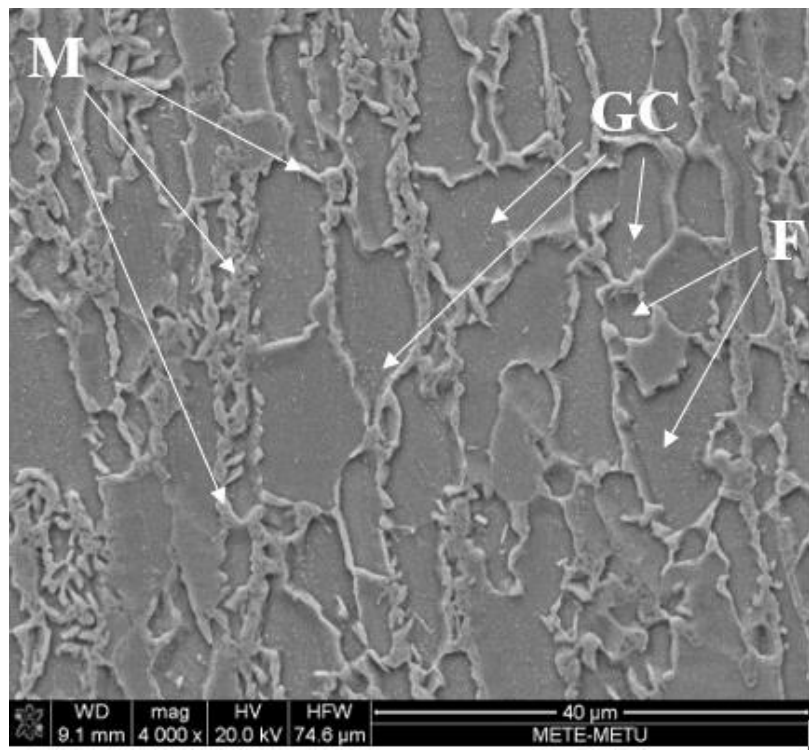


Figure 4.19. SEM image of 730-60-5.

In Figure 4.20, SEM micrograph of 740-45-5 is given. Compared to that of 740-45-10 i.e. 10 minute annealed sample (Figure 4.21), globular cementite particles are less intense in 10 minute sample. Fraction of martensite increased as a result of enabling diffusion of more C and Mn to nearby austenite phases at longer annealing times.

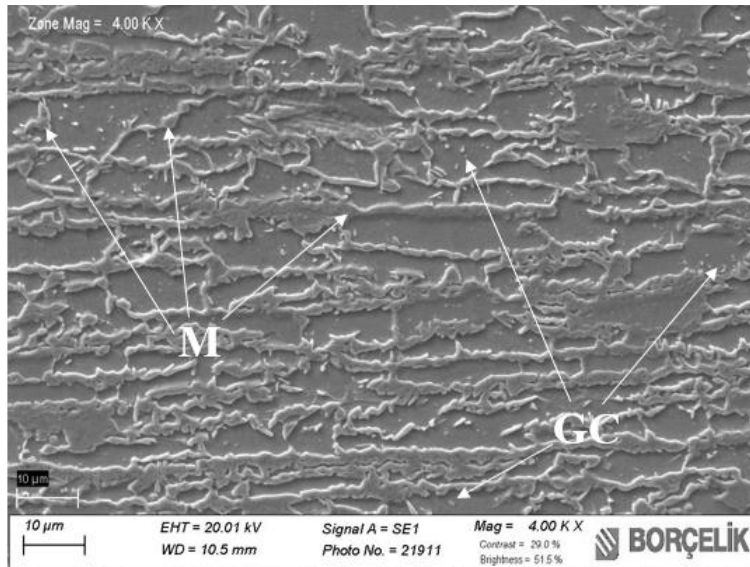


Figure 4.20. SEM micrograph of 740-45-5.

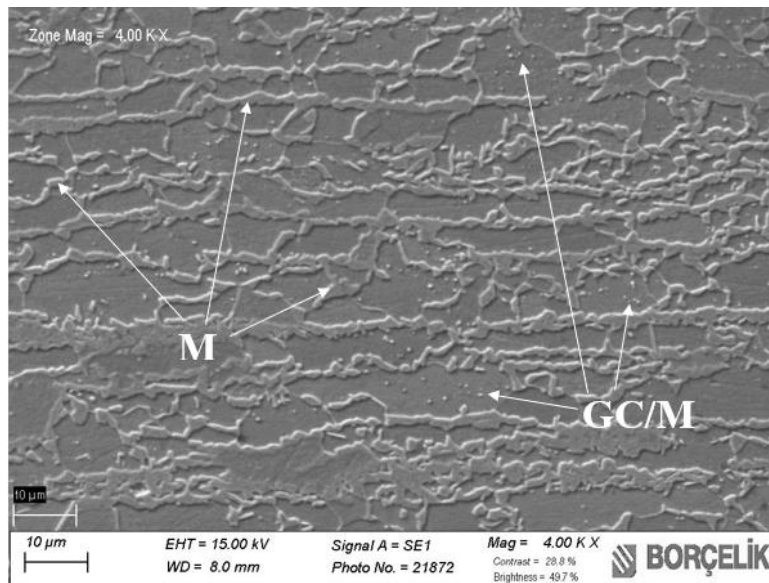


Figure 4.21. SEM micrograph of 740-45-10.

At 800°C, the amount of martensite is significantly higher than samples annealed at lower temperatures, such that the matrix consist of nearly 100% martensitic. The amounts of ferrite in all samples are similar, as given in Figure 4.22, Figure 4.23 and Figure 4.24.

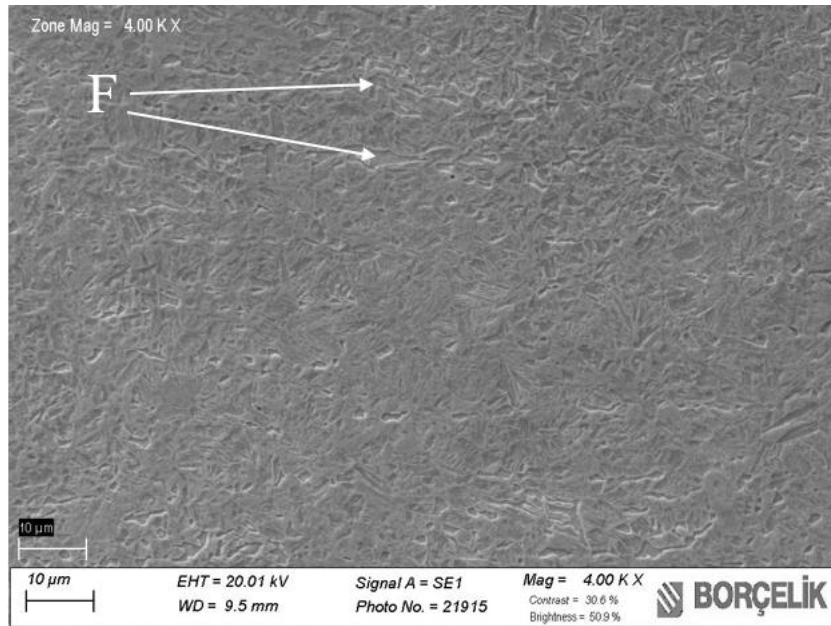


Figure 4.22. SEM image of 800-30-5.

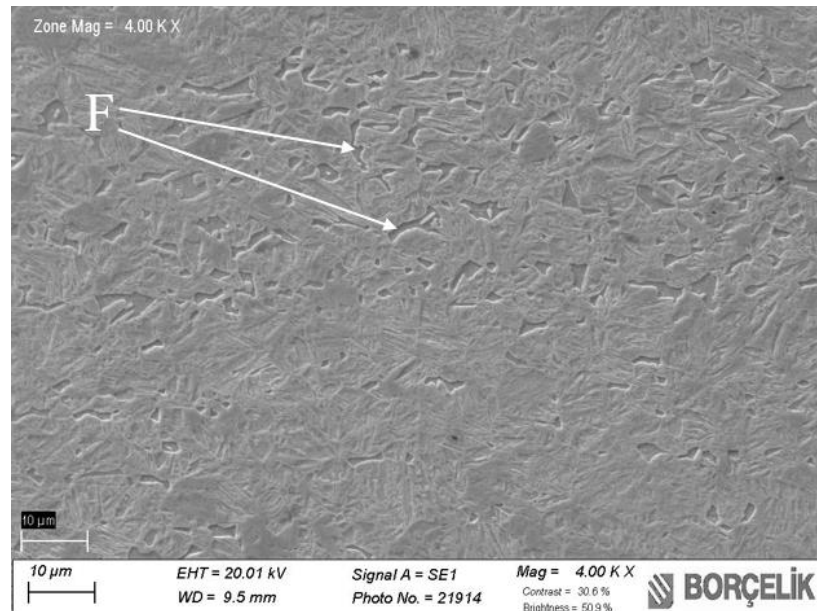


Figure 4.23. SEM image of 800-45-5.

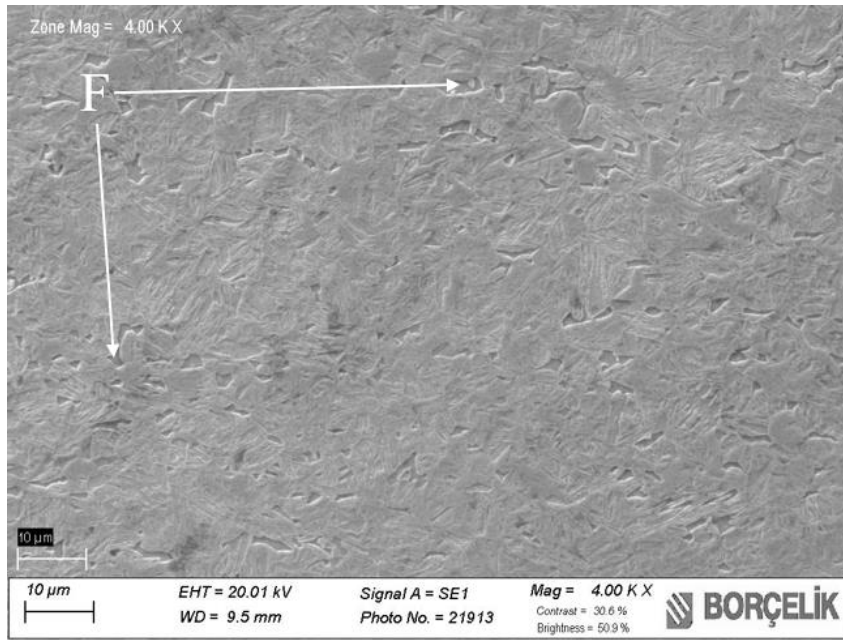


Figure 4.24. SEM image of 800-60-5.

4.3.2. Mechanical Properties

4.3.2.1. 5 Minute Annealed Samples

Mechanical properties of the 5 minute annealed samples are given in Table 4.2, Table 4.3 and Table 4.4. In the table, tensile ductility values are also given. Tensile ductility is a material property, defined with multiplication of tensile strength and fracture ductility of the material. In Figure 4.25 and Figure 4.26, yield and tensile strengths of 5 minute annealed samples are given. As seen, both yield and tensile strength of the samples increase with an increase in annealing temperature. It is worth to notice that both yield strength and tensile strength is similar for 30% and 60% CR samples in the range 680°C-760°C. At high annealing temperatures, it seems that the effect of cold reduction rate becomes more pronounced as tensile strength of 60% CR samples are close and even higher at 800°C than 30% CR specimen. Another point to note is that in the intercritical range, yield and tensile strength of 45% CR specimens, intermediate CR ratio, found to be lowest.

Table 4.2. Mechanical properties of the 5 minute annealed 30% CR samples.

	30% CR			
	YS (MPa)	TS (MPa)	EI (%)	Tensile Ductility (MPa*%EI)
680	546+-20	642+-12	9+-0	5558
700	565+-15	646+-11	7+-0,3	4369
710	419+-26	573+-14	12+-2,5	6967
720	362+-13	568+-4	19+-0,6	11057
730	349+-13	652+-5	13+-0,5	8715
740	405+-27	805+-60	10+-0,9	7862
760	423+-9	867+-11	7+-0,5	6471
780	595+-31	1161+-24	7+-2,4	8245
800	678+-79	1196+-55	6+-0,3	7015

Table 4.3. Mechanical properties of the 5 minute annealed 45% CR samples.

	45% CR			
	YS (MPa)	TS (MPa)	EI (%)	Tensile Ductility (MPa*%EI)
680	417+-17	551+-26	18+-6,6	10055
700	411+-19	546+-18	14+-4,5	7862
710	374+-10	526+-14	23+-1,8	12246
720	313+-11	519+-16	23+-0,6	12085
730	273+-2	585+-9	18+-0,8	10310
740	340+-2	719+-5	13+-0,4	9519
760	384+-3	806+-1,5	8+-0,4	6806
780	506+-27	1052+-38	9+-0,9	8942
800	620+-102	1112+-76	7+-1	7527

Table 4.4. Mechanical properties of the 5 minute annealed 60% CR samples.

	60% CR			
	YS (MPa)	TS (MPa)	EI (%)	Tensile Ductility (MPa*%EI)
680	412+-5	556+-4	17+-3,1	9215
700	394+-32	546+-19	17+-3,6	9500
710	359+-22	540+-2	24+-0,8	12870
720	291+-2	552+-7	21+-0,7	11564
730	268+-1	604+-20	17+-0,3	10363
740	340+-5	716+-12	13+-1,4	9288
760	391+-20	858+-48	10+-0,2	8351
780	575+-16	1143+-19	8+-0,8	8684
800	741+-24	1230+-9	6+-0,5	7011

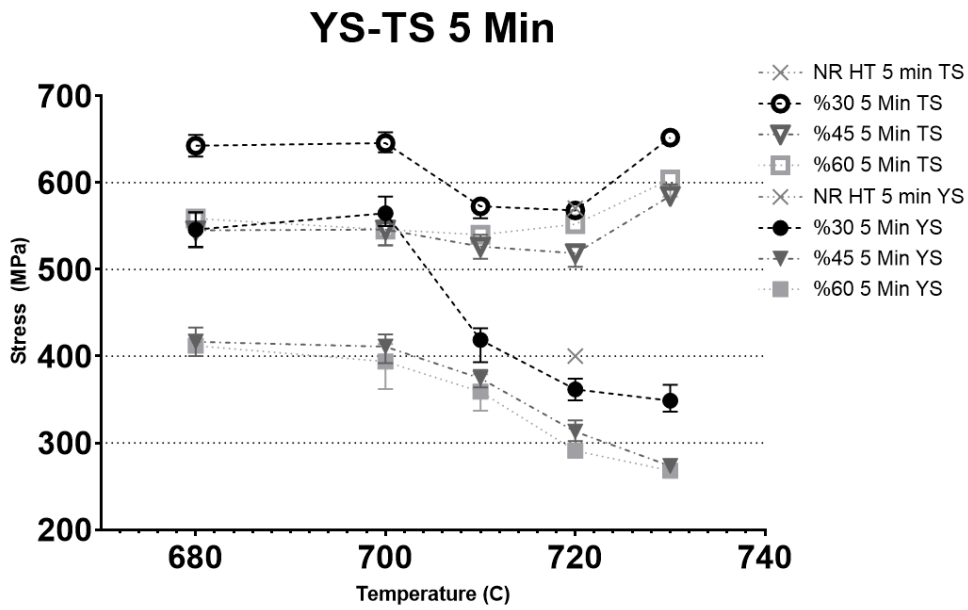


Figure 4.25. Yield Strength and Tensile Strength of 5 minute annealed samples below 740°C.

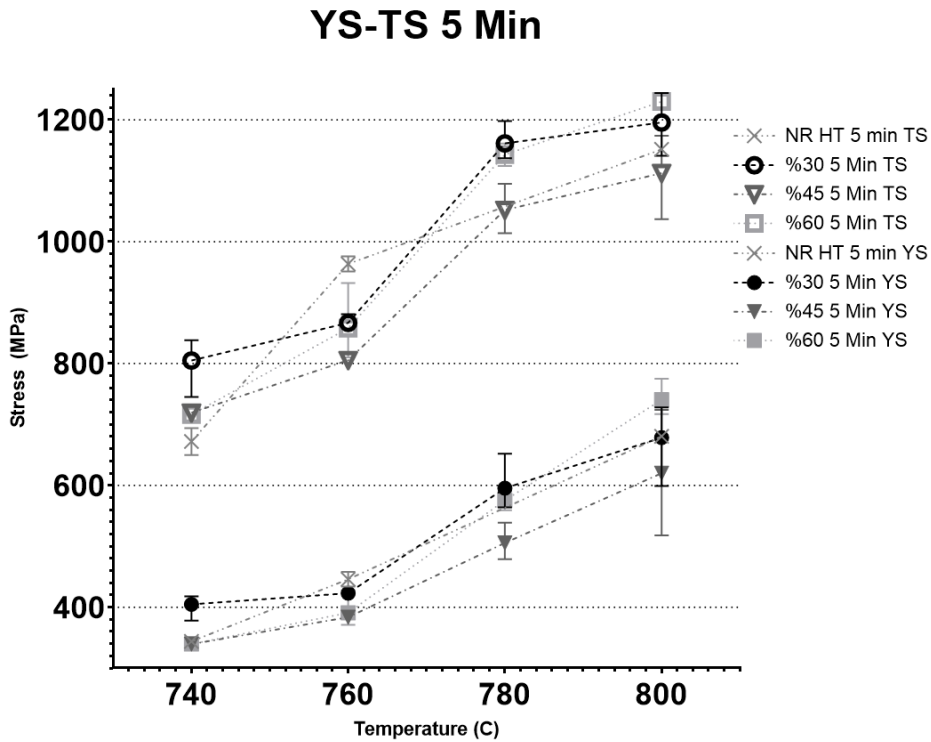


Figure 4.26. Yield strength and tensile strength of 5 minute annealed samples above 740°C.

Ferrite fraction and ferrite grain sizes of the 5 minute soaked samples are given in Figure 4.27 and Figure 4.28. As expected, the amount of ferrite decreases with an increase in annealing temperature in agreement with Fe-Fe₃C phase diagram. This leads to an increase in yield and tensile strength in all samples.

In 30% and 45% CR samples, a scattered and similar ferrite grain size pattern is seen until 760°C. Similar grain sizes for 45% and NR HT between 720°C and 760°C samples indicate that, recrystallization is almost completed in 45% CR sample. Above 760°C, ferrite grain size for all samples start to drop dramatically. The ferrite grain size is smallest for the 60% CR sample at all temperatures.

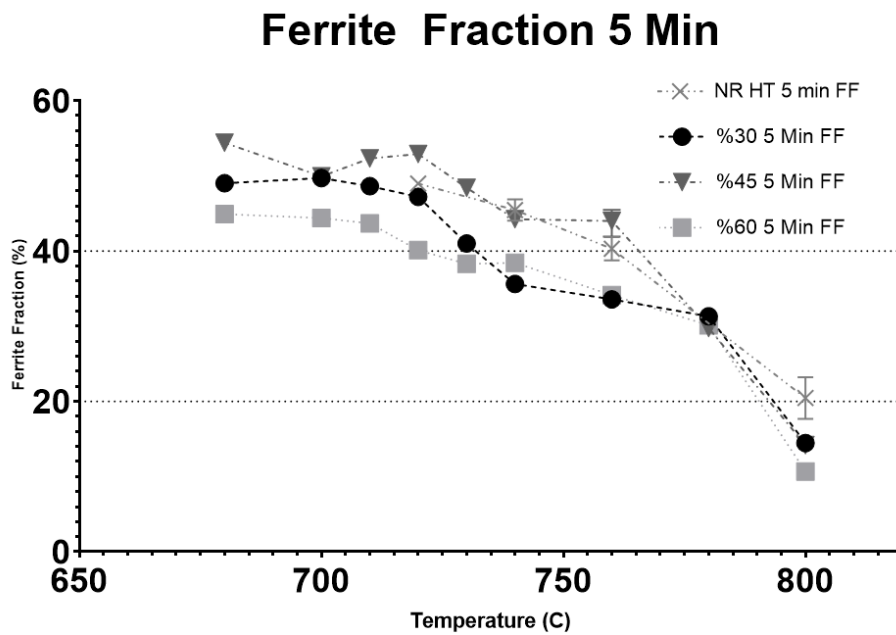


Figure 4.27. Ferrite fraction of 5 minute annealed samples.

Grain Size 5 Min

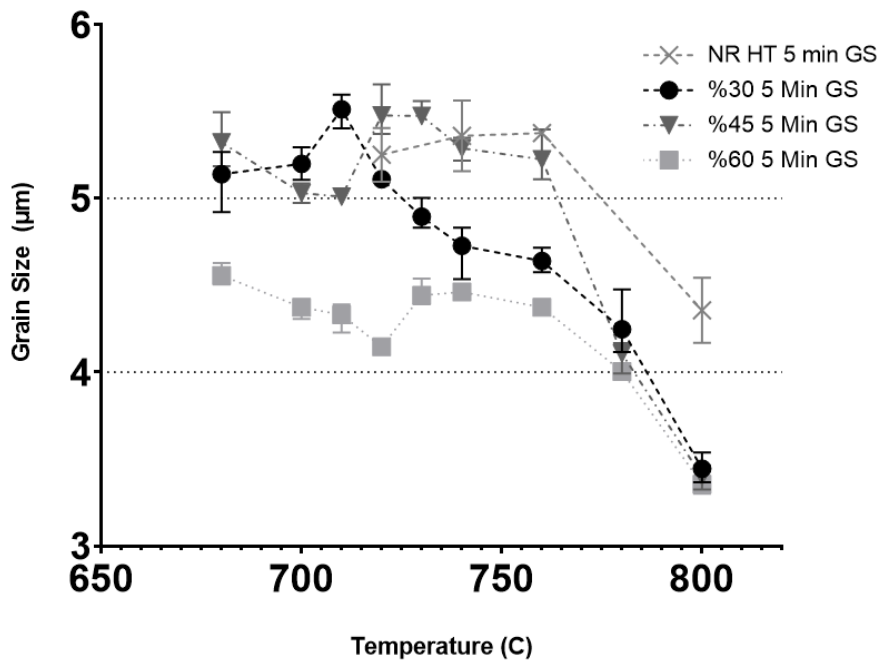


Figure 4.28. Ferrite grain sizes of 5 minute soaked samples.

%Elongation versus annealing temperature plot is given in Figure 4.29. The dependence of elongation on the annealing temperature is similar to yield and tensile strength behavior. As the strength of the sample increases, the elongation decreases.

Elongation 5 Min

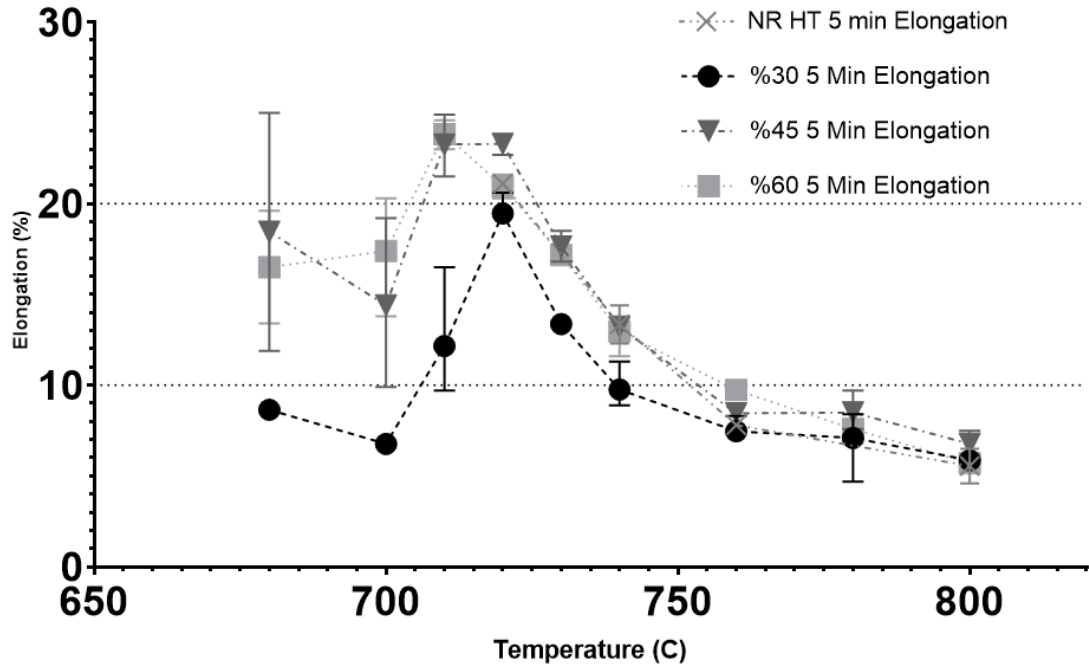


Figure 4.29. Temperature versus elongation for 5 minute annealed samples.

4.3.2.2. 10 Minute Heat Treatments

Mechanical properties of the 10 minute annealed samples are given in Table 4.5, Figure 4.30 and Figure 4.31. The tensile strength of 10 minute soaked samples are given in Figure 4.30. Increasing soaking time from 5 minute to 10 minute did not seem to change relationship between tensile strength, reduction ratio and annealing temperature. 30% CR samples show highest tensile strength up to 800°C, while 45% CR samples show the lowest tensile strength. At 800°C, tensile strength of all samples are similar. This could be an indicator of that, if enough time is given at high annealing temperatures, the effect of cold reduction on the tensile strength become negligible.

Also at high temperatures the amount ferrite become so low that the martensite phase dominate the properties (Figure 4.32).

Table 4.5. Mechanical properties of the 10 minute annealed samples.

	30% CR				45% CR				60% CR			
	YS (MPa)	TS (MPa)	El (%)	Tensile Ductility (MPa*% El)	YS (MPa)	TS (MPa)	El (%)	Tensile Ductility (MPa*% El)	YS (MPa)	TS (MPa)	El (%)	Tensile Ductility (MPa*% El)
680	429±5	579±7	15±0,8	8579	388±12	528±22	21±1,3	11305	393±7	534±2	23±1,5	13880
720	307±5	580±17	18±0,4	14928	288±20	550±10	21±0,6	15077	275±5	607±7	17±0,8	13771
740	408±18	845±21	9±0,6	9308	342±7	726±22	13±1	11674	386±6	812±7	11±0,9	10774
760	523±9	1074±7	6±0,6	8062	397±4	869±9	10±1,2	11872	432±9	942±10	9±1	10724
800	951±27	1280±37	5±1	8579	879±80	1250±12	5±0,3	11305	713±59	1247±52	5±0,1	13880

YS-TS 10 Min

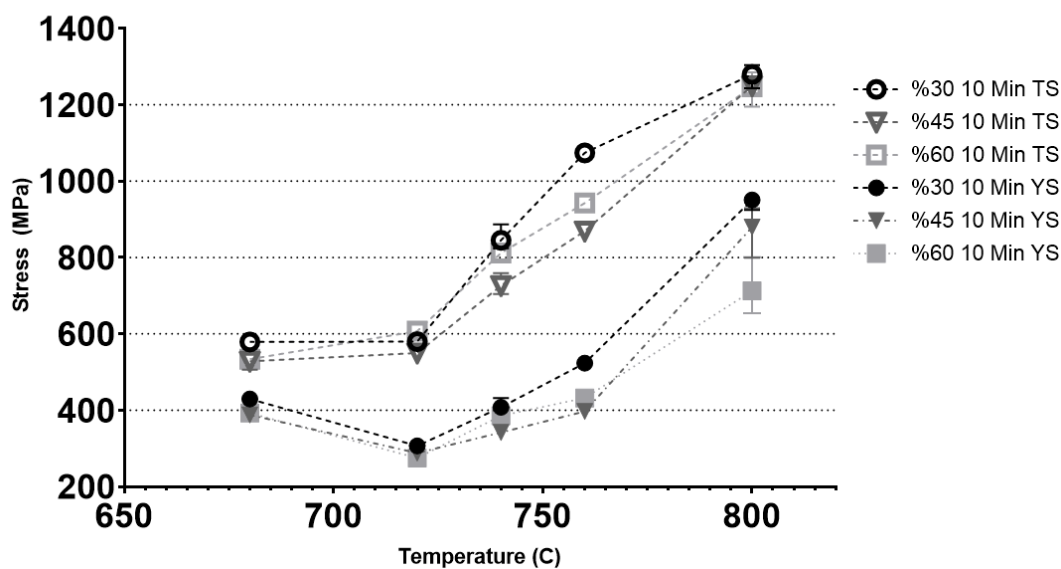


Figure 4.30. 5 minute and 10 minute soaking time effect on the tensile strength.

Temperature EI 10 Min

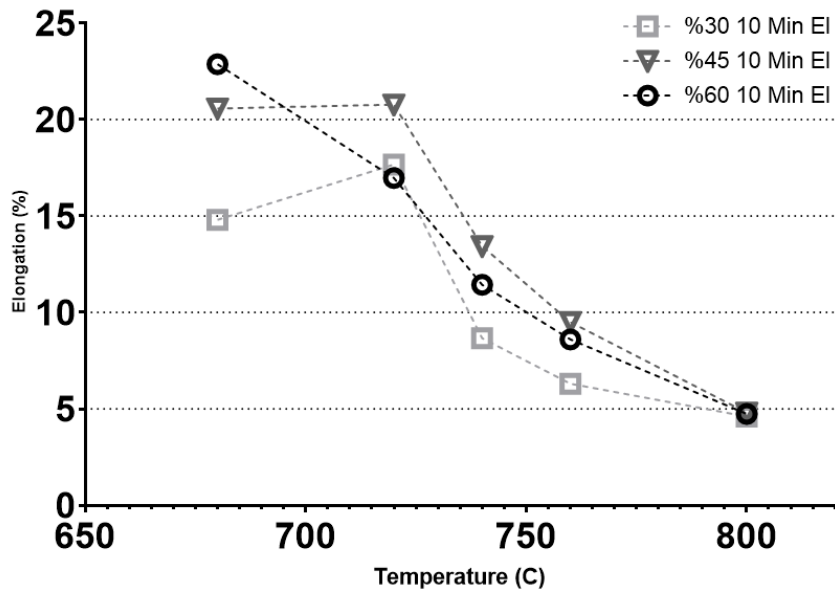


Figure 4.31. Temperature-Elongation plot of 10 minute annealed samples.

Ferrite fractions and ferrite grain sizes of 10 minute annealed samples are given in Figure 4.32 and Figure 4.33. The ferrite fraction of samples are in similar trend with 5 minute annealed samples, such that, as temperature increases, ferrite fraction decreases. Grain sizes also change in a similar manner with 5 minute annealed samples. A reduction in grain size is seen as temperature increases. The grain size of 60% 10 min sample always has the smallest grain size.

Ferrite Fraction 10 Min

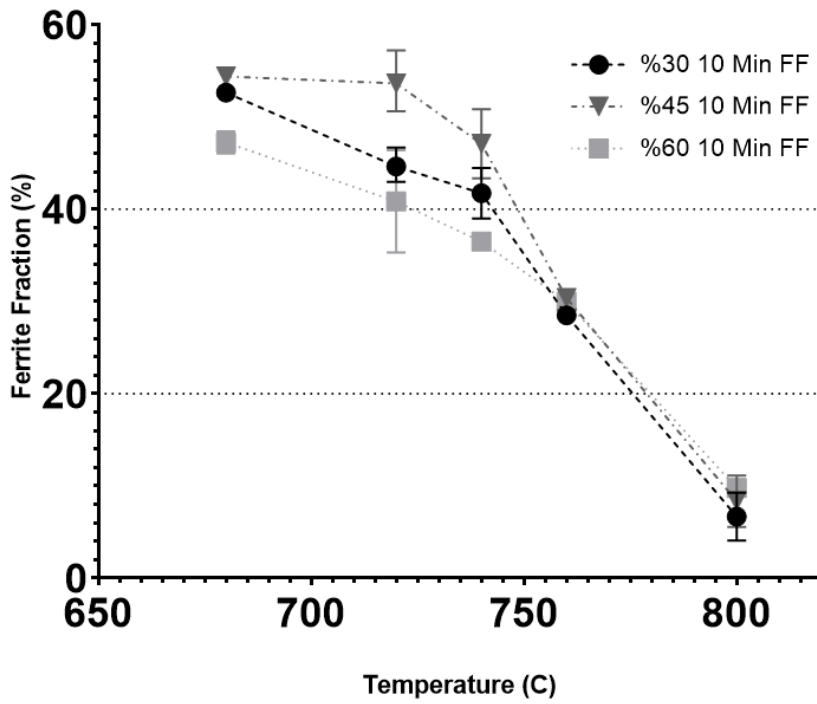


Figure 4.32. Ferrite fractions of 10 minute annealed samples.

Grain Size 10 Min

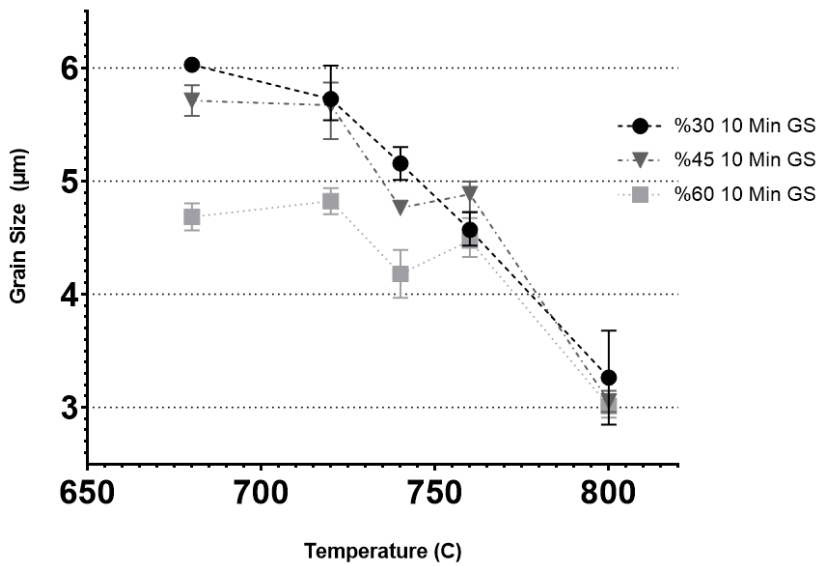


Figure 4.33. Ferrite grain sizes of 10 minute annealed samples

CHAPTER 5

DISCUSSION

5.1. Recrystallization of Ferrite

The resulting effect of increased cold rolling ratio on the recrystallization can be divided into 2 groups. The first one is the reduction of recrystallization temperature. When comparing 30% and 45% CR samples at 680°C, light microscope images show clear difference in aspect ratio of ferrite grains (Figure 5.1, Figure 5.2). So, it can be concluded that lower recrystallization temperature of 45% CR resulted in recrystallization of the sample at an earlier stage and resulted in more equiaxed ferrite grains. Aspect ratios of samples up to 720°C is given in Figure 5.3.



Figure 5.1. Light Microscope image of 680-30-5. Dark regions are pearlite, white regions are ferrite.



Figure 5.2. Light Microscope image of 680-45-5. Dark regions are pearlite, white regions are ferrite.

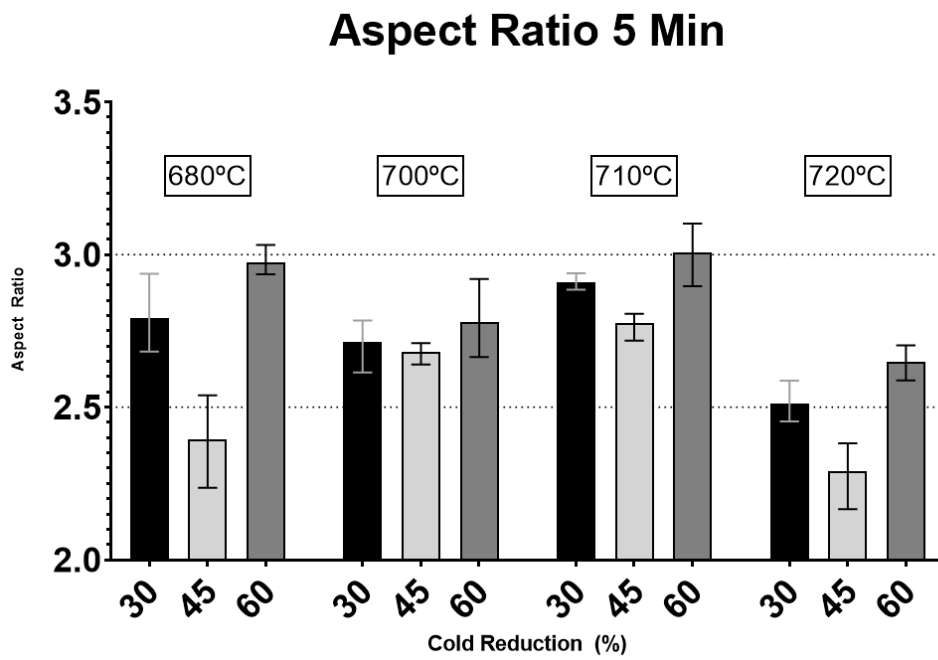


Figure 5.3. Ferrite aspect ratios of 5 minute annealed samples up to 720°C.

The other effect of cold rolling ratio on the recrystallization is related to the grain sizes. Heavy deformation resulted in excessive elongation of grains. Upon annealing, recrystallization of heavy deformed samples started earlier and due to high driving force for nucleation, many small ferrite nuclei formed. When the annealing time is short, and grain growth is not completed, grain sizes of ferrite remained small. When the 45% and 60% CR samples annealed at 680°C is compared, it is seen that the grain size of 60% CR samples are smaller (Figure 5.2, Figure 5.4). Despite heavy deformation, only a few deformed ferrite grains can be seen at 700°C, indicating that recrystallization is almost completed. Emadoddin has stated that upon annealing of 65%, 76% and 84% CR DP samples with the same parameters, elongated grains are still present in 84% CR sample [71]. The reason for that is related to the need of more time or higher temperature for the elimination of elongated texture, even though the recrystallization temperature is lower in 84% CR sample.



Figure 5.4. Light Microscope image of 680-60-5. Dark regions are pearlite, white regions are ferrite.

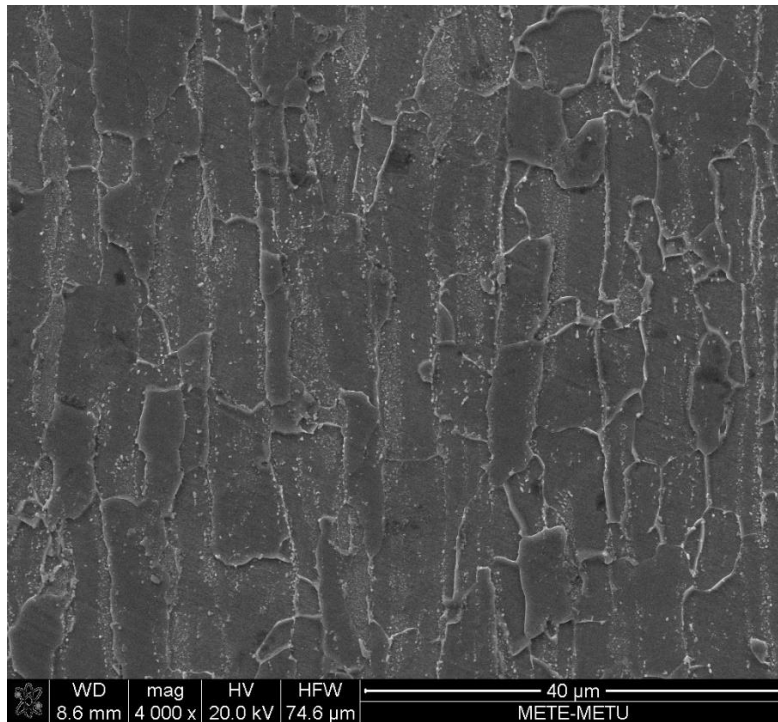


Figure 5.5. SEM image of 700-60-5 at 4000x. No deformed ferrite is observed.

As a result, due to the combined effect of lower recrystallization temperature than 30% CR samples and lower deformation ratio than 60% CR samples, it is probable that 45% CR samples have the fastest overall recrystallization kinetics and the largest grain sizes. Comparing tensile strengths at 680°C and 700°C, it is seen that non recrystallized, deformed ferrite yields higher tensile strength values (Figure 5.6).

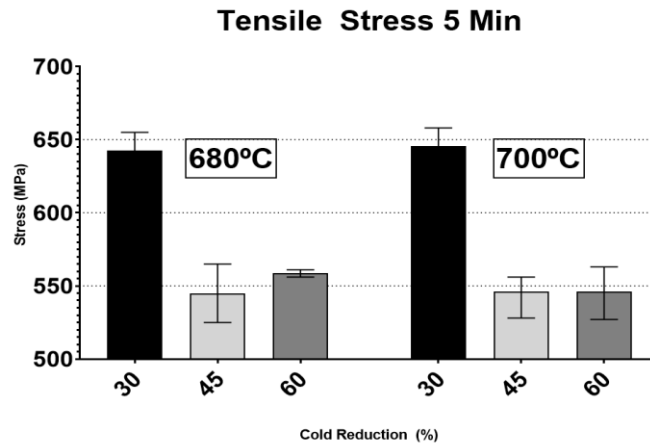


Figure 5.6. Tensile strength of samples at 680°C and 700°C.

5.2. Nucleation of Austenite

In this study, SEM images of cold rolled and annealed samples revealed that the austenite mainly starts to nucleate at grain boundaries. In the starting microstructure, 2 types of boundary exist: Ferrite/Ferrite and Ferrite/Cementite. As pearlite has a lamellar structure with alternating layers of ferrite and cementite, this phase consists of higher amount of ferrite/cementite boundaries.

The solubility of C in ferrite is maximum at A1 temperature and decreases with an increase in annealing temperature. So upon heating above A1 temperature, ferrite has to reject the excess carbon in order to stay stable. The nearest region for C to diffuse is grain boundaries. Therefore, whether it is ferrite/ferrite or ferrite/cementite boundary, there will be C atoms which were rejected from adjacent ferrite grains.

Austenite requires C atoms to nucleate and growth. In the case of ferrite/cementite boundary, cementite is the main C supplier for nucleation and growth so these grain boundaries are favored. In the case of ferrite/ferrite boundary, the work of Savran et al (Savran, et al., 2007) helps to understand the nucleation. They reported that, C rejected from adjacent ferrite grains provide C for austenite nucleation at ferrite/ferrite

grain boundaries. Additionally, C depleted ferrite grains provide C from nearby dissolved cementite particles, providing a constant flow of C to austenite at ferrite/ferrite grain boundaries. They also argued that austenite formation is possible even below equilibrium austenite C content and found differences in C content which were nucleated on ferrite/ferrite grain and on ferrite/cementite grain. [72]. Growth of austenite along grain boundaries could therefore be explained as high C content of ferrite/ferrite and ferrite/cementite grain boundaries.

In all cases, nucleation of austenite inside a prior pearlite is almost never the case. Even though, pearlite consists of many ferrite/cementite grain boundaries, which are favored for austenite nucleation, austenite grains formed at low temperatures have some sides that are free from C atoms. This phenomena may be explained by the fact that, due to high amount of C at the core of the pearlite, these atoms are unable to dissolve and diffuse as the surrounding regions also have high amounts of C atoms. In the case of scattered cementite particles however, austenite nucleation is relatively easier as there is enough space for C to diffuse away and form austenite. SEM images of samples annealed at 720°C are given in Figure 5.7, Figure 5.8 and Figure 5.9. It is important to note that even at prior pearlite bands, austenite is covering almost all the grain boundaries. It seems that the nucleation of austenite is first favored mainly at grain boundaries that are adjacent to ferrite grains. Lower interfacial energy of ferrite/ferrite and ferrite/pearlite grain boundaries or insufficient space for rejection of carbon within pearlite grains during transformation to austenite phase could be the reason for almost no austenite formation within the pearlite colonies and bands.

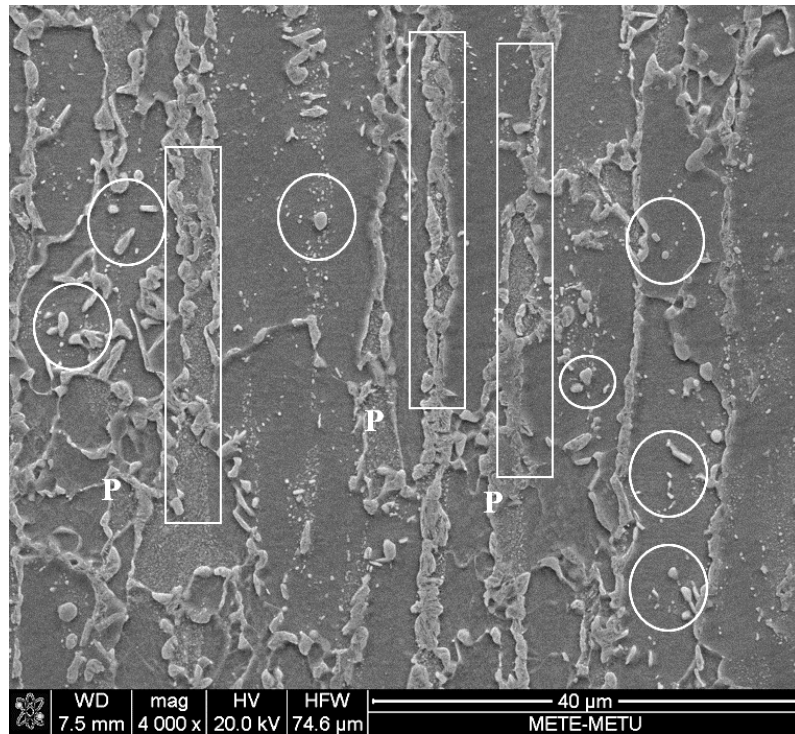


Figure 5.7. SEM image of 720-30-5. White circles represent austenite formation from agglomeration of fragmented cementite particles, white rectangles represent prior pearlite bands, P represents Pearlite.

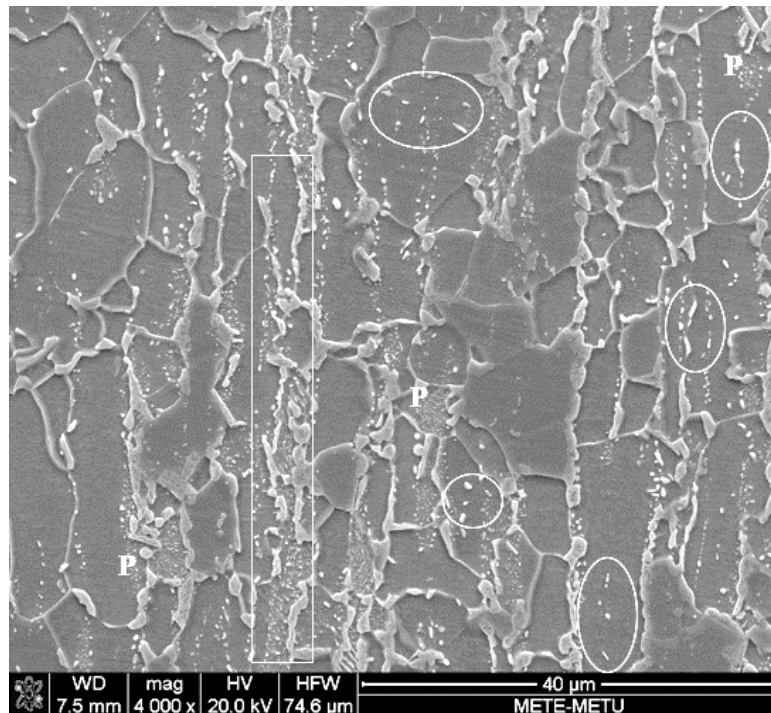


Figure 5.8. SEM image of 720-45-5. White circles represent austenite formation from agglomeration of fragmented cementite particles, white rectangles represent prior pearlite bands, P represents Pearlite.

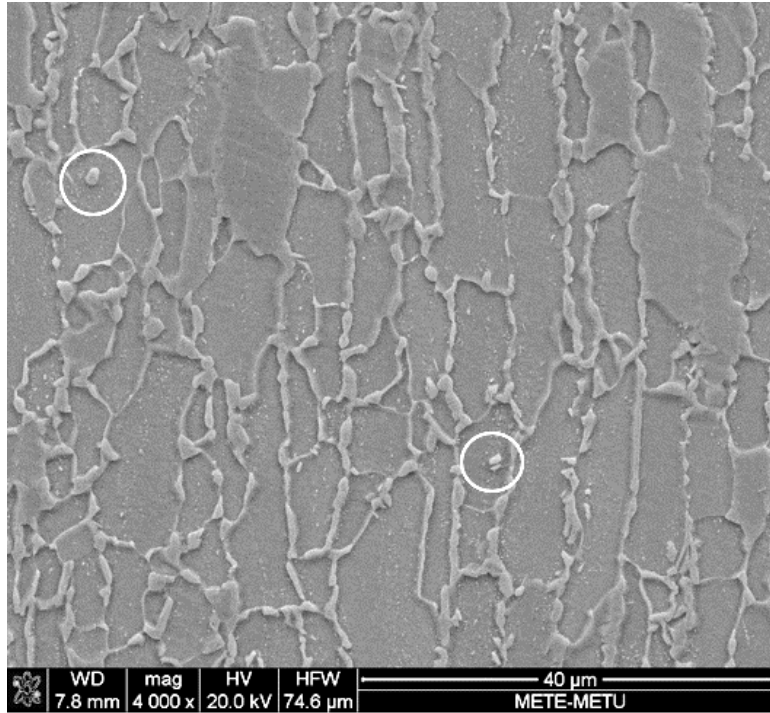


Figure 5.9. SEM image of 720-60-5. White circles represent austenite formation from agglomeration of fragmented cementite particles. Note that these particles are considerably lower in amount than 30% and 45% CR samples.

John-Mehl-Avrami-Komologgov equation, also called JMAK equation, could be used in order to study the apparent activation energy for austenite growth. Generally, it is assumed that if the calculated activation energies for processes are lower than the activation energy of Mn diffusion in austenite, the process is not dominated by the Mn diffusion, but dominated by C diffusion. JMAK equation is given below:

$$V_{\gamma} = 1 - e^{-kt^n} \quad \text{Eq.6}$$

Where, V_{γ} is the austenite volume fraction, k is the temperature dependent growth rate constant, n is the JMAK exponent. Integrating both sides, a more common version is obtained:

$$\ln\left(\ln\left(\frac{1}{1-\alpha}\right)\right) = \ln k + n \ln t \quad \text{Eq.7}$$

where α is the austenite fraction and t is the annealing time. In order to calculate the apparent activation energy, some researchers replaced k with an Arrhenius equation as this parameter is temperature dependent [73] [74] [75] [76]:

$$K = A * e^{\frac{-Q}{RT}} \quad \text{Eq.8}$$

Where Q is the apparent activation energy for the diffusion-controlled austenization. Taking integral of the both sides:

$$\ln K = \ln A - \frac{Q}{RT} \quad \text{Eq.9}$$

Integrating Eq.7 and Eq.9, we obtain:

$$\ln\left(\ln\left(\frac{1}{1-\alpha}\right)\right) = \ln A + n \ln t - \frac{Q}{RT} \quad \text{Eq.10}$$

Plot of the $\ln\left(\ln\left(\frac{1}{1-\alpha}\right)\right)$ versus $-1/T$ graph gives us a line with a slope of Q/R and with an intercept of $\ln A + n \ln t$. In order to plot the graph, it is assumed that, all cementite particles are dissolved above 740°C and the matrix only contains ferrite-martensite. Plotted graphs are given in Figure 5.10 calculated values are given in Table 5.1.

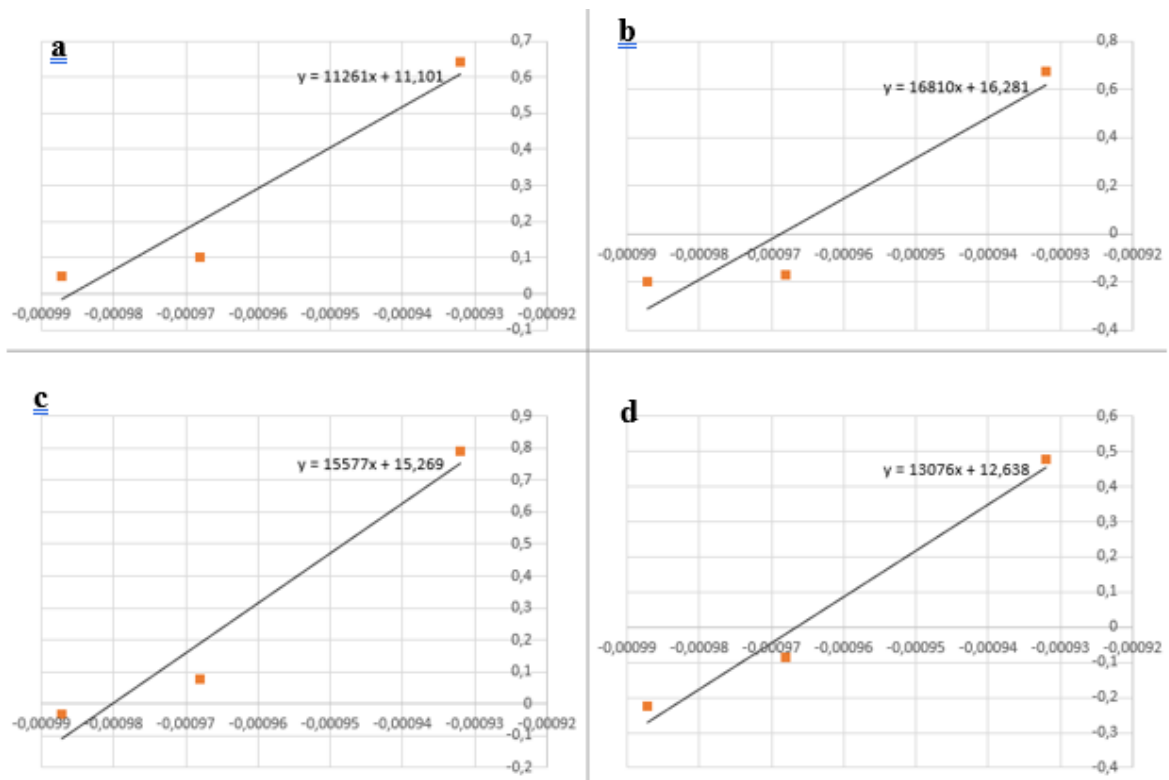


Figure 5.10. Plotted graphs for calculation of Q values. a) 30% CR, b) 45% CR, c) 60% CR, d) NR HT. Vertical lines correspond the \ln function in Eq.10, horizontal lines correspond the $-1/T$ values.

Table 5.1. JMAK values of samples.

	740C		760C		800C		Q kJ/mol
	α	$\ln(\ln(\frac{1}{1-\alpha}))$	α	$\ln(\ln(\frac{1}{1-\alpha}))$	α	$\ln(\ln(\frac{1}{1-\alpha}))$	
NR	0,45	-0,225	0,40	-0,0874	0,2	0,47588	108,68
30%	0,35	0,04862	0,33	0,10315	0,15	0,64034	93,63
45%	0,44	-0,1973	0,43	-0,1696	0,14	0,67606	139,76
60%	0,38	-0,033	0,34	0,07586	0,11	0,79176	129,48

Comparing these results (for 0.14C-1.98Mn-0.2Si-0.25Cr) with the work of Mazaheri et al. (calculated apparent activation energy is given as 246.9 kJ/mol for a 0.15C-1.15Mn-0.4Si-0.95Cr steel), the activation energies in this study is found to be much

lower. Lower apparent activation energy found in this study could be explained by the low amount of elements such as Si and Cr, which could increase nucleation incubation time [77]. Another possible reason is that, due to the starting microstructure in this study is ferrite-pearlite, while the work of Mazaheri et al. has ferrite-martensite, cold deformation could have caused fragmentation of pearlite, causing more homogeneous carbon distribution within the microstructure.

Comparing the calculated activation energies with carbon diffusion in ferrite and austenite, 84 kJ/mol and 157 kJ/mol, respectively, it can be concluded that the austenite formation was primarily governed by diffusion of carbon from ferrite or pearlite to grain boundaries. Increase of hardenability of austenite grains by carbon diffusion to austenite and homogenization may have taken place in 45% CR sample, as 45% CR and carbon diffusion in austenite activation energies are close to each other. Finally, when considering Mn diffusion in austenite, which has an activation energy of 284.1 kJ/mol, this mechanism did not seem to have influenced the austenite formation very much.

Using the calculated activation energies, it may be possible to calculate the amount of martensite where pearlite decomposition is not finished. Before this calculation, the amount of austenite particles' effect on the apparent activation energy is assumed to be zero. Also, the apparent activation energy is assumed to be constant and the same at lower temperatures. To be able to compare with the real values, 720-NR-5 sample is processed with MIPAR, and cementite fraction is measured, using color cluster and range threshold, and found as 11% (Figure 5.11). Note that due to fragmentation of cementite particles and elongation of grains, carbide or martensite fraction measurements of CR samples are not as successful as NR samples. Sum of the ferrite and cementite fractions of 720-NR-5 samples are 60%, therefore leaving approximately 40% martensite in the microstructure. Putting the $-1/T$ value as $-0,00101$, \ln function becomes $-0,53018$. The martensite fraction which equates the \ln function to $-0,53018$ is 44%, which is 4% higher than the measured value. This reason of the difference is most probably that the assumptions are not entirely correct and

there are other factors that affect the apparent activation energy with changing temperature. However, close calculated and measured values might be an indication of reliability of this method. Still, the calculated values are empirical and should be further studied for their validity.

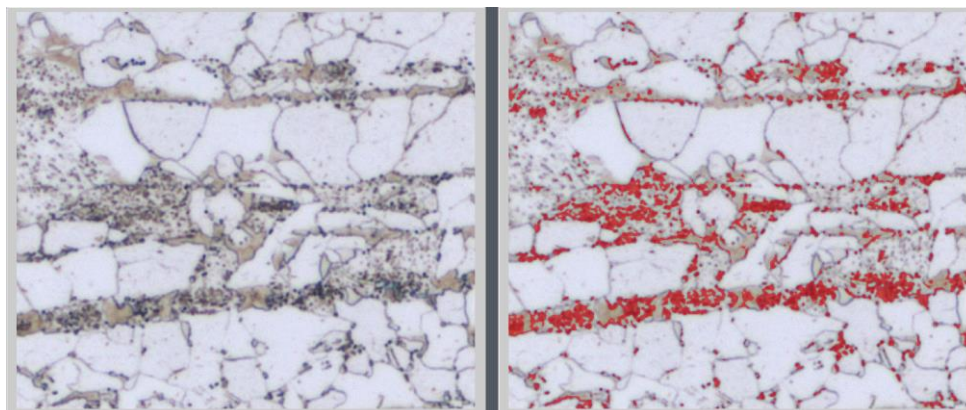


Figure 5.11. Carbide fraction determination with MIPAR in 720-NR-5.

5.3. Mn Partitioning at 740°C, 760°C and 780°C

Thermo-Calc calculations for Mn partitioning and growth of ferrite/austenite phase at 740°C, 760°C and 780°C for 5 and 10 minute of soaking times for 0.14C-1.98Mn steel are given in Figure 5.12, Figure 5.13 and Figure 5.14. Initial Mn and C content of the ferrite phase is given as 1.5% and 0.012%, initial Mn and C content of the austenite phase is given as 2.1% and 0.232%, respectively. The calculations represent Mn a grain boundary movement that is adjacent to ferrite and austenite phases with above given initial compositions.

It is convenient to assume that, at temperatures lower than 780°C, the rate of partitioning of Mn to austenite is limited by the slower diffusion speed of Mn in austenite than in ferrite. In their calculations, Speich et al has indicated that rate of

Mn diffusion in ferrite is three orders greater than in austenite and due to this, Mn buildup forms at the grain boundary [60]. At 740°C, Mn content at the grain boundary reaches up to 3.5% weight percent (Figure 5.12). Increasing temperature to 760°C reduces the Mn concentration 2,9% and grain boundary movement towards ferrite grain becomes more distinct (Figure 5.13). Further increasing the temperature, the Mn content at the grain boundary reduces as a result of faster diffusion of Mn in ferrite and the movement of grain boundary towards ferrite become faster (Figure 5.14). In the case of low annealing temperatures, high amount of Mn build up at the grain boundaries could improve local hardenability, enabling martensite formation even at slow cooling rates.

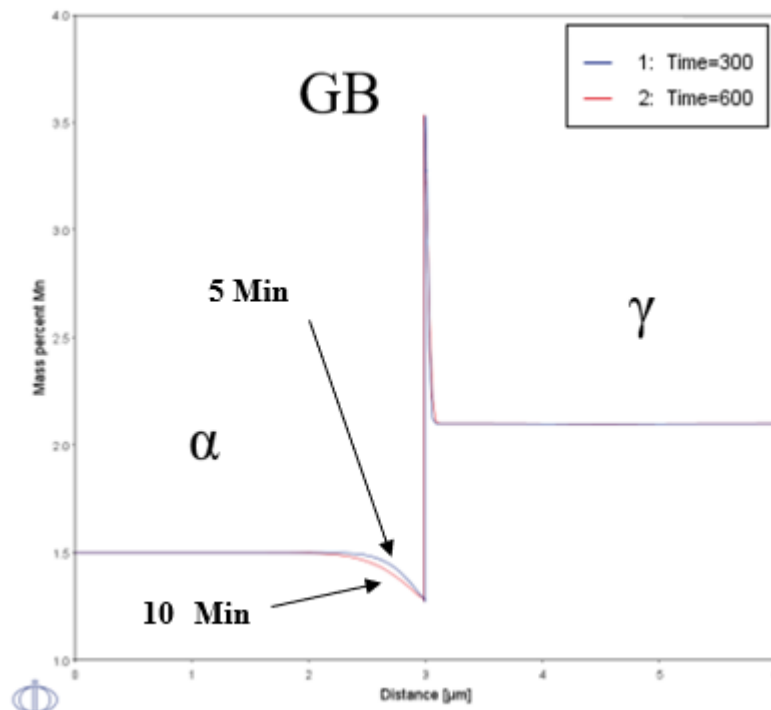


Figure 5.12. Mn partitioning during annealing at 740°C.

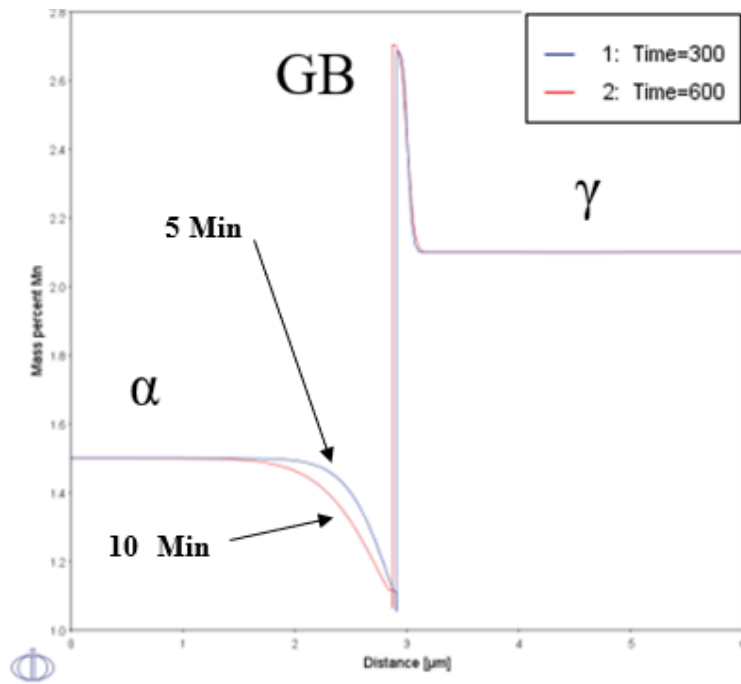


Figure 5.13. Mn partitioning during annealing at 760°C.

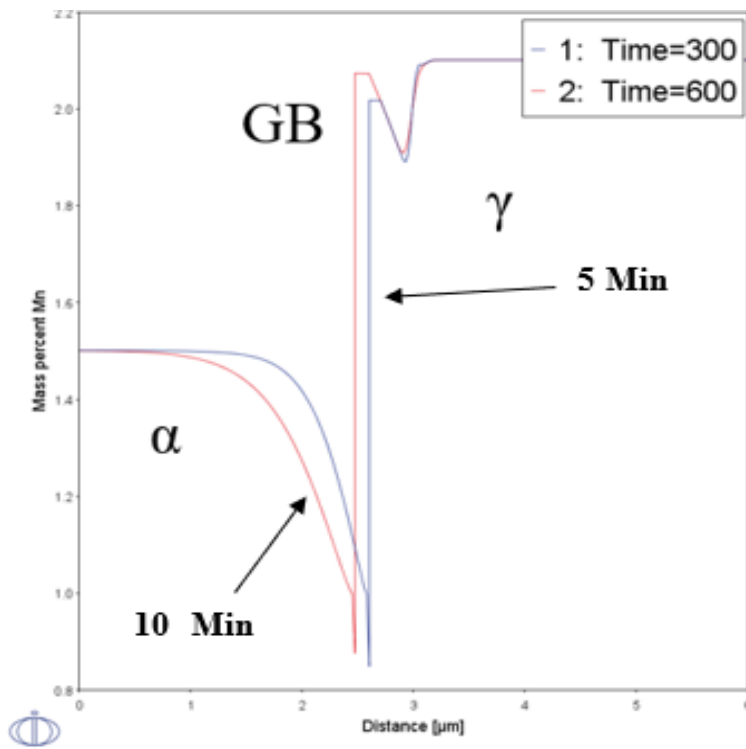


Figure 5.14. Mn partitioning during annealing at 780°C.

5.4. Comparison of Grain Sizes

The effect of heavy deformation on increasing the grain boundary area seen in Figure 5.15. As expected, heavily deformed samples have smaller grain sizes due to higher amount of energy stored and consequently higher nucleation rate. The effect of cold reduction ratio is best seen in 720°C-780°C range. At high annealing temperatures, this effect is less intense. Increasing soaking time from 5 minute to 10 minute, ferrite grain sizes of samples at high annealing temperatures are slightly reduced.

Above 730°C, reduction of ferrite grain size is seen for both 5 minute and 10 minute annealed samples. Similar results are present in the literature. In their work with 0.17C-1.15Mn-0.95Cr %80 CR steel, Mazaheri et al has reported a constant reduction in ferrite grain size for 8 minute annealing above 760°C (Figure 5.16) [75]. In a study with 0.08C-1.91Mn steel, it is established that, increasing annealing temperature from 750°C to 820°C, refinement of ferrite grains is seen [78]. The grain size refinement could be explained by the nucleation rate of austenite and ferrite grains. At higher annealing temperatures, atoms are more energetic, therefore the amount of atoms which has more energy than austenite nucleation activation energy would be higher, resulting in an increased number of grains with small grain sizes at short annealing times. Additionally, Rocha et al has reported that increasing annealing temperature reduces the energy needed for austenite nucleation, further improving nucleation kinetics, given in Figure 5.17. Combined with main nucleation sites for austenite as grain boundaries, ferrite grains will be covered with austenite at high temperatures, preventing ferrite grain growth (Figure 5.18).

With increasing annealing time from 5 minutes to 10 minutes, two mechanisms operate; slow austenite growth into ferrite due to slow diffusion speed of Mn and connection of ferrite grains. Below 740°C, where ferrite fraction is high compared to higher annealing temperatures, connection of ferrite grains is dominant, as ferrite grain size increases with time. Between 740°C and 760°C, a dominance of either mechanism

is not seen as there is no distinct pattern for ferrite grain sizes, indicating there are still uncovered ferrite/ferrite grain boundaries for merging. At 800°C however, it can be concluded that the growth of austenite into ferrite is more pronounced, causing smaller ferrite grain size.

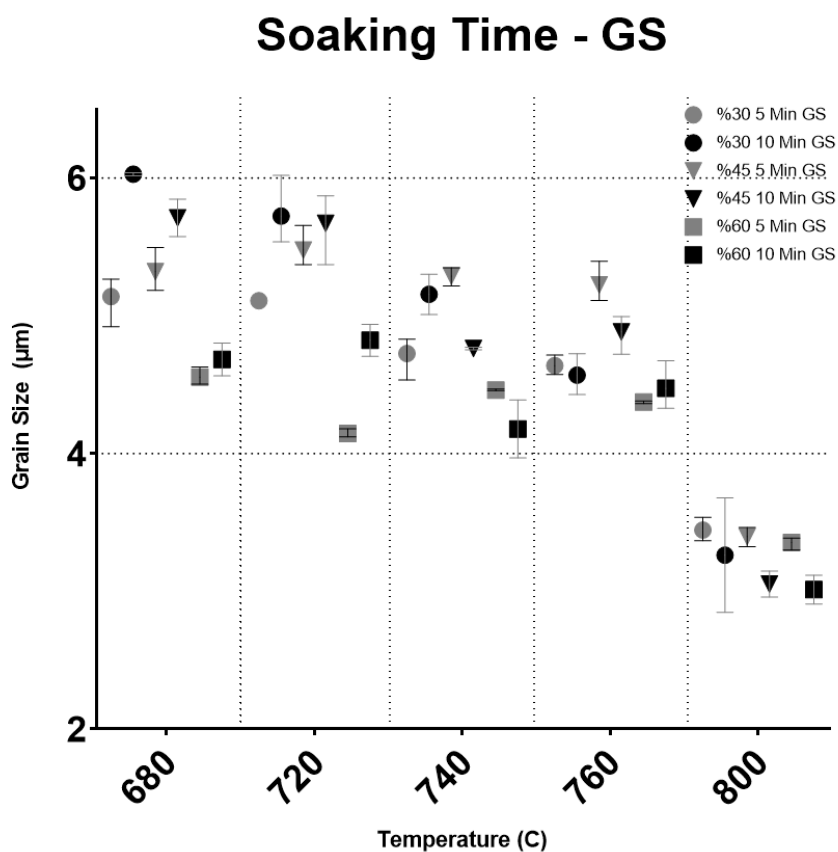


Figure 5.15. Grain sizes of annealed samples.

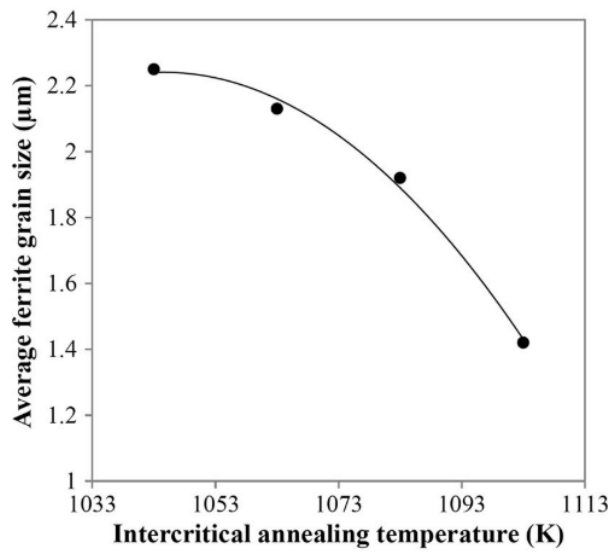


Figure 5.16. Ferrite grain size versus intercritical annealing temperature, from the study of Mazaheri et al [75].

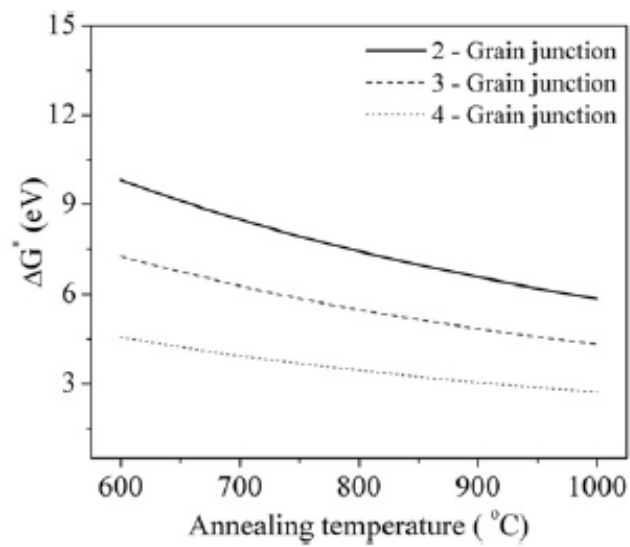


Figure 5.17. Activation energy for heterogeneous nucleation of austenite [78].

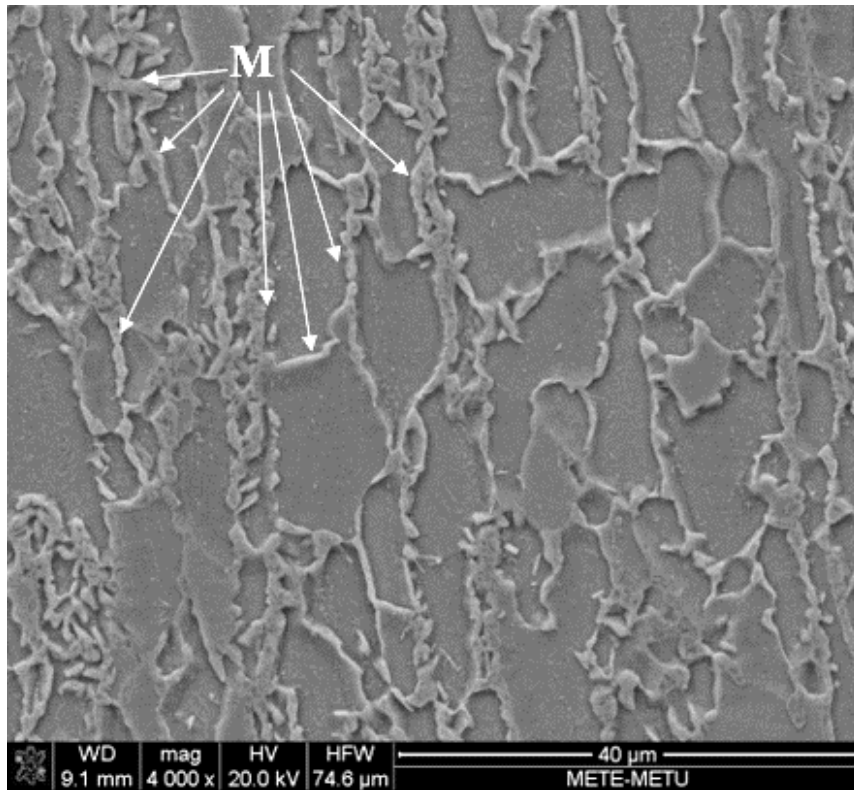


Figure 5.18. SEM image of 730-60-5. Almost all grain boundaries are covered with martensite (M).

5.5. Comparison of Ferrite Fractions

Up to 780°C, ferrite fraction of NR and 45% CR samples are similar and the highest for 5 minute samples (Figure 5.19). As discussed before, main regions for austenite nucleation are grain boundaries. As far as the 30% CR and NR samples are concerned, increase in nucleation sites for austenite as a result of cold rolling seems to have reduced the amount of ferrite.

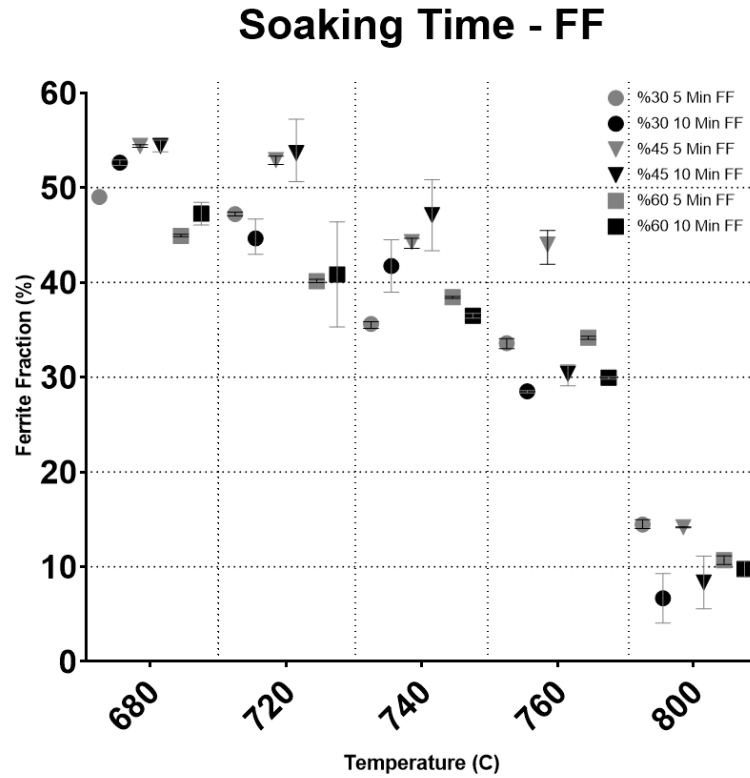


Figure 5.19. Ferrite fraction of annealed samples.

In order to maximize austenite fraction, C atoms must be able to diffuse to nearest grain boundaries and contribute to grain boundary austenite formation. Slower austenite formation due to longer path for diffusion of carbon atoms has been discussed by previous studies [49] [46]. Using conventional random walk theory, the distance for diffusion of C atoms can be calculated by:

$$l = 2 * \sqrt{D * t_{IA}} \tag{Eq.6}$$

Where l is the diffusion distance of atoms, D is the diffusion coefficient of C in austenite and t_{IA} is the intercritical annealing time. As the only variable parameter is the cold reduction ratio, at a fixed annealing time, the distance diffused by C atoms are the same for all the samples. Increasing the degree of deformation, due to

elongation and refinement of grains, diffusion of C atoms to the grain boundaries is easier.

Another effect of the degree of cold deformation is the cementite phase in pearlite. It is shown that upon excessive cold deformation, the cementite layers are fragmented to smaller particles and distribute within the matrix (Figure 5.20). As shown, higher reduction ratios causes a more homogeneous distribution of small globular cementite particles within the matrix. As reported, the equilibrium carbon solubility of ferrite surrounding a cementite with a small curvature is higher than of a high curvature, explained by Gibbs-Thomson equation [79] [80] [81]. Therefore, after extreme deformation and refinement of fragmented cementite size, carbon solubility of ferrite surrounding small cementite particles increases and causes rapid dissolution. Another work has been done by Bojian et al. They reported that, extremely small cementite particles become unstable due to very low interfacial energy to exist and dissolve in the ferritic matrix [82]. In view of these, smaller cementite particle size and shorter diffusion distance to grain boundaries, as ferrite aspect ratio of 45% CR sample is smaller, make it so that the amount of martensite inside ferrite grains in 60% CR samples lower than in 45% CR samples. When comparing 30% and 45% CR samples, due to low amount of deformation, the amount of fragmented cementite could be lower in 30% CR samples (Figure 5.20) and higher ferrite aspect ratio could reduce the time needed for C atoms to diffuse to the nearest grain boundaries, resulting in lower ferrite fraction.

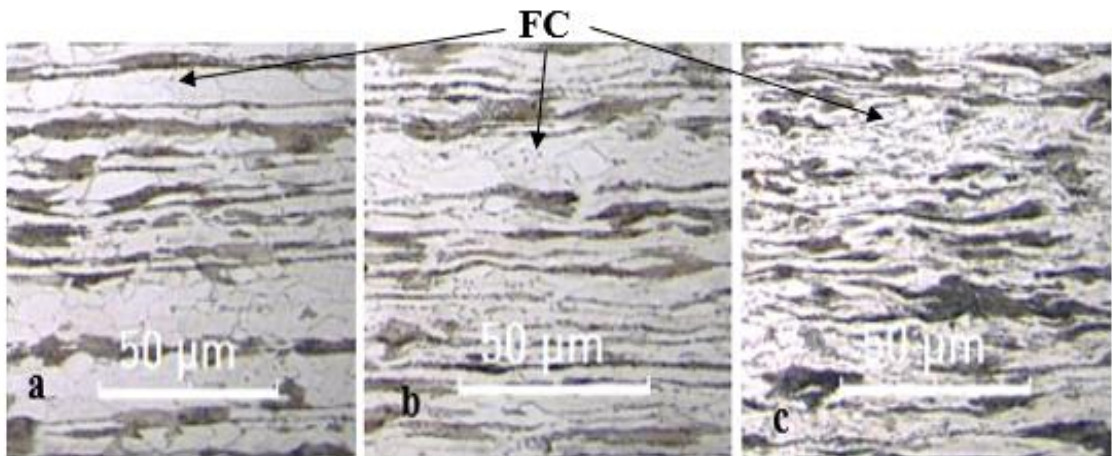


Figure 5.20. The degree of elongation of grains and cementite fragmentation in a) 30%, b) 45%, c) 60% as rolled samples. FC represents fragmented cementite.

When the above explained mechanisms are combined, the amount of martensite inside ferrite grains is higher in 45% CR sample than 30% and 60% CR samples. Another important point is that, austenite at ferrite/ferrite grain boundaries restrain the growth of ferrite grains. Therefore, grain refinement due to restrain is less effective in 45% CR sample (Figure 5.18) [83]. As martensite inside ferrite grains do not contribute to pinning of ferrite grains and require higher nucleation energy, the amount of ferrite in 45% CR samples is higher in the 730°C-780°C range (Figure 5.21, Figure 5.22, Figure 5.23). At high temperatures, differences between ferrite fraction and ferrite grain sizes are less intense, most probably due to rapid dissolution of cementite and diffusion of C [84].

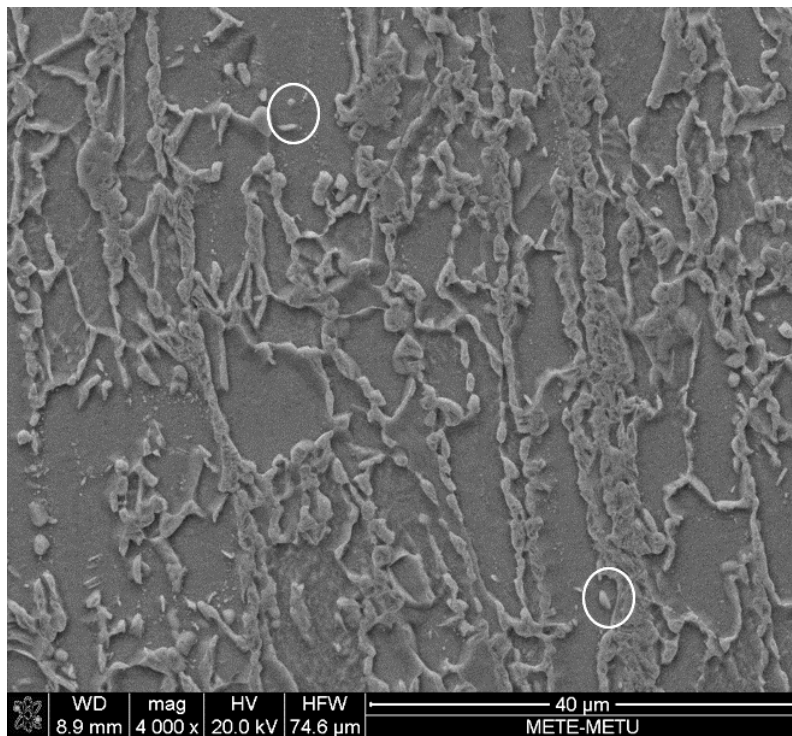


Figure 5.21. SEM image of 730-30-5. White arrows represent martensite inside the grains.

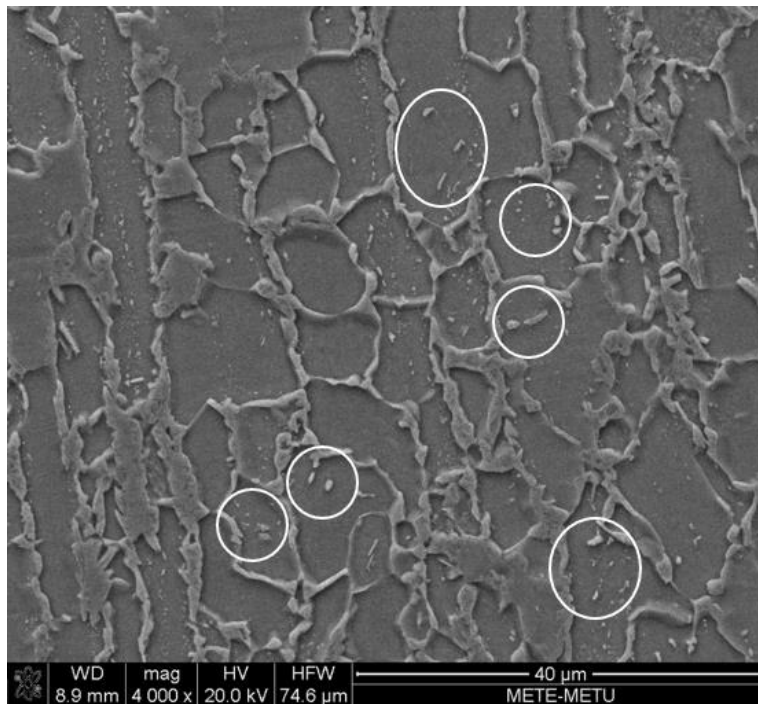


Figure 5.22. SEM image of 730-45-5. White arrows represent martensite inside the grains.

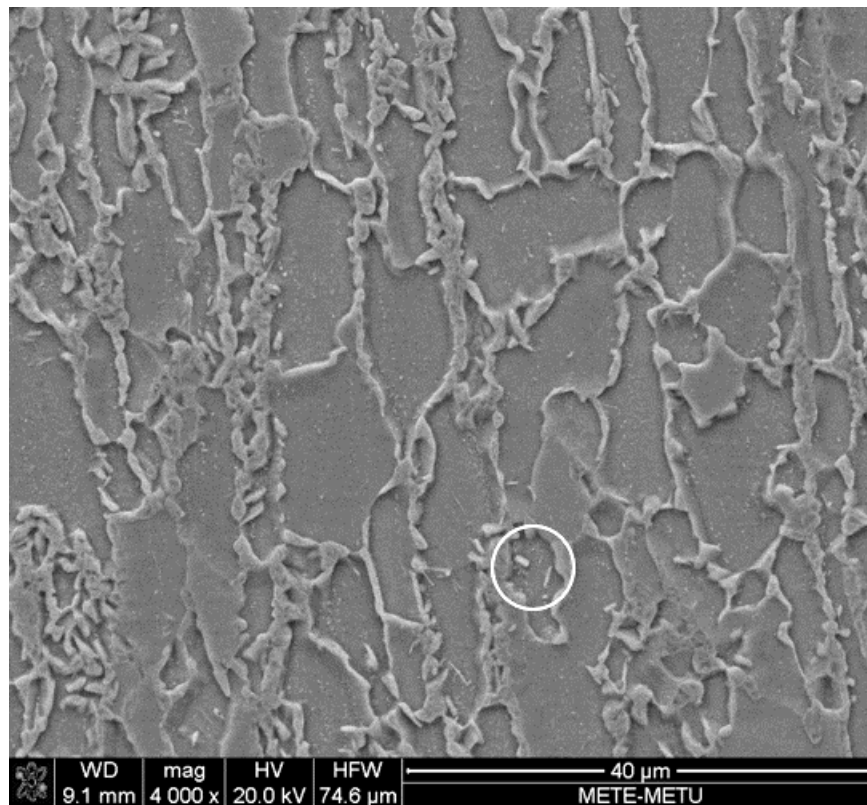


Figure 5.23. SEM image of 730-60-5. White arrows represent martensite inside the grains.

For 10 minute annealed samples, the difference between ferrite fractions between 45% CR and other samples is not as pronounced as 5 minute annealed samples, most probably due to longer time for dissolution of cementite and diffusion of C is permitted. Further reduction in ferrite fraction in 10 minute annealed samples indicate that austenite growth is not completed in 5 minutes. In Figure 5.24, volume fraction of austenite with respect to annealing time is plotted in Thermo-Calc for 0.14C-1.98Mn steel. It is seen that, rapid formation of austenite occurs under 2 minutes and consequent grain growth of austenite is very slow. Austenite growth into pearlite and cementite seems to have been completed before 5 minutes, between 5 and 10 minutes, slow growth of austenite into ferrite took place. Increase in volume fraction of austenite with increasing time has been also reported by prior studies [59] [56].

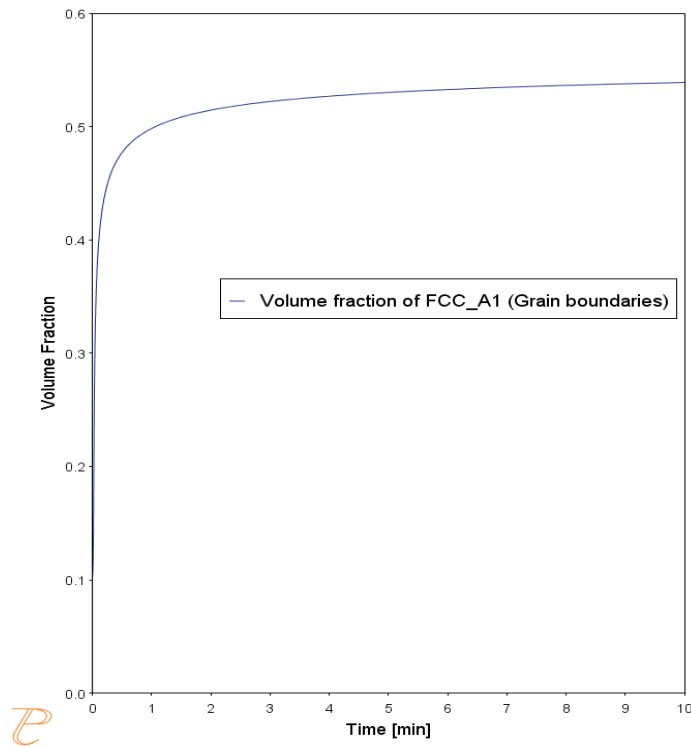


Figure 5.24. Volume fraction of austenite in 0.14C-1.98Mn steel.

5.6. Comparison of Tensile Properties

The most important effect of annealing temperature in the production of dual phase steels is the determination of amount and composition of the austenite [13]. At higher annealing temperature, dissolution kinetics of carbides is improved, resulting in a more stable austenite [85].

Below A_{e1} temperature ($711,2^{\circ}\text{C}$), both tensile and yield stresses of the samples reduce while elongation increases as a result of recrystallization and growth of ferrite grains. Above A_{e1} temperature, due to transformation of austenite to martensite upon quenching, a constant increase in tensile and yield strength can be seen (Figure 5.25). This increase could be explained by increase in volume fraction of austenite [86] [87] [88] [55].

Comparing different CR samples, below A_{e1} temperature, yield and tensile strength of 30% CR samples show highest strength levels, while 45% and 60% samples show lower strength levels. The reason is the reduction of recrystallization temperature with increasing cold deformation ratio. Higher deformation most probably causes recrystallization to start earlier, relieving internal stress and softening the material. However, increasing reduction ratio from 45% to 60% did not seem to affect mechanical properties very much. This could be explained by the fact that, 60% CR samples still having elongated and non-equiaxed grains could have led to poor mechanical properties (Figure 5.1, Figure 5.2, Figure 5.4).

Above 730°C, 30% and 60% CR mechanical properties are very similar, while 45% CR show lower yield and tensile strength. In their study, Pan et al has mentioned that, low density precipitations inside ferrite grains are less effective in increasing tensile strength than grain refinement by dissolution and diffusion of precipitations to grain boundaries and contribution to grain boundary austenite formation [83]. Also, as lesser austenite is present at the grain boundaries, the connected-network structure of the austenite is less intense in 45% CR samples. Terada et al has reported that, with the same amount of martensite fraction, fully connected-network structure has a better strength-ductility balance than a structure with isolate martensite islands and the reason is explained as more uniform distribution of stress between ferrite and martensite phases, given in Figure 5.26 [89]. Therefore, low yield and tensile strength of 45% CR steel can be explained by higher ferrite fraction, second-order contribution of cementite particles inside ferrite grains to tensile strength and lesser intensity of networked martensite structure.

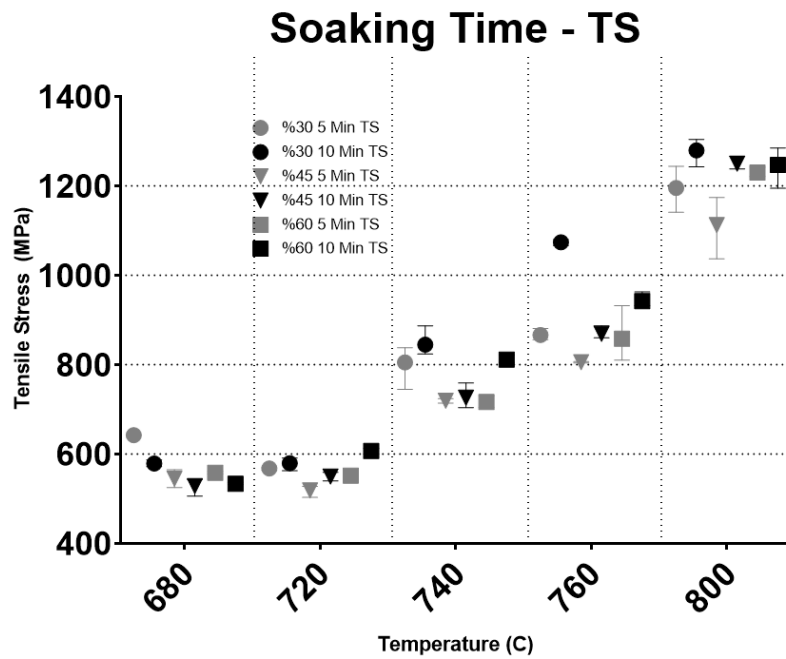


Figure 5.25. Tensile strengths of 5 minute and 10 minute annealed samples .

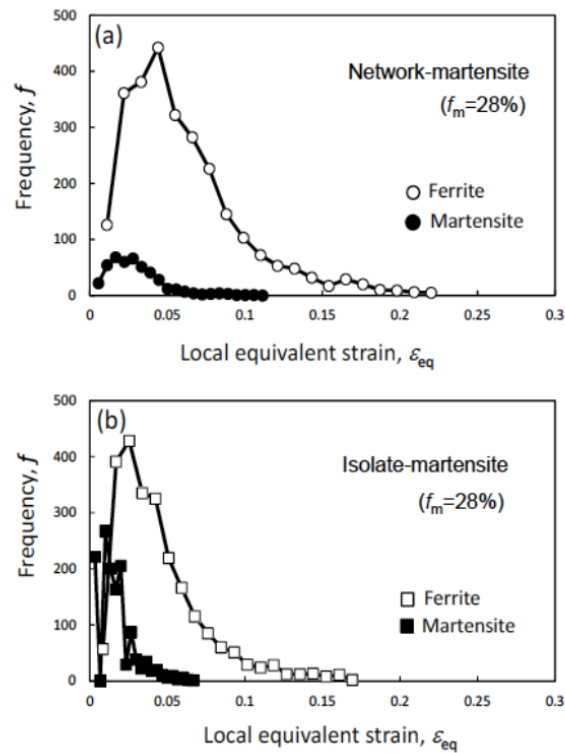


Figure 5.26. Strain distribution between ferrite and martensite in networked and isolated martensite structures [89].

CHAPTER 6

CONCLUSIONS

In order to see the effect of cold rolling ratio and annealing parameters during production of dual phase steels, same material with different reduction ratios and annealing parameters have been studied. Analyzing the results, following conclusions are obtained:

1. Even though recrystallization temperature is decreased with an increase in degree of cold working, highly deformed samples need longer recrystallization time in order to fully restore mechanical properties and have equiaxed grains. For this study, a 10 minute soaking time is found enough for stabilizing microstructure in terms of phase transformations.
2. The amount of martensite phase formed highly depends on the intercritical annealing temperature and time. Increasing the temperature, the amount of martensite increases in correlation with the lever rule.
3. At high intercritical annealing temperatures, ferrite grain sizes become smaller as a result of restrained grain growth of ferrite by austenite. This effect is not pronounced at lower temperatures, due to the fact that the nucleating austenite at the ferrite grain boundaries do not form a continuous network.
4. Main nucleation sites for austenite are the carbon rich grain boundaries. These boundaries are basically ferrite/cementite, ferrite/pearlite and ferrite/ferrite boundaries. There is almost none or very limited austenite formation within a pearlite grain.
5. There exists a critical cold rolling ratio range during production of dual phase steels from a pearlite-ferrite starting microstructure. Faster overall equiaxed grain formation during heating causes ferrite aspect ratios of 45% CR samples

to be lowest, therefore leaving lesser grain boundary area for nucleation of austenite.

REFERENCES

- [1] "Review of EuroCarBody," Bad Neuheim, 2011.
- [2] "Dual Phase and Cold Pressing Vanadium Steels in the Automobile Industry: Proceedings of Seminar," Berlin, 1978.
- [3] R. A. Kot and J. W. Morris, "Structure and Properties of Dual-Phase Steels," in *AIME*, New York, 1981.
- [4] J. F. B. Pereira, *Metall. Mater. ABM* 59, pp. 149-52, 2002.
- [5] S. Estay, L. Chengji and G. Purdy, "CARBIDE DISSOLUTION AND AUSTENITE GROWTH IN THE INTERCRITICAL ANNEALING OF Fe-C-Mn DUAL PHASE STEELS," in *Canadian Metallurgical Quarterly*, 1984.
- [6] F. S. Barrado, T. M. F. Melo, L. C. Candido and L. B. Godefroid, "Rolling and Laminated Products," *Processes and Products Seminar*, pp. 536-44, 2003.
- [7] S. Nikkhah, H. Mirzadeh and M. Zamani, "Fine tuning the mechanical properties of dual phase steel via thermomechanical processing of cold rolling and intercritical annealing," *Materials Chemistry and Physics*, 2019.
- [8] Y. Zhang, Q. Yuan, J. Ye, X. Weng and Z. Wang, "Effect of cold rolling reduction on microstructure, mechanical properties, and texture of deep drawing dual-phase (DP) steel," *Mater. Res. Express*, 2019.
- [9] I. Gupta and P. H. Chang, "Effect of Compositional and Processing Parameters on the Steels," in *Technology of Continuously Annealed Cold-Rolled Sheet Steels*, Detroit.

- [10] S. Hayami and T. Furukawa, "A Family of High-Strength Cold-Rolled Steels," *Microalloying*, pp. 311-321, 1975.
- [11] R. G. Davies, "The Deformation Behavior of a Vanadium-Strengthened Dual Phase Steel," *Metallurgical Transactions*, vol. 9, no. 1, pp. 41-52, 1978.
- [12] R. G. Davies and C. L. Magee, "Physical Metallurgy of Automotive High Strength Steels," in *Conference of Structure and Properties of Dual-Phase Steels.*, New Orleans, 1981.
- [13] N. Fonstein, *Advanced High Strength Sheet Steels*, Springer, 2015, pp. 2-3.
- [14] L. Samek and Krizan, *Steel-Material of Choice for Automotive Lightweight Applications*, 2012.
- [15] I. Berger, M. Lesemann and C. Sahr, *Superlight-CAR - the Multi-Materials Car Body*, 2009.
- [16] "EN 10338:2015 E," EUROPEAN COMMITTEE FOR STANDARDIZATION, 2015.
- [17] W. D. Callister and D. G. Rethwisch, *Materials Science and Engineering*, Elsevier, 2006.
- [18] "Advanced Vehicle Concepts Technical Transfer Dispatch," in *Ulsab-Avc Concertium*, 2001.
- [19] M. Sarwar and R. Priestner, "Influence of Ferrite-Martensite Microstructural Morphology on Tensile Properties of Dual Phase Steels," *Journal of Materials Science*, pp. 2091-95, 1996.

- [20] A. P. Coldren, G. Tither, A. Cornford and J. R. Hiam, "Development and Mill Trial of As-Rolled Dual-Phase Steels," *Formable HSLA and Dual-Phase Steels*, pp. 205-27, 1977.
- [21] T. Greday, H. Mathy and P. Messien, "About Different Ways to Obtain Multiphase Steels," *Structure and Property of Dual-Phase Steels*, pp. 260-80, 1979.
- [22] T. Kato, K. Hashiguchi, I. Takahashi, T. Irie and N. Ohashi, "Development of As-Hot-Rolled Dual Phase Steel Sheet," *Fundamentals of Dual-Phase Steels*, pp. 199-220, 1981.
- [23] A. F. Crawley, M. T. Shehata, N. Pussegota, C. M. Mitchell and W. R. Tyson, "Processing, Properties and Modelling of Experimental Batch-Annealed Dual-Phase Steels," *Fundamentals of Dual-Phase Steels*, pp. 181-97, 1981.
- [24] A. Okamoto and M. Takahashi, "Control of Strength and r-Value in Box-Annealed Dual Phase Steel Sheet," *Fundamentals of Dual-Phase Steels*, pp. 427-45, 1981.
- [25] H. Hsun, "Effect of silicon on annealing texture, plastic anisotropy, and mechanical prop-," *Formable HSLA and Dual-Phase Steels*, pp. 109-25, 1977.
- [26] J. Pittner, "A New Strategy for Optimal Control of Continuous Tandem Cold Metal Rolling," *IEEE TRANSACTIONS ON INDUSTRY APPLICATIONS*, p. 703, 2010.
- [27] A. Belotserkovets, R. Deltombe, M. Dubar, L. Dubar, A. Dubois, H. Vandekinderen and J. Damasse, "ROUGHNESS PREDICTION DURING COLD ROLLING OF STAINLESS STEEL STRIP: FLUID STRUCTURE APPROACH," *Int J Mater Form*, p. 22, 2009.

- [28] F. J. Humphreys and M. Hatherly, *Recrystallization and Related Annealing Phenomena*, Elsevier, 2004.
- [29] W. C. Leslie and E. Hornbogen, "Physical metallurgy of steels," in *Physical Metallurgy Vol2*, ELSEVIER SCIENCE, 1996, p. 1590.
- [30] "Grain Structure," 2017. [Online]. Available: <https://www.the-warren.org/ALevelRevision/engineering/grainstructure.htm>.
- [31] Y. Granbom, "Structure and mechanical properties of dual phase steels – An experimental and theoretical analysis," *La Revue de Métallurgie-CIT*, 2010.
- [32] I. Schindler, M. Janošec, E. Mistecký, M. Růžička and L. A. Dobrzański, *Archives Mat. Sci. Eng.*, 2009.
- [33] Y. D. Huang, W. Y. Yang and Z. Q. Sun, *J. Mat. Proc. Tech.*, 2003.
- [34] P. B. Prangnell, J. R. Bowen and P. J. Apps, *Mat. Sci. Eng. A*, 2004.
- [35] P. D. Hodgson, M. R. Hickson and R. K. Gibbs, *Mater. Sci. Forum*, pp. 284-86, 1988.
- [36] M. R. Hickson, P. J. Hurley, G. L. Kelly, P. D. Hodgson and M. R. Barnett, in *2nd Symposium on Supermetals*, Tokyo, 1999.
- [37] H. Hu, "Trans.," *AIME*, p. 224, 1962.
- [38] G. N. Haidemenopoulos, *Physical metallurgy: Principles and design*, 2018.
- [39] G. C. Venturello, C. Antonione and C. Bonaccorso, "Trans.," *AIME*, p. 227, 1963.
- [40] R. W. Cahn and P. Haasen, *Physical Metallurgy Vol2*, Amsterdam: ELSEVIER SCIENCE, 1996.

- [41] W. C. Leslie, J. T. Michalak and F. W. Aul, "Iron and its Dilute Solid Solutions," *Interscience*, 1963.
- [42] M. S. Rashid, "Ann. Rev. Mater. Sci.," *Dual Phase Steels*, pp. 245-66, 1981.
- [43] P. Wycliffe, G. R. Purdy and J. D. Embury, "Austenite Growth in the Intercritical Annealing of Ternary and Quaternary Dual-Phase Steels," in *Conference of Fundamentals of Dual-Phase Steels, Symposium at the 110th AIME Annual Meeting*, Warrendale, 1981.
- [44] R. R. Judd and H. W. Paxton, "Trans. TMS-AIME," p. 206, 1968.
- [45] J. Newkirk, "Lectures on Precipitation from Solid Solution," in *ASM*, Ohio, 1957, p. 15.
- [46] C. I. Garcia and A. J. Deardo, "METALLURGICAL TRANSACTIONS A," *Formation of Austenite in 1.5 Pct Mn Steels*, 1981.
- [47] H. Azizi-Alizamini, M. Militzer and W. Poole, "ISIJ Int.," pp. 958-64, 2011.
- [48] M. Calcagnotto, D. Ponge and D. Raabe, "ISIJ Int.," pp. 874-83, 2012.
- [49] Y. Granboom, "Effects of Process Parameters prior to Annealing on the Formability of Two Cold Rolled Dual Phase Steels," *Steel Research International*, pp. 297-305, 2008.
- [50] Wever, *Archiv für Eisenhüttenwesen* 2, p. 193, 1928.
- [51] H. K. D. H. Bhadeshia and R. W. K. Honeycombe, *Steels, Microstructure and Properties*, Elsevier, 2006.
- [52] K. W. Andrews, "Empirical Formulae for Calculation of Some Transformation Temperatures," *Iron and Steel Institute Journal*, pp. 721-27, 1965.

- [53] G. R. Speich, "Physical Metalurgy of Dual Phase Steels," in *Fundamentals of Dual Phase Steels*, 1981.
- [54] J. M. Rigsbee and P. J. Vanderarend, "Laboratory studies of Microstructures and Structure Property Relationships in Dual Phase Steels," in *Formable HSLA and Dual Phase Steels*, 1977.
- [55] V. Concepción, H. N. Lorusa and H. G. Svoboda, "International Congress of Science and Technology of Metallurgy and Materials," *Effect of carbon content on microstructure and mechanical*, pp. 1047-56, 2015.
- [56] M. Calcagnotto, D. Ponge and D. Raabe, "On the Effect of Manganese on Grain Size Stability and Hardenability in Ultrafine-Grained Ferrite/Martensite Dual-Phase Steels," *METALLURGICAL AND MATERIALS TRANSACTIONS A*, 2011.
- [57] E. K. S. Moor, J. G. Speer and D. K. Matlock, "Manganese Diffusion in Third Generation Advanced High," *Proceedings of the International Conference on Mining, Material and Metallurgical Engineering*, 2014.
- [58] S. Shoujin and M. Pugh, "Manganese partitioning in dual-phase steel during annealing," *Materials Science and Engineering*, pp. 164-74, 2000.
- [59] J. Huang, W. J. Poole and M. Militzer, "Austenite Formation during Intercritical Annealing," *METALLURGICAL AND MATERIALS TRANSACTIONS A*, 2004.
- [60] G. R. Speich, V. A. Demarest and R. L. Miller, "Formation of Austenite During Intercritical Annealing of Dual-Phase Steels," *METALLURGICAL TRANSACTIONS A*, 1981.

- [61] A. Nouri, H. Saghafian and S. Kheirandish, "Effects of Silicon Content and Intercritical Annealing on Manganese Partitioning in Dual Phase Steels," *Journal of Iron and Steel Research International*, pp. 44-50, 2010.
- [62] P. Abramowitz and R. A. Moll, "Metall. Trans. 1," pp. 1773-75, 1970.
- [63] J. Y. Koo and G. Thomas, "Design of Duplex Fe/X/0.1C Steels for Improved Mechanical," *Metallurgical Transactions A*, pp. 525-28, 1977.
- [64] N. Fonstein, H. Jun, O. Yakubovsky, R. Song and N. Pottore, "Evolution of Advanced," 2013.
- [65] A. Mein, G. Fournalis, D. Growther and P. Evans, "Material Science and Technology," *Influence of Aluminium Additions upon*, pp. 627-33, 2012.
- [66] O. Girina and N. Fonstein, "Influence of Al additions on Austenite Decomposition in a Continuously Annealed Dual Phase Steels," in *MS&T*, 2005.
- [67] T. Irie, S. Satoh, K. Hashiguchi, I. Takahashi and O. Hashimoto, "Characteristics of Formable Cold Rolled High Strength Steel Sheets for Automotive Use," *Kawasaki Steel Technical Report*, pp. 14-22, 1981.
- [68] T. Hara, H. Asahi, R. Uemori and H. Tamehiro, "Role of Combined Addition of Niobium and Boron and of Molybdenum and Boron on Hardenability in Low Carbon Steels," *ISIJ International*, p. 1431, 2004.
- [69] A. P. Coldren and G. Eldis, "Using CCT Diagrams to Optimize the Composition of an as Rolled Dual Phase Steel," *Journal of Metals*, pp. 41-48, 1980.

- [70] L. M. Kaputkina, A. V. Marmulev, G. Herman and E. I. Poliak, "Microstructure Heredity and Non Uniformity of Mechanical Properties During Hot Rolling," in *Machines, Technologies, Materials*, 2013.
- [71] E. Emadoddin, "Effect of cold rolling on annealing behavior and retained austenite characteristics of multiphase CMnSi steel," *ISIJ International*, pp. 330-36, 2013.
- [72] V. I. Savran, Y. V. Leeuwen, D. N. Hanlon, C. Kwakernaak, W. G. Sloof and J. Sietsma, "Microstructural Features of Austenite Formation in C35 and C45 alloys," *The Minerals, Metals & Materials Society and ASM International*, pp. 946-55, 2007.
- [73] F. Qian and W. M. Rainforth, "The formation mechanism of reverted austenite in Mn-based maraging steels," *Journal of Material Science*, 2019.
- [74] X. Luo, L. Han and J. Gu, "Study on Austenitization Kinetics of SA508 Gr.3 Steel," *Metals*, 2016.
- [75] Y. Mazaheri, A. Kermanpur and A. Najafizadeh, "Kinetics of Ferrite Recrystallization and Austenite Formation During Intercritical Annealing of the Cold-Rolled Ferrite/Martensite Duplex Structures," *Metallurgical and Materials Transactions A: Physical Metallurgy and Materials Science*, pp. 1040-51, 2016.
- [76] K. Mukunthan and E. B. Hawbolt, "Modeling recovery and recrystallization kinetics in cold-rolled Ti-Nb stabilized interstitial-free steel," *Metallurgical and Materials Transactions A: Physical Metallurgy and Materials Science*, pp. 3410-23, 1996.
- [77] J. S. Kirkaldy and D. Venugopalan, "Phase Transformations in Ferrous Alloys," *TMS-AIME*, pp. 125-48, 1984.

- [78] R. Rocha, T. Melo, E. Pereloma and D. B. Santos, "Microstructural evolution at the initial stages of continuous annealing of cold rolled dual-phase steel," *Materials Science and Engineering A*, pp. 296-304, 2005.
- [79] B. Chalmers, *Physical Metallurgy*, New York: Wiley, 1959.
- [80] I. Novikov, "Theory of heat treatment of metals," *Metallurgia*, p. 479, 1986.
- [81] M. Perez, "Gibbs–Thomson effects in phase transformations," *Scripta Materialia*, pp. 709-12, 2005.
- [82] W. Bojian, G. Xiaochen, X. Qiang and L. Shifeng, "Evolution of Cementite in Hypoeutectoid Steel Wire during Cold Work Hardening in Rolling Process," *International Journal of Mineral Processing and Extractive Metallurgy*, pp. 60-64, 2018.
- [83] Z. Pan, B. Gao, Q. Lai, X. Chen, Y. Cao, M. Liu and H. Zhou, "Microstructure and mechanical properties of a cold-rolled ultrafine-grained dual-phase steel," *Materials*, pp. 1-11, 2018.
- [84] L. Hui, H. Zhang, L. Zheng-feng and Z. Zheng-feng, "Cementite Dissolution Kinetics of High Carbon Chromium Steel During Intercritical Austenitization," *J. Phase Equilib. Diffus.*, 2017.
- [85] C. Garcia, K. Cho, K. Redkin, A. Deardo, S. Tan, M. Somani and L. Karjalainen, "Influence of Critical Carbide Dissolution Temperature during Intercritical Annealing on Hardenability of Austenite and Mechanical Properties of DP980 Steels," *ISIJ International*, pp. 969-74, 2011.
- [86] N. Matsumara and M. Tokizane, "Microstructure and the Mechanical Properties of Dual-Phase Steel Produced By Intercritical Annealing of Lath Martensite," *ISIJ*, 1984.

- [87] J. Lis, A. Lis and C. Kolan, "Processing and properties of C-Mn steel with dual-phase microstructure," *Journal of Materials Processing Technology*, pp. 350-54, 2005.
- [88] G. Rosenberg, I. Sinaiova and P. Hvizdos, "Development of Cold-Rolled Dual-Phase Steels with Tensile Strength Above 1000 MPa and Good Bendability," *Metallurgical and Materials Transactions A: Physical Metallurgy and Materials Science*, pp. 4755-71, 2015.
- [89] D. Terada, G. Ikeda, M. H. Park, A. Shibata and N. Tsuji, "Reason for high strength and good ductility in dual phase steels composed of soft ferrite and hard martensite," in *IOP Conference Series: Materials Science and Engineering*, 2017.
- [90] D. C. Smith, *Palestine and the Arab–Israeli Conflict*, New York: Bedford, 2006, p. 329.
- [91] L. Meyer, F. Heisterkamp and W. Mueschenborn, "Columbium, Titanium and Vanadium in Normalized, Thermo-mechanically Treated and Cold-Rolled Steels," in *International Symposium on High Strength Low-Alloy Steels*, Pittsburgh, 1975.
- [92] M. Aydın, *Steel Materials*, vol. 2, İstanbul: Aybitak, 2017, pp. 552-590.
- [93] "Metallography, Structures, and Phase Diagrams," in *Metals Handbook, 8th ed.*, 1973, American Society for Metals, 1973.
- [94] Thelning, "Steel and its Heat Treatment," *Bofors Handbook*, 1975.
- [95] "Properties and Selection of Metals," in *Metals Handbook 8th ed.*, American Society for Metals, 1961, p. 13.
- [96] H. K. D. H. Bhadeshia, *Bainite in Steels*, Leeds: Maney Publishing, 2015.

- [97] A. Y. Bratashevskii and A. I. Khristoforov, "Position of the Intercritical Point Ac1 After Cold Rolling of Steel 25," *Metallovedenie i Termicheskaya Obrabotka Metallov*, pp. 417-18, 1984.
- [98] A. E. Conford, J. R. Hiam and R. Hobbs, *SAE Tech Paper Series 79007*, 1979.
- [99] J. Gilmour, G. R. Purdy and J. S. Kirkaldy, "Met. Trans A," p. 3213, 1972.
- [100] E. R. Petty, *Martensite: Fundamentals and Technology*, London: Longmans, 1970.
- [101] M. S. Rashid, "SAE Trans.," pp. 935-46, 1977.
- [102] O. A. Girina, N. M. Fonstein and D. Bhattacharya, "Effect of Nb on the Phase Transformation and Mechanical Properties of Advanced High Strength Dual-Phase Steels," in *International Conference of New Developments on Metallurgy and Applications of High Strength Steels*, Buenos Aires, 2008.
- [103] W. F. Hosford, *Physical Metallurgy*, New York: CRC Press, 2010.
- [104] C. M. Wayman and H. K. D. H. Bhadeshia, "PHASE TRANSFORMATIONS, NONDIFFUSIVE," in *Physical Metallurgy Vol2*, Amsterdam, ELSEVIER SCIENCE, 1996, p. 1511.
- [105] M. Goune, P. Maugis and J. Drillet, "A Criterion for the Change from Fast to Slow Regime of Cementite Dissolution in Fe-C-Mn Steels," *Mater. Sci. Technol.*, pp. 728-36, 2012.